Title
Operational Control and Survivability Enhancement of Asymmetric Wave-Energy Converters

Author
Madhi, Farshad

Publication Date
2016

Peer reviewed|Thesis/dissertation

Operational Control and Survivability Enhancement of Asymmetric Wave-Energy Converters

by

Farshad Madhi

A dissertation submitted in partial satisfaction of the

requirements for the degree of

Doctor of Philosophy

in

Engineering - Mechanical Engineering

in the

Graduate Division

of the

University of California, Berkeley

Committee in charge:

Professor Ronald W. Yeung, Chair
Professor Stephen Morris
Professor Jon Wilkening

Fall 2016

Abstract

Operational Control and Survivability Enhancement of Asymmetric Wave-Energy Converters

by

Farshad Madhi

Doctor of Philosophy in Engineering - Mechanical Engineering

University of California, Berkeley

Professor Ronald W. Yeung, Chair

The aim of this research is to study the operational and survivability modes of asymmetric wave-energy converters (AWEC). "The Berkeley Wedge" (TBW), a one-degree-of-freedom, asymmetrical, energy-capturing, floating breakwater, which is relatively free from viscosity effects, is used as a canonical problem of study.

For the operational mode, the focus of the analysis is to optimize the power-to-load ratio of TBW. Linear hydrodynamic theory was used to calculate bounds on the expected time-averaged power (TAP), the corresponding surge restraining force, pitch restraining torque, and power take-off (PTO) control force. This thesis formulates the optimal control problem to incorporate metrics that provide a measure of the surge restraining force, pitch restraining torque, and PTO control force. The controller handles an objective function with competing terms, so as to maximize power capture while minimizing structural and actuator loads. In achieving these goals, a per-unit gain in TAP would not lead to a greater per-unit demand in structural strength, hence yielding a favorable benefit-to-cost ratio. Demonstrative results in the form of TAP, reactive TAP, and the amplitudes of the surge restraining force, pitch restraining torque, and PTO control force are shown for TBW example.

To provide guidance for improving the survivability of the AWECs, analysis of the extreme forces they experience in deep-water breaking waves was conducted. The forces were obtained by computation using the Weakly Compressible Smoothed Particle Hydrodynamics (WCSPH) method and also by model-scaled experiments (conducted at the RFS Model Testing Facility of the University of California at Berkeley). Breaking waves were first generated for both physical and computational modeling by developing appropriate time histories of the wavemaker, using potential-flow theory. Plunging breakers and wave forces at two target locations by computations were verified by experiments. The effects of different drafts of TBW on the force reduction were studied. To increase the survivability while maintaining the operational draft of the TBW, pressure-relief channel (PRC), a new scheme that allows water to flow through TBW was implemented. The PRC effectiveness in reducing the extreme wave forces was demonstrated computationally. With guidance from these computations, a design is proposed to illustrate an effective way to install and operate the PRCs so as to increase the survivability of TBW and similar devices in extreme sea states.

Dedication

To my wife Sahba and my parents Rouhollah & Farangis for all of their love, kindnesses, and encouragements

Know that the reality of man embraces the realities of things, and discovers the verities, properties and secrets of things. So all these arts, wonders, sciences and knowledge have been discovered by the human reality. At one time these sciences, knowledge, wonders and arts were hidden and concealed secrets; then gradually the human reality discovered them and brought them from the realm of the invisible to the plane of the visible.

'Abdu'l-Bahá
Some Answered Questions

Acknowledgments

I would like to express my sincere gratitude to my advisor Prof. Ronald W. Yeung. His insights and broad expertise in Marine Mechanics are salutary. His initial work and original idea of TBW are the cornerstones of this thesis. I am very much grateful for his constant support during my academic career at UC Berkeley. He is a great mentor, teacher, and role model. His commitment to excellence, care for students, classroom teachings, and his pioneering works are inspirations to me.

I am thankful to Professors Stephen Morris and Jon Wilkening for their guidance, encouragements, and excellent classroom teachings. Also, I would like to thank them for serving on this Ph.D. thesis committee and their review of this thesis.

Many thanks go to my friend and laboratory colleague Dr. Nathan Tom. He has been a sincere friend and mentor since the beginning of my graduate studies. His invaluable assistance and collaborations in the theoretical part of this thesis has been crucial.

I would like to thank Faraz Tavakoli and Pouria Talebifard for their advice in the computational part of this thesis. Also would like to thank Yun Linn, Ryan Sanders, and John Reilly Marin for their help in the design process.

I am grateful to Daewoong Son for his assistance in the experimental setup and during the experiments. I would like to thank Lu Wang and Mohamed Hariri for many constructive discussions.

My utmost gratitude goes to my wife Sahba and my parents Rouhollah & Farangis. Their constant love and support assisted me beyond measure.

Contents

List of Figures

List of Tables

List of Abbreviations

AF	Asymmetric Floater
AWEC	Asymmetric Wave Energy Converter
BEM	Boundary Element Method
BMML	The Berkeley Marine Mechanics Laboratory
CWT	Computational Wave Tank
LPMG	Linear Permanent Magnet Generator
PRC	Pressure-Relief Channel
PTO	Power-Take-Off
PWT	Physical Wave Tank
RFS	Richmond Field Station
SPH	Smoothed Particle Hydrodynamics
TAP	Time-Averaged Power
TBW	The Berkeley Wedge
WEC	Wave Energy Converter
WCSPH	Weakly Compressible Smoothed Particle Hydrodynamics

Chapter 1

Introduction

The negative effects of fossil fuel consumptions on the environment and our daily lives are becoming more and more apparent. Parallel to this, many movements and research projects have been initiated to increase the efficiency and reliability of the means of harnessing renewable energy resources [1]. Renewable energy resources, such as solar, wind, geothermal, ocean waves, etc., are abundant and can be used in combinations to overcome the energy crisis [2] and to reduce fossil fuel consumption. One of the resources with high potential, availability, and predictability is ocean waves [3, 4]. Many devices are proposed or implemented for harvesting wave energy [5, 6]. The ocean is an unforgiving environment and wave energy converters (WEC) face multiple destructive forces such as corrosion, fatigue, large forces by extreme waves, etc. Even after the proof of concept and laboratory testing of WECs, many challenges remain in terms of installation cost, maintenance, and survivability of the devices. Most of the proposed WEC designs are highly complicated and consist of many parts. Thus, many of the WECs eventually fail under fatigue stress even before encountering severe weather.

The performance conditions of WECs can be categorized into operational and survival modes [7]. In the design process of WECs, it is also crucial to obtain a clear understanding of the range of peak periods and wave heights that lead to the best energy absorption to load ratios. In the operational mode, it is required to develop control strategies that can adapt device performance to maximize energy generation while mitigating hydrodynamic loads so as to reduce the structural mass and overall cost [8]. Balancing these objectives offers an interesting design and control challenge. For example, they are in contrast to previous works that solved the optimal control problem with the sole focus on maximizing the time-averaged power (TAP). The application of state-constrained optimization [9–11] to WEC control has gained significant traction recently as it provides the ability to include linear and nonlinear constraints. This optimization has been pursued using calculus of variations [9], model predictive control [12–14], and pseudo-spectral methods [15–17]. If the PTO and structural loads are not considered, the optimum WEC trajectory follows that of complex conjugate control [18], which is known to require a substantial amount of reactive power when moving away from the resonance frequency. Suboptimal strategies that eliminate reactive power, notably latching [19] and declutching [20], have been proposed, yet still do not include a load metric in the optimization. It can be expected that as the controller works to maximize the absorbed mechanical energy, the growth rate in structural loads may exceed the growth in TAP. To address this concern, this work incorporates the restraining loads in the objective function of the optimization routine. As a result, the optimizer must now balance the opposing contributions in an attempt to obtain the largest

power-to-load ratio.

One of the biggest challenges facing the wave energy technology is to increase the survivability of WECs in extreme waves. Until recently, the main focus of the design of WECs was to increase their efficiency. However, it is evident that the survivability of the WECs is as important, if not more so, as their efficiency. The importance of including extreme wave load measurements in the design process of WECs is emphasized in recent studies [21]. One of the solutions proposed to decrease extreme forces on the floating objects is to fully submerge them [22]. With this approach the slamming forces on the bodies decrease. For the surface-piercing floaters, such as Salter's duck (an asymmetric WEC, AWEC), a study [23] suggests maintaining undamped motion of the floater when it encounters breaking waves. In this scenario, such devices capsize but the total forces they experience are reduced [24]. Another study suggests that adding a power-take-off system (PTO) to the point absorbers reduces the magnitude of the forces they experience [25]. It is cumbersome to fully submerge a WEC that has its PTO installed above the water line. Also, extreme waves cause point absorbers to undergo large displacements. The undamped motion causes damage to the floater or the mounting structure. Also, damping the large displacement of a floater by a PTO requires a large energy input to the system and introduces much stress to the PTO.

In order to gain an understanding on the behavior of WECs under extreme waves, one can adopt different techniques, such as theoretical, computational, and experimental methods. Computational Fluid Mechanics methods in the Lagrangian description such as Smoothed Particle Hydrodynamics (SPH) are effective ways to model the wave structure interaction. Specifically, SPH method can be used to model different types of surface waves [26–30]. Also, SPH has been used to accurately measure the impact forces on structures by extreme waves [31–36]. Thus, SPH would be an effective method to predict the extreme forces on WECs to help us better predict the survivability of similar devices.

The "Berkeley Wedge" (TBW) [5] is an asymmetric wave energy converter (AWEC) and breakwater. It consists of an asymmetric floater, a power take-off (PTO) system, and a support structure. The particular shape of the floater, depicted in Fig. 2.1, was designed to experience minimal effects from viscosity in heave motion. The mounting structure limits the motion of the floater to heave only. The PTO system implemented in the design is a linear permanent magnet generator (LPMG) [37–40]. When the damping of the LPMG is matched with the heave radiation damping of the floater at resonance, there will be almost no reflected or transmitted waves and almost all of the incident wave energy will be absorbed by the damping of the LPMG. TBW can be used near shore to provide electricity for local communities and act as a breakwater (concurrently) to protect the harbor with minimal environmental impact. It can also be attached to offshore structures and floating platforms to provide electricity and protect the structure. In a recent study [41], the particular asymmetric shape of TBW was implemented in a coaxial wave energy converter (consisting of a fixed inner cylinder and moving outer cylinder) to reduce the viscous effects on the heave motion of the outer cylinder. The experimental testing revealed that the shape of TBW reduced the viscous damping on the heave displacement of the outer cylinder by

70%, resulting in an increase in the heave displacement of the outer cylinder by more than 300%.

The first part of this thesis begins by describing TBW device concept. This is followed by construction of the heave time-domain equation of motion to provide the preliminaries for extension into its spectral representation. The upper and lower bounds on the TAP, surge-restraining force, pitch-restraining torque, and PTO actuator force are calculated while assuming that the WEC motion was constrained but remains sinusoidal. The upper bound was calculated assuming an optimum phase between the heave wave-exciting force and heave velocity while the lower bound assumes that the PTO system consists only of a linear resistive damper, and in both cases the PTO force coefficients are constant and continuous throughout the wave cycle. Next, pseudo-spectral control theory is reviewed followed by incorporating the surge-restraining force, pitch-restraining torque, and PTO actuator force into the optimization problem. A penalty weight is placed on the contributions to the objective function from the restraining and PTO loads to allow the desired performance to be achieved. The effect of including the restraining loads on balancing power absorption and load shedding is first explored by varying the penalty weight magnitudes and comparing against the known performance bounds. The time history of WEC motion and PTO control force are presented to illustrate how per-unit increases in TAP can exceed the per-unit increase in restraining and PTO loads while having a minimal reactive power requirement.

The second part of this thesis analyzes the survivability of TBW. We establish a computational technique to produce the deep-water plunging breakers. Then, we conduct computations and experiments to analyze the wave exciting forces on TBW. Finally, by comparing the experimental findings with the computational predictions, we introduce minimal design changes (without altering the efficiency) for improving the survivability of these kinds of devices in breaking waves.

Chapter 2

Time-Domain Solution in Regular Waves

2.1 Asymmetric Point Absorbers

For the canonical problem of study we examine TBW, an asymmetric wave energy converter (WEC) and breakwater. The idea of a needle shape AWEC with high efficiency that can concurrently act as a breakwater was originally introduced in 1983 [42]. Then, the concept was experimentally tested in 2012 [5]. The system that is called TBW, consists of an asymmetric floater (AF), a power take-off (PTO) system, and a support structure. The particular shape of the AF, depicted in Fig. 2.1, was designed to experience minimal effects from viscosity in heave motion. The mounting structure limits the motion of the AF to heave only. The PTO system implemented in the design is a linear permanent magnet generator (LPMG) that requires no gearing system. When the damping of the LPMG is matched with the heave radiation damping of the AF at resonance, almost all of the incident wave energy will be absorbed by the damping of the LPMG.

The physical dimensions of the AF were chosen to fit the model testing facility at the University of California at Berkeley. A detailed theoretical and experimental study [5] confirmed the effectiveness of the design in reducing the viscous effect on the motion of the device, thereby capturing almost all of the incident wave energy and providing a calm water surface leeward of the AF.

In this chapter we examined TBW with the design dimensions of the AF shown in Table 2.1 and in the next chapter, other beam and drafts of the AF were adopted. The particular shape of the AF (Fig. 2.1) can be obtained from

$$\mathscr{F}(\bar{y}) = 0.05926(\bar{y}+1)^2 + 3.88147(\bar{y}+1)^3 - 2.94074(\bar{y}+1)^4 \tag{2.1}$$

In Eqn. (2.1), $\bar{x} = \mathscr{F}(\bar{y})$ is a shaping function, and $\bar{x} = x/b$ and $\bar{y} = y/d$ are nondimensional scales. In this equation, $\bar{y}$ can be shifted to obtain different drafts. The hydrodynamics coefficients for the AF were obtained from the two-dimensional (2D) potential-flow code RWYADMXA [43] and all shown in nondimensional form in Fig. 2.2.

In order to analyze the optimal energy extraction efficiency of TBW, the relation between heave wave exciting force, heave radiated damping, and far-field radiated wave amplitudes will be discussed. Far-field radiated waves are generated as result of heave displacement of the AF. They propagate away from the AF (Fig. 2.1) facing positive ($A_j^+ e^{-ikx}$) and negative ($A_j^- e^{ikx}$) x-coordinate. The heave wave exciting force can be obtained from far-field radiated wave amplitudes in deep water by using the Haskind Relation (see Appendix A for the

Table 2.1: Geometric values of the AF.

Water Depth, h, 1.5 m	Draft, d, 0.7 m
Beam, b, 0.212 m	Area, S, 0.067 m^2
Center of Gravity, x_g, -0.0848 m	Resonance, T_{res}, 1.25 s

derivation).

$$\frac{X_j}{A} = -\frac{\rho g^2}{\sigma^2} A_j^- \tag{2.2}$$

We can denote the geometry-hydrodynamic factor, γ, to the ratio of left (A_j^-) and right (A_j^+) far-field radiated wave amplitudes.

$$\gamma = \left| \frac{A_j^+}{A_j^-} \right| \tag{2.3}$$

At this point if we equate the work done by an oscillator on the fluid and the energy propagation associated with the far-field wave amplitudes, we obtain the following expression (see Appendix B for details).

$$|X_2|^2 = \frac{2\rho g^2}{\sigma} \frac{\lambda_{22}}{1+\gamma^2} \tag{2.4}$$

With having the above expression we can obtain the optimal energy extraction efficiency for TBW which will be discussed in latter sections.

.

2.2 Time-Domain-Heave Equation of Motion

The one-degree-of-freedom time-domain-heave equation of motion is given by

$$m\ddot{\zeta}_2(t) = f_{e2}(t) + f_{r22}(t) + f_h(t) + f_d(t) + f_m(t) \tag{2.5}$$

where t is time, m is the mass of the WEC, $\ddot{\zeta}_2$ is the heave acceleration, f_{e2} is the wave-exciting heave force caused by the incident waves, f_{r22} is the wave radiation force caused by heave motion, f_h is the hydrostatic restoring force, f_d is the drag force caused by viscous effects, and f_m is the mechanical force applied by the PTO system.

The heave hydrostatic restoring force is given by

$$f_h(t) = -C_{22}\zeta_2(t) \ , \quad \text{with} \ \ C_{22} = \rho g b \tag{2.6}$$

[1] $\bar{\sigma} = \sigma\sqrt{b/g}$, $\bar{\mu}_{22} = \mu_{22}/\rho b^2$, $\bar{\lambda}_{22} = \lambda_{22}/\rho b^2\sigma$, $\bar{X}_2 = X_2/\rho g b$, $\bar{\phi}_2 = \phi_2/\pi$, $\bar{\mu}_{12} = \mu_{12}/\rho b^2$, $\bar{\lambda}_{12} = \lambda_{12}/\rho b^2$, $\bar{X}_1 = X_1/\rho g b$, $\bar{\phi}_1 = \phi_1/\pi$, $\bar{\mu}_{32} = \mu_{32}/\rho b^3$, $\bar{\lambda}_{32} = \lambda_{32}/\rho b^3\sigma$, $\bar{X}_3 = X_3/\rho g b^2$, $\bar{\phi}_3 = \phi_3/\pi$

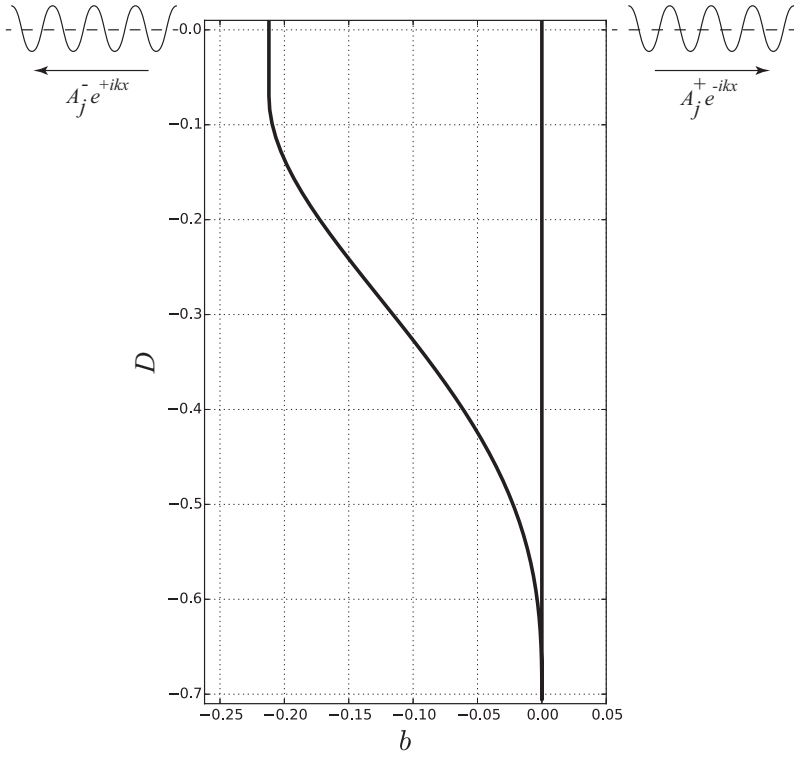

Figure 2.1: 2D shape of the AF with the beam $b = 0.212\ m$ and draft $D = 0.7\ m$.

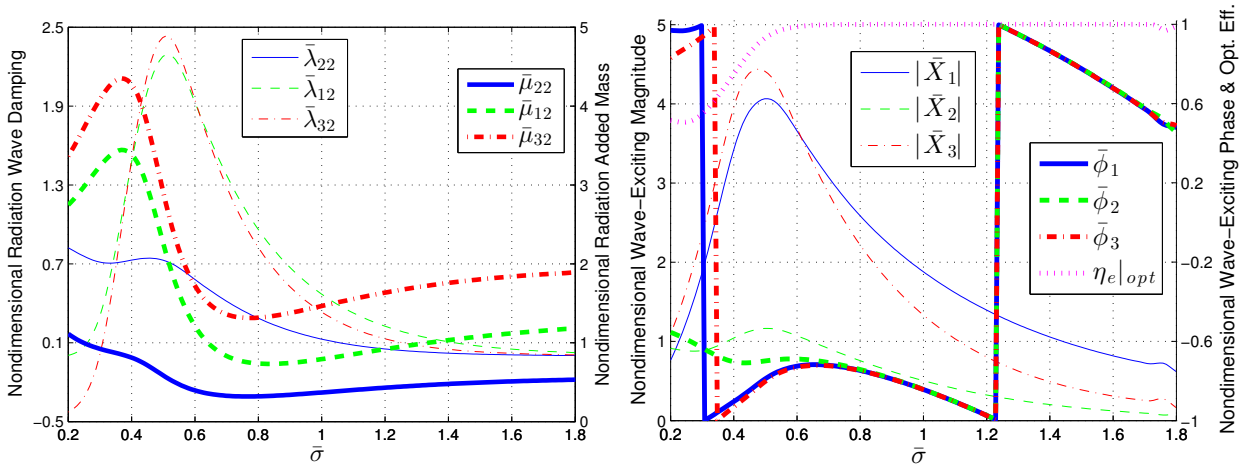

Figure 2.2: Nondimensional 2D hydrodynamic radiation and wave-exciting coefficients[1].

where ρ is the fluid density, g is the gravitational acceleration, b is the device beam length at the calm water line, and ζ_2 is the time-varying heave displacement.

The linear hydrodynamic wave-radiation heave force will be represented in the time domain using the Cummins equation [44] and is written as follows

$$f_{r22}(t) = -\mu_{22}(\infty)\,\ddot{\zeta}_2(t) - \int_{-\infty}^{t} K_{r22}(t-\tau)\,\dot{\zeta}_2(\tau) \tag{2.7}$$

where $\mu_{22}(\infty)$ is the heave-added mass at infinite frequency, and K_{r22} is the heave radiation impulse response function, also known as the memory function because it represents the wave radiation memory effect caused by past WEC motions. The relations between the time- and frequency-domain radiation coefficients were derived in [45]

$$K_{r22}(t) = \frac{2}{\pi}\int_{0}^{\infty} \lambda_{22}(\sigma)\cos(\sigma t)\,d\sigma \tag{2.8}$$

$$K_{r22}(t) = -\frac{2}{\pi}\int_{0}^{\infty} \sigma\left[\mu_{22}(\sigma) - \mu_{22}(\infty)\right]\sin(\sigma t)\,d\sigma \tag{2.9}$$

where $\mu_{22}(\sigma)$ and $\lambda_{22}(\sigma)$ are the frequency-dependent hydrodynamic radiation coefficients commonly known as the added mass and wave radiation damping.

The wave-exciting heave force can be written in the time domain as follows

$$f_{e2}(t) = \int_{-\infty}^{\infty} K_{e2}(t-\tau)\,\eta(\tau)\,d\tau \tag{2.10}$$

where K_{e2} is the heave wave-excitation kernel, which is noncausal, and η is the wave elevation. The relationship between the time- and frequency-domain excitation coefficients is given by

$$K_{e2}(t) = \frac{1}{\pi}\int_{0}^{\infty} \left[\Re\left\{X_2(\sigma)\right\}\cos(\sigma t) - \Im\left\{X_2(\sigma)\right\}\sin(\sigma t)\right]d\sigma \tag{2.11}$$

where X_2 is the frequency-dependent complex wave-exciting heave-force coefficient, $\Re$ is the real component, and $\Im$ is the imaginary component.

The drag force is represented by either of the following

$$f_d(t) = \begin{cases} -\lambda_{vl}\dot{\zeta}_2(t) \\ -\lambda_{vn}\dot{\zeta}_2(t)\left|\dot{\zeta}_2(t)\right| \end{cases} \tag{2.12}$$

where λ_{vl} is the linear-drag coefficient caused by the presence of viscosity, and λ_{vn} is the quadratic-drag coefficient, assuming they are not negligible. The final one-degree-of-freedom heave equation of motion can now be written as

$$\begin{aligned}(m+\mu_{22}(\infty))\,\ddot{\zeta}_2(t) = &-C_{22}\zeta_2(t) - \lambda_{vl}\dot{\zeta}_2(t) \\ &- \int_{-\infty}^{t} K_{r22}(t-\tau)\,\dot{\zeta}_2(\tau)\,d\tau + \int_{-\infty}^{\infty} K_{e2}(t-\tau)\,\eta(\tau)\,d\tau + f_m(t)\end{aligned} \tag{2.13}$$

where the linear form of the drag force has been used.

2.2.1 Regular Wave Analysis

It is common practice to begin analysis under regular wave excitation in which the incident wave elevation is described by

$$\eta(x,t) = \Re\left\{-\frac{1}{g}\frac{\partial\phi_0}{\partial t}\bigg|_{z=h}\right\} = \Re\left\{Ae^{i(\sigma t-kx)}\right\} = A\cos(\sigma t - kx) \tag{2.14}$$

where η is the wave elevation, ϕ_0 is the incident wave potential, A is the wave amplitude, σ is the wave angular frequency, k is the wave number, and $i = \sqrt{-1}$ is the imaginary unit. The time-harmonic heave response is then given by

$$\zeta_2(t) = \Re\left\{\xi_2 e^{i\sigma t}\right\} \tag{2.15}$$

where ξ_2 is the complex amplitude of pitch displacement.

Under regular wave excitation, the radiation-convolution integral can be simplified to

$$f_{r22}(t) = -\Re\left\{\left[-\sigma^2\mu_{22}(\sigma) + i\sigma\lambda_{22}\right]\xi_2 e^{i\sigma t}\right\} \tag{2.16}$$

The wave-excitation-convolution integral can be written as

$$f_{e2}(t) = \Re\left\{AX_2(\sigma)\,e^{i\sigma t}\right\} \tag{2.17}$$

For the time being, the mechanical force from the PTO system will be described by the following

$$f_m(t) = -\Re\left\{\left(C_g - \sigma^2\mu_g + i\sigma B_g\right)\xi_2 e^{i\sigma t}\right\} \tag{2.18}$$

where C_g is the linear PTO-restoring coefficient, B_g is the PTO linear-damping coefficient, and μ_g is the additional PTO inertia. The frequency-domain expressions can be inserted into Eqn. (2.13), leading to the heave-displacement response amplitude operator as

$$\frac{\xi_2}{A} = \frac{X_2}{\left[C_{22} - \sigma^2(m+\mu_{22}) + C_g - \sigma^2\mu_g\right] + i\sigma\left[\lambda_{22} + B_g\right]} \tag{2.19}$$

where λ_{vl} has been set to zero since results as [5] saw minimal effects from viscosity.

2.2.1.1 PTO Absorbed Power

The TAP absorbed by the PTO is calculated from

$$\frac{P_T}{A^2} = \frac{1}{2} B_g \sigma^2 \left| \frac{\xi_2}{A} \right|^2 \tag{2.20}$$

Equation (2.19) can be inserted into Eqn. (2.20) to calculate the optimal PTO damping at each wave frequency. The optimal, unconstrained, time-averaged absorbed power and PTO damping at each wave frequency is given by

$$\left. \frac{P_T}{A^2} \right|_p = \frac{1}{4} \frac{|X_2|^2}{\lambda_{22}} \frac{1}{1 + \sqrt{1 + \left(\frac{C_{22} + C_g - \sigma^2 (m + \mu_{22} + \mu_g)}{\sigma \lambda_{22}} \right)^2}} \tag{2.21}$$

$$B_g|_p = \lambda_{22} \sqrt{1 + \left(\frac{C_{22} + C_g - \sigma^2 \left(m + \mu_{22} + \mu_g \right)}{\sigma \lambda_{22}} \right)^2} \tag{2.22}$$

where P_T is frequency dependent and at resonance $B_g = \lambda_{22}$, leading to the maximum time-averaged absorbed power [46]. Because these expressions do not consider motion constraints, it may be necessary to increase the PTO damping to remain under a given limit. The required PTO damping is given by

$$B_g|_{pc} = \left\{ \left(\frac{A|X_2|}{\sigma |\xi_2|_{max}} \right)^2 - \left[\frac{C_{22} + C_g}{\sigma} - \sigma \left(m + \mu_{22} + \mu_g \right) \right]^2 \right\}^{1/2} - \lambda_{22} \tag{2.23}$$

where $|\xi_2|_{max}$ is the maximum amplitude of heave displacement [47].

To provide a measure of efficiency for a given device, the TAP contained within a propagating wave must be known. The time-averaged wave power per-unit width, P_w, can be obtained from

$$P_w = \frac{1}{4} \rho g A^2 \sqrt{\frac{g}{k} \tanh kh} \left[1 + \frac{2kh}{\sinh kh} \right] \approx \left. \frac{1}{4} \frac{\rho g^2 A^2}{\sigma} \right|_{kh \to \infty} \tag{2.24}$$

where h is the water depth.

We denote η_e as the ratio of TAP absorbed by the PTO per the incident wave energy flux. Substituting the expression of heave wave exciting force, Eqn. (2.4), into the modulus of the expression for the heave-displacement response amplitude operator, Eqn. (2.19), and using the maximum TAP condition, $B_g = \lambda_{22}$, the expression for optimal energy extraction efficiency as a function of geometry-hydrodynamics factor, γ, is obtained.

$$\eta_e|_{\text{opt}} = \frac{1}{1 + \gamma^2} \tag{2.25}$$

To obtain maximum extraction efficiency ($\eta_e = 1$), γ needs to be equal to 0. This is possible by having the right far-field radiated wave amplitude equal to zero ($A_j^+ = 0$) and the left

far-field radiated wave amplitude be finite ($A_j^- \neq 0$). For symmetric floaters both right and left far-field wave amplitudes will be equal ($A_j^- = A_j^+$), so $\gamma = 1$, which results in $\eta_e|_{\text{opt}} = 0.5$ if the maximum time-averaged absorbed power condition is satisfied. The graph of $\eta_e|_{\text{opt}}$ for TBW is shown in Fig. 2.2.

2.2.1.2 Maximum Power Under Constrained Motion

The maximum power absorption under motion constraints, while assuming sinusoidal motion, was explored in [48] which led to the following expression

$$\left.\frac{P_T}{A^2}\right|_{mc} = \frac{1}{8}\frac{|X_2|^2}{\lambda_{22}}\left[1 - H\left(1-\delta\right)\left(1-\delta\right)^2\right] \tag{2.26}$$

where $H(x)$ is the Heaviside step function, and δ is the ratio between the constrained-to-optimal heave velocity given by

$$\delta = \frac{\sigma|\xi_2|_{max}}{A}\frac{2\lambda_{22}}{|X_2|} \tag{2.27}$$

Equation (2.26) can be expanded to show the trends in time-averaged absorbed power for the ranges of δ.

$$P_T|_{mc} = \begin{cases} \frac{1}{8}A^2|X_2|^2/\lambda_{22} & \delta > 1 \\ \frac{1}{2}A|X_2|\sigma|\xi_2|_{max} - \lambda_{22}\sigma^2|\xi_2|^2_{max} & \delta < 1 \end{cases} \tag{2.28}$$

The capture width, defined as the ratio between the TAP absorbed by the PTO and the incident wave power per-unit width and is a metric used to evaluate the absorption efficiency of the device. The incident wave power is proportional to the incident wave amplitude squared, see Eqn. (2.24). For unconstrained motion, which may also correspond to a very small incident wave amplitude, the capture width will be invariant to the incident wave height; whereas for a strongly constrained motion, which may also correspond to a very large incident wave amplitude, the capture width will be inversely proportional to the incident wave height and become less efficient.

The associated PTO linear-damping coefficient to observe the motion constraint is given by

$$B_g|_{mc} = \lambda_{22}\left[1 + \frac{2\left(1-\delta\right)}{\delta}H\left(1-\delta\right)\right] = \begin{cases} \lambda_{22} & \delta > 1 \\ \frac{A|X_2|}{\sigma|\xi_2|_{max}} - \lambda_{22} & \delta < 1 \end{cases} \tag{2.29}$$

where the PTO spring and inertia coefficients cancel the dynamic force contribution from the natural body-restoring coefficient, mass, and hydrodynamic added mass

$$C_g - \sigma^2\mu_g = -\left[C_{22} - \sigma^2\left(m + \mu_{22}\right)\right] \tag{2.30}$$

which is the basis of complex conjugate control [18]. Often in power quality management it is desirable to have the peak-to-average power ratio as close as possible to eliminate the need for advanced signal conditioning. Under complex conjugate control the peak-to-average power ratio, $P_{\pm}$, is given by [47] (see Appendix C)

$$P_{\pm} = 1 \pm \sqrt{1 + \left[\frac{C_{22} - \sigma^2 (m + \mu_{22})}{\sigma B_g}\right]^2} \tag{2.31}$$

When there is no reactive power, $X_g = \sigma\mu_g - C_g/\sigma = 0$, the peak-to-average power ratio is 2 and the instantaneous power oscillates between 0 and $2P_T$. The reactive component is eliminated at the resonance frequency of the isolated floating body and the peak-to-average power ratio is minimized at 2; however, when away from the resonant frequency, the peak-to-average power ratio quickly increases, resulting in large swings in the bidirectional energy flow.

2.2.2 Foundation Reaction Force and Moment

The structural foundation must handle the reaction force and torque needed to restrain the WEC to heave motion. The reaction force in the surge, X_{r1}, and pitch, X_{r3}, modes of motion are given by

$$A (X_{r1} + X_1) = [-\sigma^2 \mu_{12} + i\sigma\lambda_{12}] \xi_2 \tag{2.32}$$

$$A (X_{r3} + X_3) = [-\sigma^2 (x_g m + \mu_{32}) + i\sigma\lambda_{32}] \xi_2 \tag{2.33}$$

where X_1 and X_3 are the complex surge wave-exciting force and pitch wave-exciting torque coefficients per unit wave amplitude, μ_{12} is the surge-heave added mass, and λ_{12} is the surge-heave wave radiation damping, μ_{32} is the pitch-heave added mass, λ_{32} is the pitch-heave wave radiation damping, and x_g is the horizontal center of gravity. The surge and pitch foundation reaction force and torque are affected by the heave motion of the WEC, which can be controlled by the PTO. The time-domain corollary of Eqns. (2.32) and (2.33) is given by

$$f_{r1}(t) = -\int_{-\infty}^{\infty} K_{e1}(t-\tau)\,\eta(\tau)\,d\tau + \mu_{12}(\infty)\,\ddot{\zeta}_2(t) + \int_{-\infty}^{t} K_{r12}(t-\tau)\,\dot{\zeta}_2(\tau)\,d\tau \tag{2.34}$$

$$\begin{aligned} f_{r3}(t) = -\int_{-\infty}^{\infty} K_{e3}(t-\tau)\eta(\tau)\,d\tau + (x_g m + \mu_{32}(\infty))\,\ddot{\zeta}_2(t) + \\ \int_{-\infty}^{t} K_{r32}(t-\tau)\,\dot{\zeta}_2(\tau)\,d\tau \end{aligned} \tag{2.35}$$

2.2.3 Results from Fixed-PTO Coefficients

Maximizing the TAP, as described in previous sections, involves the PTO coefficients to be fixed in time although adapted for a given wave amplitude and angular frequency. Performance bounds can be set for the TAP, surge-restraining force amplitude, pitch-restraining torque amplitude, and PTO control force amplitude, which have been plotted in Fig. 2.3. A benefit of the current design can be observed in the bottom plot of Fig. 2.3, where the heave amplitude and phase required for elimination of the surge-restraining force and pitch-restraining torque are presented. The surge and pitch components require a very similar amplitude and phase for elimination, which will lead to a reduction in both if only one contribution is heavily penalized in the controller. It is expected that time-varying PTO coefficients can help optimize the time-averaged absorbed power while reducing loads, leading to device performance that sits between the maximum constrained and passive curves.

2.3 Pseudo-Spectral Control

The discretization of the control problem is completed by approximating the heave velocity and PTO force with a linear combination of basis functions [16, 49]. The heave velocity, $\dot{\zeta}_2$, and PTO force, f_m, are approximated by a zero-mean truncated Fourier series with N terms as follows

$$\dot{\zeta}_2(t) \approx \sum_{j=1}^{N/2} \psi_j^c \cos(j\sigma_0 t) + \psi_j^s \sin(j\sigma_0 t) = \Phi(t)\,\hat{\psi} \tag{2.36}$$

$$f_m(t) \approx \sum_{j=1}^{N/2} \tau_j^c \cos(j\sigma_0 t) + \tau_j^s \sin(j\sigma_0 t) = \Phi(t)\,\hat{\tau} \tag{2.37}$$

where

$$\hat{\psi} = \left[\psi_1^c, \psi_1^s, \ldots, \psi_{\frac{N}{2}}^c, \psi_{\frac{N}{2}}^s\right]^\top, \quad \hat{\tau} = \left[\tau_1^c, \tau_1^s, \ldots, \tau_{\frac{N}{2}}^c, \tau_{\frac{N}{2}}^s\right]^\top \tag{2.38}$$

$$\begin{aligned}\Phi(t) &= [\phi_1(t), \phi_2(t), \ldots, \phi_{N-1}(t), \phi_N(t)] \\ &= \left[\cos(\sigma_0 t), \sin(\sigma_0 t), \ldots, \cos\left(\frac{N}{2}\sigma_0 t\right), \sin\left(\frac{N}{2}\sigma_0 t\right)\right]\end{aligned} \tag{2.39}$$

with the fundamental frequency given by $\sigma_0 = 2\pi/T$ and T is the chosen time duration. The heave equation of motion can be described as follows

$$M_{22}\hat{\psi} = \hat{\tau} + \hat{e}_2 \tag{2.40}$$

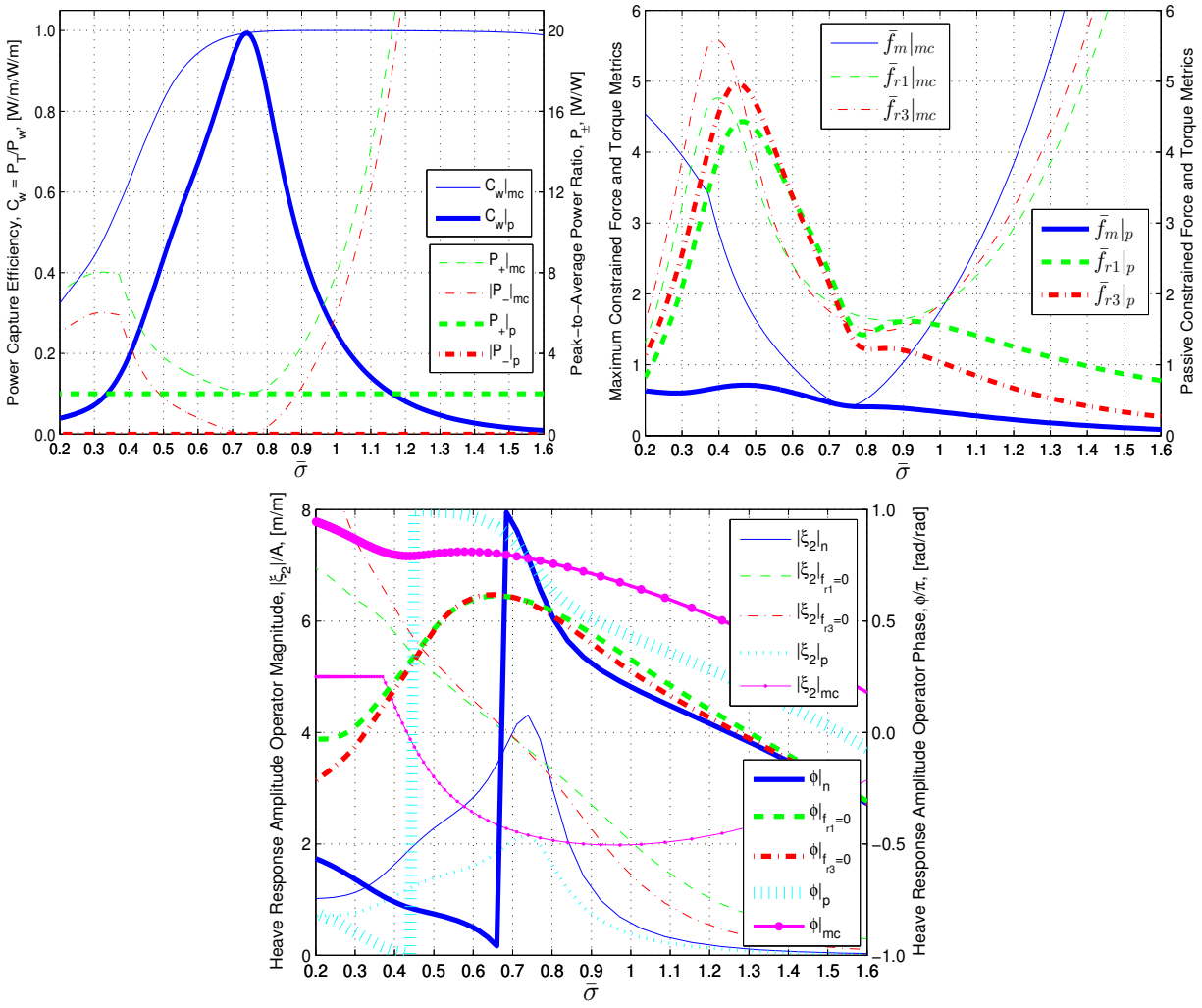

Figure 2.3: Performance bounds under a heave-displacement amplitude constraint of 0.1 m and a wave amplitude of 0.02 m. The subscript $_p$ denotes passive performance as given by Eqns. (2.20)–(2.23). The subscript $_{mc}$ denotes maximum constrained performance as given by Eqns. (2.26)–(2.30). The subscript $_n$ denotes the natural heave motion (no PTO), whereas $_{f_{r1}} = 0$ and $_{f_{r3}} = 0$ denote heave motion required to eliminate the surge-restraining force and pitch-restraining torque. The nondimensional force and torque values are given by: $\bar{f_m} = f_m/\rho g b A$, $\bar{f_{r1}} = f_{r1}/\rho g b A$, and $\bar{f_{r3}} = f_{r3}/\rho g b^2 A$.

where $\hat{e}_2$ is the Fourier coefficient vector of the heave wave-exciting force. The matrix $M_{22} \in \mathbb{R}^{N\times N}$ is block diagonal with the following structure

$$M_{22}^j = \begin{bmatrix} \lambda_{22}(j\sigma_0) & \alpha(j\sigma_0) \\ -\alpha(j\sigma_0) & \lambda_{22}(j\sigma_0) \end{bmatrix} \quad \text{for} \quad j = 1, 2, \ldots, N/2$$
$$\alpha(j\sigma_0) = j\sigma_0 (m + \mu_{22}(j\sigma_0)) - C_{22}/(j\sigma_0) \tag{2.41}$$

The heave velocity coefficients can then be determined explicitly from the control and heave wave-exciting force Fourier coefficients. This representation allows the total absorbed energy, E, to be written as

$$E = -\int_0^T \dot{\zeta}_2(t) f_m(t)\, dt = -\frac{T}{2}\hat{\psi}^\top \hat{\tau} = -\frac{T}{2}\left[\hat{\tau}^\top \left(M_{22}^{-1}\right)^\top \hat{\tau} + \hat{e}_2^\top \left(M_{22}^{-1}\right)^\top \hat{\tau}\right] \tag{2.42}$$

which is in the form of a traditional quadratic problem.

2.3.1 Penalty Terms

2.3.1.1 Surge Foundation Force

Load reduction will consist of limiting the forces on the WEC structure that are required to maintain the heave-only constraint. This force has two contributions that arise from the surge wave-exciting force and WEC motion. The equation for the surge foundation force can be written in a matrix form, similar to Eqn. (2.40), as follows

$$\Phi(t)\hat{f}_{r1} = -\Phi(t)\hat{e}_1 + \mu_{12}(\infty)\Gamma\hat{\psi} + \Phi(t)(G_{12} - \mu_{12}(\infty)\Gamma)\hat{\psi}$$
$$\hat{f}_{r1} = -\hat{e}_1 + G_{12}\hat{\psi} = -\hat{e}_1 + G_{12}M_{22}^{-1}\hat{\tau} + G_{12}M_{22}^{-1}\hat{e}_2 \tag{2.43}$$

where $\hat{e}_1$ is the Fourier coefficients of the surge wave-exciting force, G_{12} and Γ are block matrices given in the Appendix C and Eqn. (2.40) has been substituted in the last expression. To maintain the convexity of the quadratic problem, the squared ℓ^2-norm of the surge-foundation force vector was added to the objective function. The objective function is given by

$$\begin{aligned} \gamma_1|f_{r1}|^2 &= \gamma_1 \int_0^T \hat{f}_{r1}^\top \Phi(t)^\top \Phi(t)\hat{f}_{r1} dt = \frac{T}{2}\hat{f}_{r1}^\top \hat{f}_{r1} \\ &\approx \gamma_1 \frac{T}{2}\Big(2\left[\hat{e}_1^\top G_{12}M_{22}^{-1} - \hat{e}_2^\top \left(M_{22}^{-1}\right)^\top G_{12}^\top G_{12}M_{22}^{-1}\right]\hat{\tau} \\ &\qquad -\hat{\tau}^\top \left(M_{22}^{-1}\right)^\top G_{12}^\top G_{12}M_{22}^{-1}\hat{\tau}\Big) \end{aligned} \tag{2.44}$$

where γ_1 is a penalty weight applied to the surge foundation force. In the final expression for the surge-foundation force contribution, there are three constant terms independent of the PTO control force, which are left out of the optimization See [17] for the full expression.

2.3.1.2 Pitch Foundation Torque

Similar to the surge-restraining force, the pitch-restraining torque has two contributions that arise from the pitch wave-exciting torque and WEC motion. The matrix form of the pitch-restraining torque can be written as

$$\hat{f}_{r3} = -\hat{e}_3 + G_{32}\hat{\psi} = -\hat{e}_3 + G_{32}M_{22}^{-1}\hat{\tau} + G_{32}M_{22}^{-1}\hat{e}_2 \tag{2.45}$$

where $\hat{e}_3$ represents the Fourier coefficients of the pitch wave-exciting torque. As with the surge-restraining force, the squared ℓ^2-norm of the pitch-restraining torque vector was added to the objective function. The foundation torque measure is given by

$$\begin{aligned}
\gamma_3|f_{r3}|^2 &= \gamma_3 \int_0^T \hat{f}_{r3}^\top \Phi\left(t\right)^\top \Phi\left(t\right) \hat{f}_{r3} dt = \frac{T}{2}\hat{f}_{r3}^\top \hat{f}_{r3} \\
&\approx \gamma_3 \frac{T}{2}\Big(2\left[\hat{e}_3^\top G_{32}M_{22}^{-1} - \hat{e}_2^\top \left(M_{22}^{-1}\right)^\top G_{32}^\top G_{32}M_{22}^{-1}\right]\hat{\tau} \\
&\qquad -\hat{\tau}^\top \left(M_{22}^{-1}\right)^\top G_{32}^\top G_{32}M_{22}^{-1}\hat{\tau}\Big)
\end{aligned} \tag{2.46}$$

where γ_3 is a penalty weight applied to the pitch foundation torque.

2.3.1.3 PTO Control Force Magnitude

The PTO force is the only control actuation, and in an effort to reduce computational time and force spikes, a penalty weight was placed on the squared ℓ^2-norm of the PTO force magnitude [12].

$$\beta_m|\tau_m|^2 = \int_0^T \beta_m \tau_m(t)\tau_m(t)dt = \frac{T}{2}\hat{\tau}^\top \beta_m I_N \hat{\tau} \tag{2.47}$$

where β_m is a penalty weight associated with the control force magnitude, and I_N is the identity matrix of size N.

2.3.1.4 Final Objective Function

The objective function will be the sum of the time-averaged absorbed power, the squared ℓ^2-norm of the surge-restraining force, pitch-restraining torque, and control force magnitude. The four contributions to the objective function are not of the same units, and the interrelationship between them is complex. Therefore, the final objective function will consist of the following nondimensional quantities

$$J = \frac{E}{P_w T} + \gamma_1\left|\frac{f_{r1}}{\rho g b A}\right|^2 + \beta_m\left|\frac{f_m}{\rho g b A}\right|^2 + \gamma_3\left|\frac{f_{r3}}{\rho g b^2 A}\right|^2 \tag{2.48}$$

2.4 Pseudo-Spectral Results

2.4.1 Effect of Penalty Terms

Figure 2.4 verifies that the pseudo-spectral controller is achieving the desired results when considering the extremes of the tested penalty weights. As the control force penalty weight, β_m, is increased the magnitude of the PTO control force and reactive power is reduced. As shown for the lowest values of γ_1 and β_m, the highest TAP is achieved; however, a larger reactive power component is required. Whereas for the largest values of γ_1 and β_m, reduction in the surge-restraining force and pitch-restraining torque is counterbalanced by an increase in the PTO control torque. The increase in PTO torque is a result of the amplitude and phase difference between the unforced (no PTO) and zero surge-restraining force heave motion (refer to the bottom plot of Fig. 2.3). It can be observed that both above and below the resonance frequency the unforced heave amplitude of motion is lower than what is required for elimination of the surge-restraining force. As more emphasis is placed on reducing the surge-restraining force, greater control forces and reactive power are required, which implies that complete elimination of the restraining loads may not be desirable.

In Fig. 2.4, the region bounded by $\beta_m \geq 0.8$ and $\gamma_1 \leq 0.4$ is the most favorable as the capture efficiency can be increased between 20%–80% with a reactive power contribution comprising only 1/10th of the TAP. Furthermore, the surge-restraining force (f_{r1}), pitch-restraining moment (f_{r3}), and PTO control torque can be reduced between 10%–30% with respect to the passive values; however, it is evident that the contours will vary depending on the incident wave frequency and most likely on the heave amplitude constraint. The left column of Fig. 2.4 plots a set of results for a wave frequency below resonance. In this frequency range the contours follow nearly straight lines when viewing the γ_1 and β_m space. Here the greatest difference in the heave motion amplitude and phase occurs, requiring a proportionate increase in the PTO control torque to decrease restraining loads. Just below resonance the TAP curve decreases slower than above resonance; however, a greater control effort will be needed to reduce restraining loads. These contour plots provide a clear design space that can be used to optimize power production, decrease structural loads, or achieve many combinations in between.

2.4.2 Time History of WEC and PTO

Figure 2.5 plots the time history of the four points marked in the plots along the right column of Fig. 2.4. In region 1 the maximum power absorption is nearly recovered, in region 2 there is roughly a 50% reduction for all performance metrics compared to maximum absorption, in region 3 the surge-restraining force is prioritized at the expense of larger PTO forces and reactive power, and in region 4 the controller attempts to maximize TAP with reduced PTO forces at the expense of larger restraint loads. As the penalty weights are reduced, the PTO control torque moves the heave velocity closer in phase with the heave

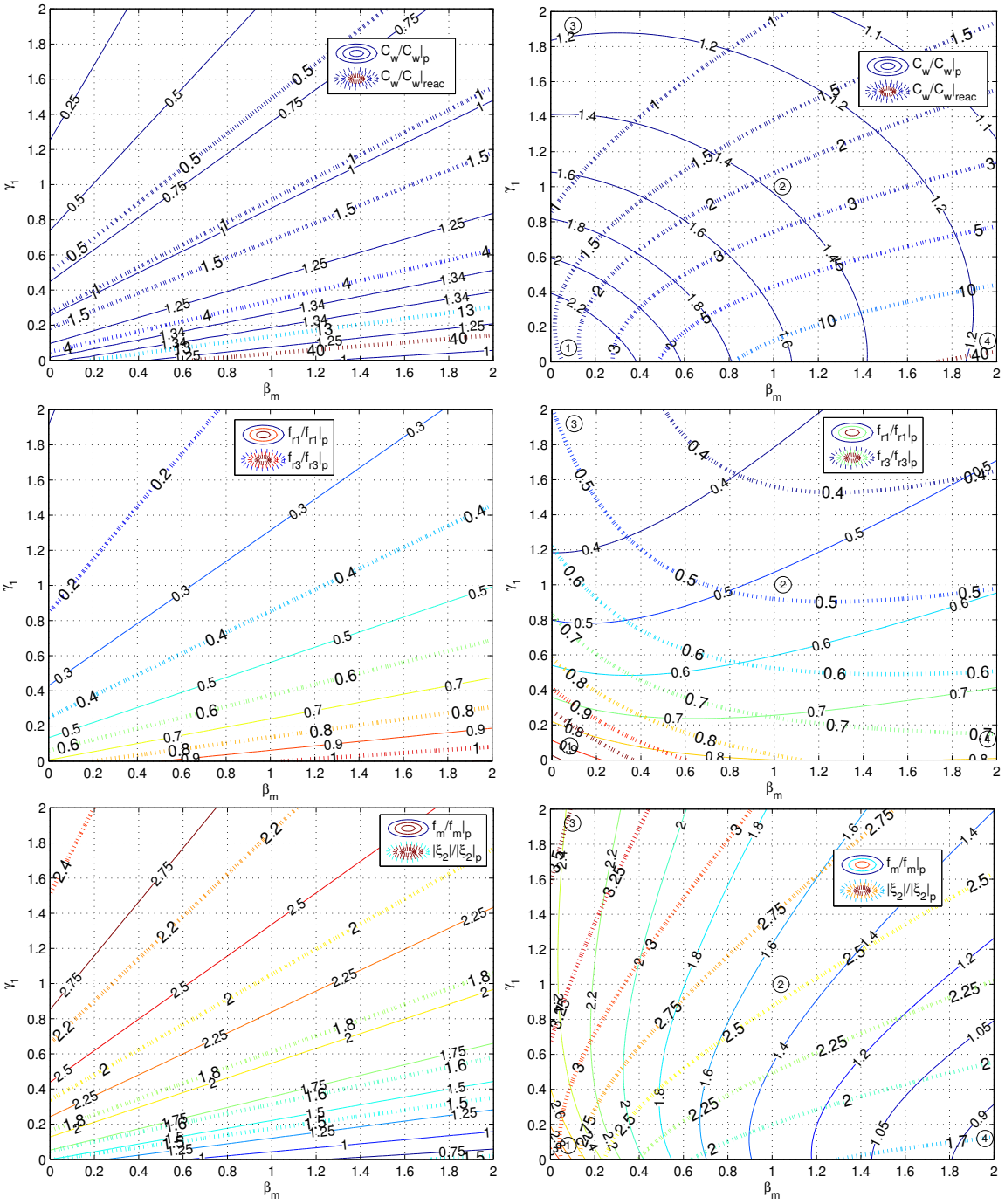

Figure 2.4: Sensitivity of performance metrics to penalty weights under a heave-displacement amplitude constraint of 0.1 m and wave amplitude of 0.02 m. The left column plots results for a wave period of 1.5 s ($\bar{\sigma} = 0.62$) and the right column for a wave period of 1 s ($\bar{\sigma} = 0.92$). The subscript $_p$ denotes passive performance as given by Eqns. (2.20)–(2.23).

wave-exciting force. This phase shift is accompanied by the greatest amplitudes in PTO control torque, surge-restraining force and pitch-restraining torque, but not reactive power. Marker 3 has the greatest reactive power requirement as the amplitude of motion to eliminate the surge-restraining force is greater than the maximum constrained heave profile. As the surge-restraint and PTO force penalty weights are increased, the controller will first maintain a near optimum phase while reducing the amplitude of motion; however, eventually a greater phase shift is introduced by the controller to eliminate a greater proportion of the surge-foundation force; refer to Eqn. (2.32). Further reduction in the restraint loads will then see an increase in the heave amplitude of motion and a corresponding increase in PTO control torque and reactive power. The larger reduction in restraint loads and PTO force can be achieved because of the ability of the controller to induce a phase shift in the heave velocity at the expense of bidirectional energy flow, which can be greatly affected by PTO efficiency [50].

2.4.3 Power-to-Load Ratio

In order to compare the results from pseudo-spectral control over a wider range of wave angular frequencies, a power-to-load ratio was calculated as follows:

$$PL = \frac{P_T/A^2}{\sqrt{\left(f_{r1}/A\right)^2 + \left(f_m/A\right)^2}} \tag{2.49}$$

The TAP was scaled by a factor of A^2, as per Eqn. (2.20), while the surge-restraining force was scaled by a factor of A, as per Eqn. (2.32). For each wave angular frequency the power-to-load ratio was calculated for all penalty weight combinations considered. The maximum contour was taken and plotted against results obtained at different wave angular frequencies, see the top plot of Fig. 2.6. As seen from the plot, there are several combinations of γ_1 and β_m that provide the same power-to-load ratio with the range increasing as the wave frequency moves closer to resonance. As the wave frequency moves away from resonance, the optimum contours shrink and converge towards $\gamma_1 \to 0$ and $\beta_m \to 0$. However, the power-to-load ratio does not consider the reactive power requirement. The contours in the center plot of Fig. 2.6 indicate when the TAP is 10 times greater than the time-averaged reactive power and above these contours the TAP-to-reactive power ratio decreases. All of the optimum power-to-load contours, except for $\bar{\sigma} = 0.77$, sit above the TAP-to-reactive power contours. As seen in Fig. 2.4, this ratio can decrease very quickly as γ_1 increases and β_m decreases resulting in a large reactive power requirement to achieve the optimum power-to-load ratios. A greater reactive power requirement and peak-to-average power ratio may lead to an increase in the levelized cost of energy because of the need for larger accumulators to smooth the power output and meet the required power capacity. The bottom plot in Fig. 2.6 compares the power-to-load ratio obtained from pseudo-spectral control to the maximum constrained and passive strategies. Pseudo-spectral control is successful at providing power-to-load ratios

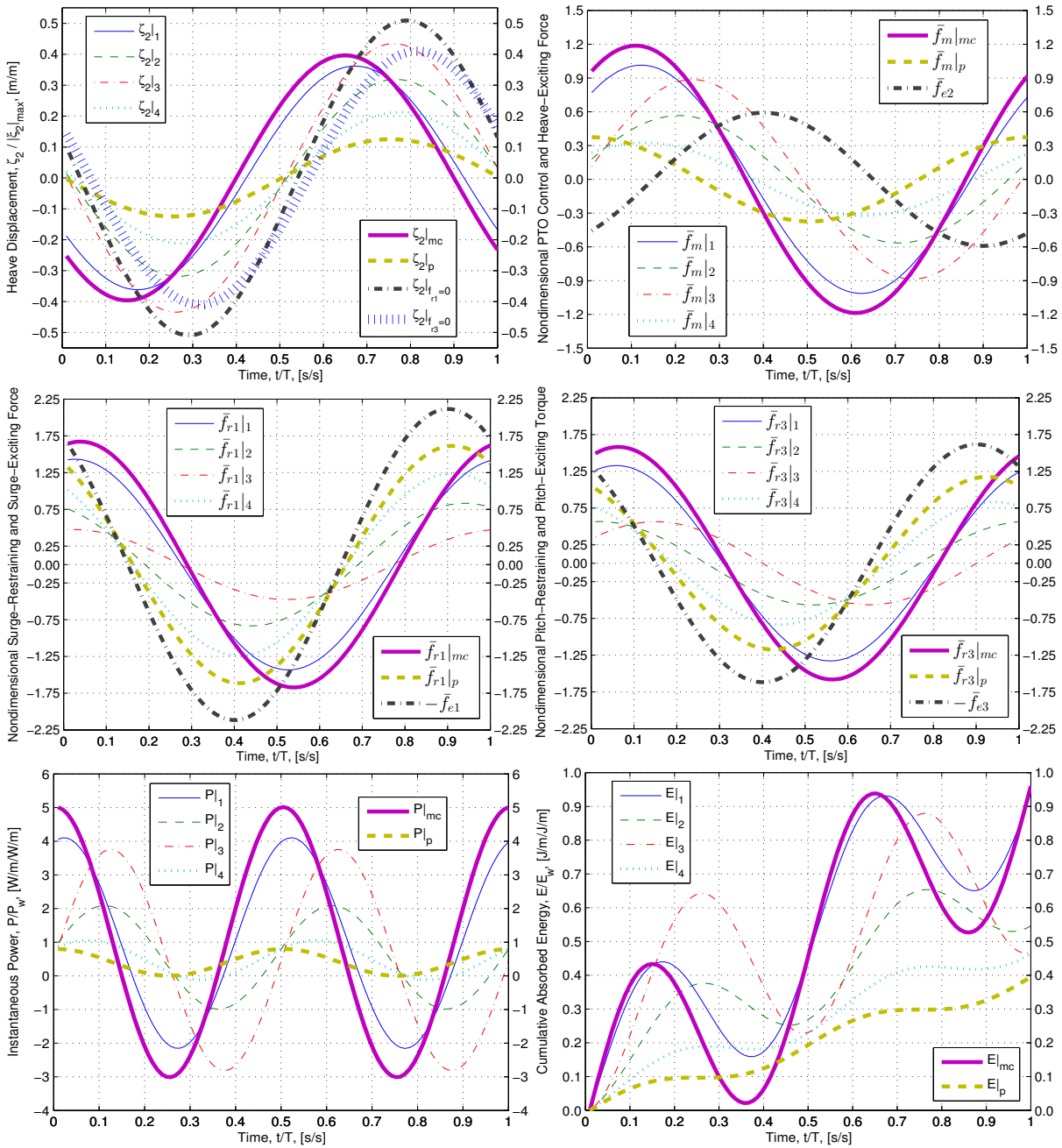

Figure 2.5: Time history of WEC motion, PTO control force, PTO power, restraining force, and restraining torque. Results from applying pseudo-spectral control with $T = 1$ s, $A = 2$ cm, and varying penalty weights. The numbers 1, 2, 3, and 4 in the legend refer to the four markers in the top plot of Fig. 2.4. The subscript $_p$ denotes passive performance as given by Eqns. (2.20)–(2.23). The subscript $_{mc}$ denotes maximum constrained performance as given by Eqns. (2.26)–(2.30). A heave-displacement amplitude limit of 0.1 m was used while the number of fourier coefficients was set at $N = 100$. E_w is the cumulative absorbed energy when assuming perfect absorption.

that are equal to or greater than the maximum constrained values with the largest gains occurring about resonance.

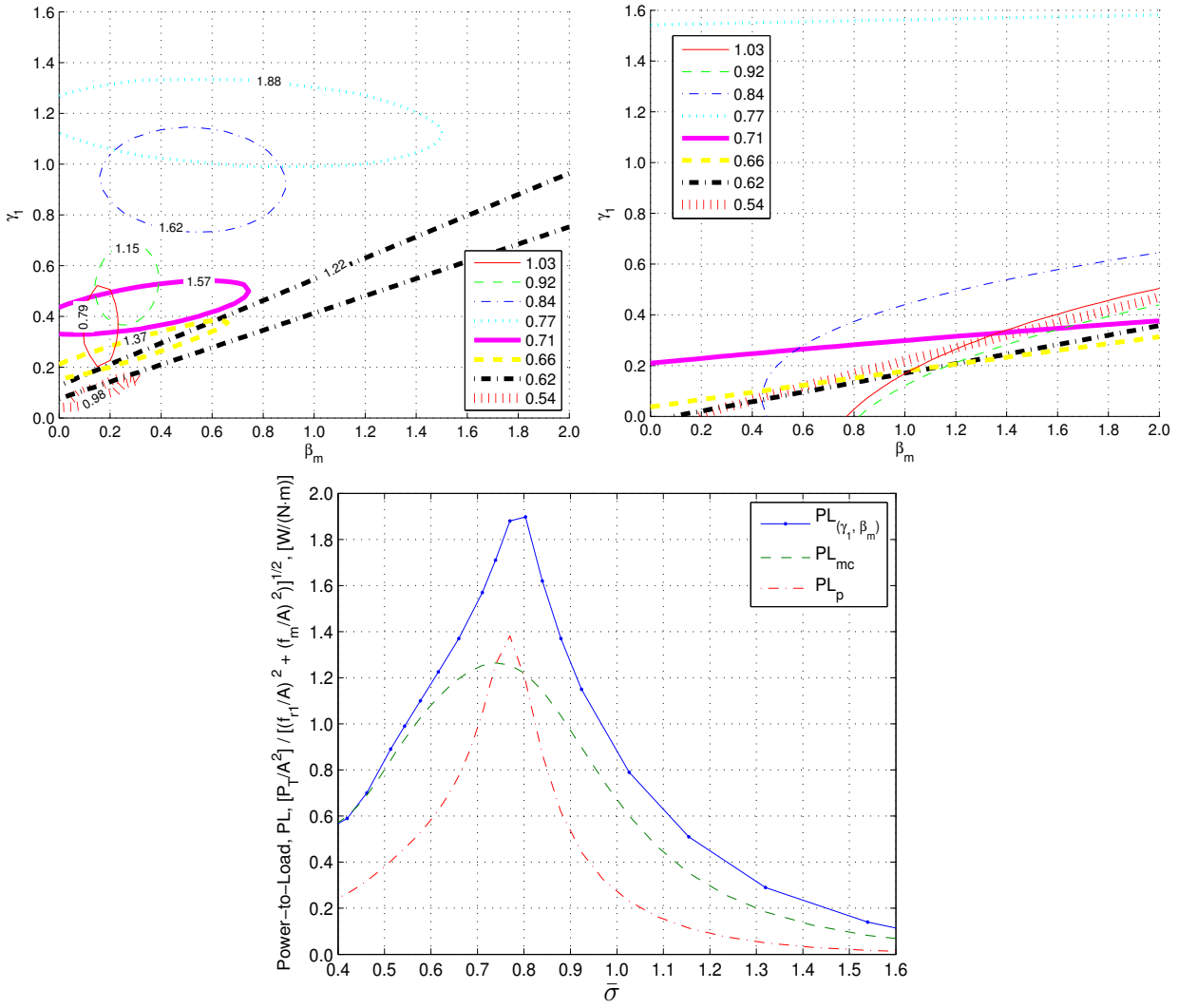

Figure 2.6: Variation of the optimum power-to-load ratio with wave angular frequency. The legend in top two plots denote $\bar{\sigma}$. Top plot displays the contours of the maximum power-to-load ratio at select wave angular frequencies. Center plot displays the contour of the ratio between the TAP and reactive power corresponding to a value of 10. Bottom plot compares the optimum power-to-load ratio obtained from pseudo-spectral control against the maximum constrained and passive results.

Chapter 3

Breaking Waves Modeling and Survivability Condition

3.1 Numerical Method

3.1.1 Lagrangian Frameworks

To analyze the forces of the deep-water plunging breakers on the AF, we used the Lagrangian formulations of the fluid, more specifically the Weakly-Compressible Smooth Particle Hydrodynamics (WCSPH). Studies have shown that breaking waves can be modeled accurately with this formulation [26, 29]. Here we briefly mention the basic equations of the WCSPH scheme. We start with the conservation equations of fluid mechanics and equation of state. The continuity equation is given by

$$\frac{d\rho}{dt} = -\rho \, \nabla \cdot \mathbf{v} \tag{3.1}$$

and the momentum equation by

$$\rho \frac{d\mathbf{v}}{dt} = -\nabla p + \mathbf{f} + \rho \mathbf{g} \tag{3.2}$$

where t, ρ, $\mathbf{v}$, p, $\mathbf{f}$, and $\mathbf{g}$ denote time, density, velocity, pressure, viscous force, and acceleration of gravity respectively. In the weakly-compressive formulation, the equation of state that relates the pressure to density is given by [51, 52]

$$p(\rho) = p_0 \left[(\frac{\rho}{\rho_0})^\gamma - 1 \right] + \chi \tag{3.3}$$

where the exponent γ takes a value between $1 - 7$. The value of $\gamma = 7$ results in a strong pressure response to density variation [53]. The background pressure χ is set to 0 for free surface flows. Also, $p_0 = \rho_0 c_0^2/\gamma$ is the reference pressure, c_0 is the speed of sound, and ρ_0 is the reference density.

3.1.2 WCSPH Scheme

WCSPH is a mesh free scheme to approximate Eqns. (3.1) and (3.2). A smoothing interpolation kernel (W) is used to approximate fluid field variables (density, pressure, and velocity), and in each time step the flow variables are stored in the particles. The smoothing kernel must satisfy the following properties: $\int W(\mathbf{r}, h_a) d\mathbf{r} = 1$, positive definiteness $W(\mathbf{r}, h_a) \geq 0$,

and needs to be even $W(\mathbf{r}, h_a) = W(-\mathbf{r}, h_a)$. Many kernels have been proposed with different degrees of accuracy and time efficiency [51, 54, 55]. We used the quintic spline for computational accuracy [53]. The continuity equation (Eqn. (3.1)) can be approximated by using the smoothing kernel [56] (density of particle a) as

$$\frac{d\rho_a}{dt} = \rho_a \sum_b \frac{m_b}{\rho_b} \mathbf{v}_{ab} \cdot \nabla_a W_{ab} \tag{3.4}$$

where ∇_a is the gradient of the smoothing kernel with respect to the particle a coordinates and $m_b = \rho_a V_a$ is the mass of particle a (the mass of all the particles is kept constant during the computations). The volume of each particle is $V_a = \Delta x^d$ where d is the spacial dimension of the computational domain. Then, the pressure gradient that results in the acceleration of particle a can be approximated by [52]

$$\frac{d\mathbf{v}_a}{dt} = -\frac{1}{m_a} \sum_b ({V_a}^2 + {V_b}^2) \frac{\rho_b p_a + \rho_a p_b}{\rho_a + \rho_b} \nabla_a W_{ab} \tag{3.5}$$

The artificial viscosity term can be added to the momentum equation to produce bulk and shear viscosity and also to stabilize the scheme as follows

$$\frac{d\mathbf{v}_a}{dt} = -\sum_b m_b \alpha h_{ab} c_{ab} \frac{\mathbf{v}_{ab} \cdot \mathbf{r}_{ab}}{\rho_{ab} \left(|r_{ab}|^2 + \epsilon\right)} \nabla_a W_{ab} \tag{3.6}$$

where $r_{ab} = |\mathbf{r}_a - \mathbf{r}_b|$. Also, h_{ab} and c_{ab} are the average smoothing length and average speed of sound respectively. The value of $\epsilon = 0.01$ is chosen to prevent the zero denominator and the value of α is kept constant for the wave generation computations [29]. The effective viscous coefficient can be obtained by the following relation.

$$\nu = \frac{1}{2(d+2)} \alpha h_{ab} c_{ab} \tag{3.7}$$

To reduce the jump in initial pressures and accelerations between the particles, the initial acceleration is damped for a period of t_{damp} by the following factor [52].

$$\zeta(t) = 0.5 \left[\sin((-0.5 + \frac{t}{t_{damp}})\pi) + 1\right], \quad t \leq t_{damp} \tag{3.8}$$

3.1.3 Solid Wall Boundary Condition

For the particles representing the wall, wavemaker, and AF, we used the generalized boundary condition that was formulated for the cases with moving boundaries [52]. In this method the fixed ghost particles represent the boundaries. The ghost particles are included in the continuity and momentum equations. Thus, when the fluid particles approach the ghost particles, their pressures increase thus, creating a high repellent force between them. This

prevents the fluid particles to penetrate into the boundaries.

The slip condition is satisfied by avoiding the viscous interaction of the fluid and ghost particles. For the no-slip condition, the velocity of the ghost particles is used for the viscous interactions. The velocity of the fluid is extrapolated to the ghost particle.

$$\tilde{v}_a = \frac{\sum_b v_b W_{ab}}{\sum_b W_{ab}} \tag{3.9}$$

Then, in the viscous interaction Eqn. (3.6), the velocity of

$$v_b = 2v_w - \tilde{v}_a \tag{3.10}$$

is assigned to the ghost particle where, v_w is the prescribed velocity of the wall particle. Fig. 3.1 shows the initial orientation of the wave tank wall, wavemaker, and fluid particles. The particle distancing shown is used for generating breaking waves at 11 m from the wavemaker in latter sections.

The pressure of a boundary particle surrounded by fluid particles is obtained from the following

$$p_w = \frac{\sum_f p_f W_{wf} + (\mathbf{g} - \mathbf{a}_w) \cdot \sum_f \rho_f \mathbf{r}_{wf} W_{wf}}{\sum_f W_{wf}} \tag{3.11}$$

where f and w represent fluid and boundary particles respectively. The acceleration of wall particles is included as $\mathbf{a}_w$. The density of wall particles is obtained from the pressure p_w as

$$\rho_w = \rho_0 \left(\frac{p_w - \chi}{p_0} + 1 \right)^{\frac{1}{\gamma}} \tag{3.12}$$

where ρ_0 and p_0 are reference density and pressure, defined in section 3.1.1.

3.1.4 Time-integration scheme

We used a velocity-Verlet scheme for stepping forward in time [52, 57].

$$\mathbf{v}_a^{n+\frac{1}{2}} = \mathbf{v}_a^n + \frac{\Delta t}{2} \left(\frac{d\mathbf{v}_a}{dt} \right)^n \tag{3.13}$$

$$\mathbf{r}_a^{n+\frac{1}{2}} = \mathbf{r}_a^n + \frac{\Delta t}{2} \mathbf{v}_a^{n+\frac{1}{2}} \tag{3.14}$$

$$\rho^{n+\frac{1}{2}} = \rho^n + \Delta t \frac{d\rho}{dt}^{n+\frac{1}{2}} \tag{3.15}$$

$$\mathbf{r}_a^{n+1} = \mathbf{r}_a^{n+\frac{1}{2}} + \frac{\Delta t}{2} \mathbf{v}_a^{n+\frac{1}{2}} \tag{3.16}$$

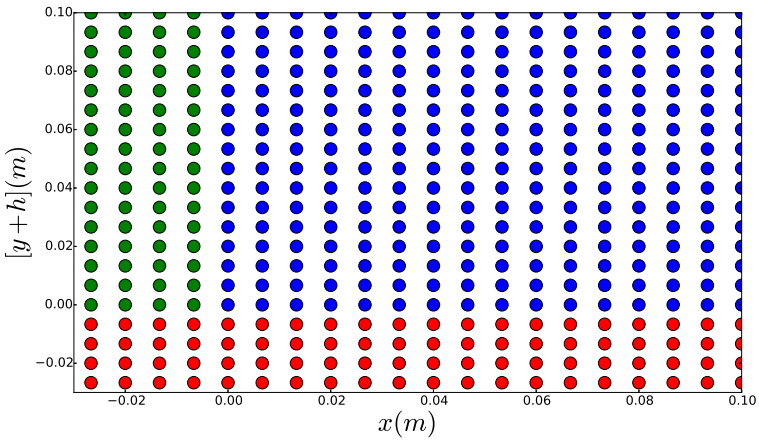

Figure 3.1: Initial particle placement in the computational wave tank. The circles shown with • represent fluid particles, • represent piston-type wavemaker (ghost particles), and • represent wave tank wall (ghost particles). This inter-particle distance was used to generate the breaking waves at 11 m from the wavemaker.

$$\mathbf{v}_a^{n+1} = \mathbf{v}_a^{n+\frac{1}{2}} + \frac{\Delta t}{2}\left(\frac{d\mathbf{v}_a}{dt}\right)^{n+1} \tag{3.17}$$

The minimum step size is based on the CFL-condition.

$$\begin{cases} \Delta t_{\text{sp}} \leq 0.25 \frac{h_0}{c_0 + |\mathbf{v}_{max}|} \\ \Delta t_{\text{vis}} \leq 0.125 \frac{h_0^2}{\nu} \\ \Delta t_{\text{fr}} \leq 0.25 \left(\frac{h_0}{|\mathbf{g}|}\right)^{0.5} \end{cases} \tag{3.18}$$

Then, the global time step Δt can be chosen as

$$\Delta t = \min(\Delta t_{\text{sp}},\ \Delta t_{\text{vis}},\ \Delta t_{\text{fr}}) \tag{3.19}$$

In Eqn. (3.18) the smoothing length $h_0 = h_{dx}\Delta x$ where $h_{dx} = 1.2$ was chosen for the simulations. The initial speed of sound was chosen as $c_0 = 10|\mathbf{v}_{max}|$, where $|\mathbf{v}_{max}| = (gh)^{0.5}$ and h is the water depth. In this thesis, simulations were based on the extension of PySPH frameworks [58].

3.1.5 Modifications

There are several corrections to the SPH scheme that make the numerical scheme more robust. One is a correction proposed to be applied to the equation of state Eqn. (3.3) [59].

$$\rho_a = \begin{cases} \rho_a & \rho_a \geq \rho_0 \\ \rho_0 & \rho_a < \rho_0 \end{cases} \tag{3.20}$$

The above equation is used to prevent the particles from sticking to the boundary. This equation imposes ρ_0 (the initial density value) to the boundary particles. Next, is the XSPH correction [60] that was used to advect particles. This condition imposes movement of a particle close to the average velocity of neighboring particles.

$$\frac{d\mathbf{r}_a}{dt} = \mathbf{v}_a - \epsilon_x \sum_b m_b \frac{\mathbf{v}_{ab}}{\rho_{ab}} W_{ab} \tag{3.21}$$

Finally, to update the smoothing length h_a we take on the following [61].

$$h_a = \frac{h_0}{\Delta x} \left(\frac{m_a}{\rho_a} \right)^{\frac{1}{d}} \tag{3.22}$$

This equation requires the recalculation of neighboring particles and should be used as the last equation in the numerical scheme.

3.2 Hydrostatic Pressure and Linear Waves

Achieving a stable linear hydrostatic pressure and the regular-wave generation are among the first steps to test the stability of the scheme before realizing our objective of studying the breaking wave environment. In order to generate linear waves, we briefly touch upon the linear potential-flow theory to relate the stroke length of the wavemaker to the amplitude of the generated linear harmonic waves. Based on the linear potential-flow theory with linearized boundary conditions, the general solution of potential for linear propagating and standing waves is as follows [42, 62].

$$\begin{aligned} \phi =& C_0 \cosh k_0(y+h) \sin(k_0 x - \omega t) \\ &+ \sum_{n=1}^{\infty} C_n e^{-k_n x} \cos\left[k_n(y+h)\right] \cos(\omega t) \end{aligned} \tag{3.23}$$

In Eqn. (3.23), the first part represents progressive waves and the second part decaying waves. The terms k_0 and k_n can be obtained from the well known dispersion relations.

$$\begin{aligned} \omega^2 &= g k_0 \tanh k_0 h, \quad \text{and} \\ \omega^2 &= -g k_n \tan k_n h, \quad n = 1, 2, .. \end{aligned} \tag{3.24}$$

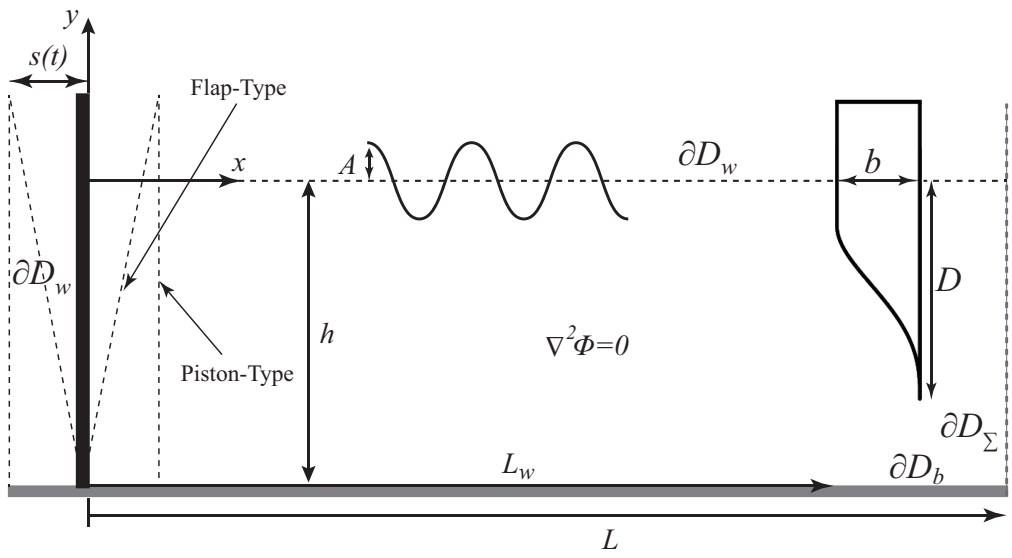

Figure 3.2: Schematics of the problem with the AF present.

By applying the proper boundary condition on the wavemaker and using orthogonality of the vertical functions of y the coefficients C_0 and C_n can be determined. Subsequently, the dynamic free-surface boundary condition enables the relation between the amplitude of the progressive waves and the potential

$$\begin{aligned}\eta(x,t) &= \frac{C_0\omega}{g}\cosh k_0 h\cos(k_0 x-\omega t)\\ &= A_f\cos(k_0 x-\omega t), \quad \text{for} \quad x\gg h\end{aligned} \tag{3.25}$$

where η and A_f are free-surface elevation and wave amplitude respectively. At this point we can relate the stroke length of the wavemaker to the wave amplitude. For flap-type wavemaker this relation can be obtain from the following equation.

$$\left(\frac{A_f}{S_0}\right)_{\text{flap}} = 4\left(\frac{\sinh k_0 h}{k_0 h}\right)\frac{k_0 h\sinh k_0 h-\cosh k_0 h+1}{\sinh 2k_0 h+2k_0 h} \tag{3.26}$$

Also, one can drive the expression for piston-type wavemaker stroke length to the wave amplitude as follows.

$$\left(\frac{A_f}{S_0}\right)_{\text{piston}} = \frac{2(\cosh 2k_0 h-1)}{\sinh 2k_0 h+2k_0 h} \tag{3.27}$$

Eqns. (3.26) and (3.27) can be used to estimate the wave elevation to the stroke length of the flap-type or piston-type wavemaker respectively.

In the WCSPH code, we created a computational wave tank (CWT) with a stabilized pressure field. The parameters used in the scheme were; $h = 1.53$ m, $L = 10$ m, $c_0 = 39$ m/s,

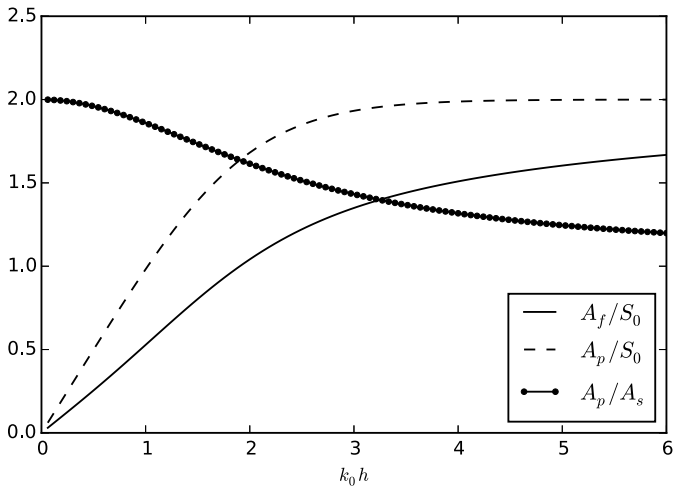

Figure 3.3: Ratio of wave amplitude generated by piston and flap-type wavemaker to stroke as a function of $k_0 h$

$\rho_0 = 1000$ kg/m^3, $\gamma = 7$, $\alpha = 0.05$, $h/\Delta x = 123$, and $dt = 6.58e-5$ s. At $t = 0$ the initial density of the particles were the reference density, therefore, their pressure was zero. Also, the initial accelerations of the particles were 0. Later, for $t > 0$ their accelerations smoothly increased by the $\zeta(t)$ (Eqn. (3.8)) to $-g$. Thus, the pressures of the wall particles gradually increased. As $t \to t_{damp}$, we observed a linear profile of the hydrostatic pressure of the fluid particles along the depth of the tank. Figure. 3.4a shows, the pressure field reaches a steady state for $t > t_{damp} = 1$ s. The linear profile of the pressure for the particles located at $x = L/2$ m along the wave tank depth (multi-processor implementation of WCSPH scheme) is shown in Fig. 3.4b. The theoretical hydrostatic pressure is also plotted for comparison. The linear profile of the pressure indicates the stability of the WCSPH scheme.

Next, the stroke length for the desired wave amplitude and period was obtained by using Eqns. (3.24) and (3.27). Then, the wavemaker was set in motion. The acceleration, velocity, and position of the wavemaker particles were the initial input to the WCSPH scheme. Also, the initial displacement of the wavemaker was multiplied by the following function

$$S = S_0 e^{-(t-6T)^2/2T^2} \quad \text{for} \quad t > 6T \tag{3.28}$$

where T is the wave period. This ensured the smooth start of the wavemaker for $t > 1$ and prevented any splashing. Wave profiles for two locations along the wave tank ($x = \lambda$ and $x = 2\lambda$) are shown in Fig. 3.4c. In this figure, the ramp-up, linear, and ramp-down sections of the wave are shown. At the end of the wave tank a beach with a tanh function was implemented to prevent excessive reflected waves from the end of the tank. The effectiveness of this scheme is verified by tuning the factor 1/6. The viscous interaction between the fluid and boundary particles dissipates the energy of the waves over the long length of the beach.

$$y_b = h \tanh \frac{x - L}{6} \quad \text{for} \quad x > L \tag{3.29}$$

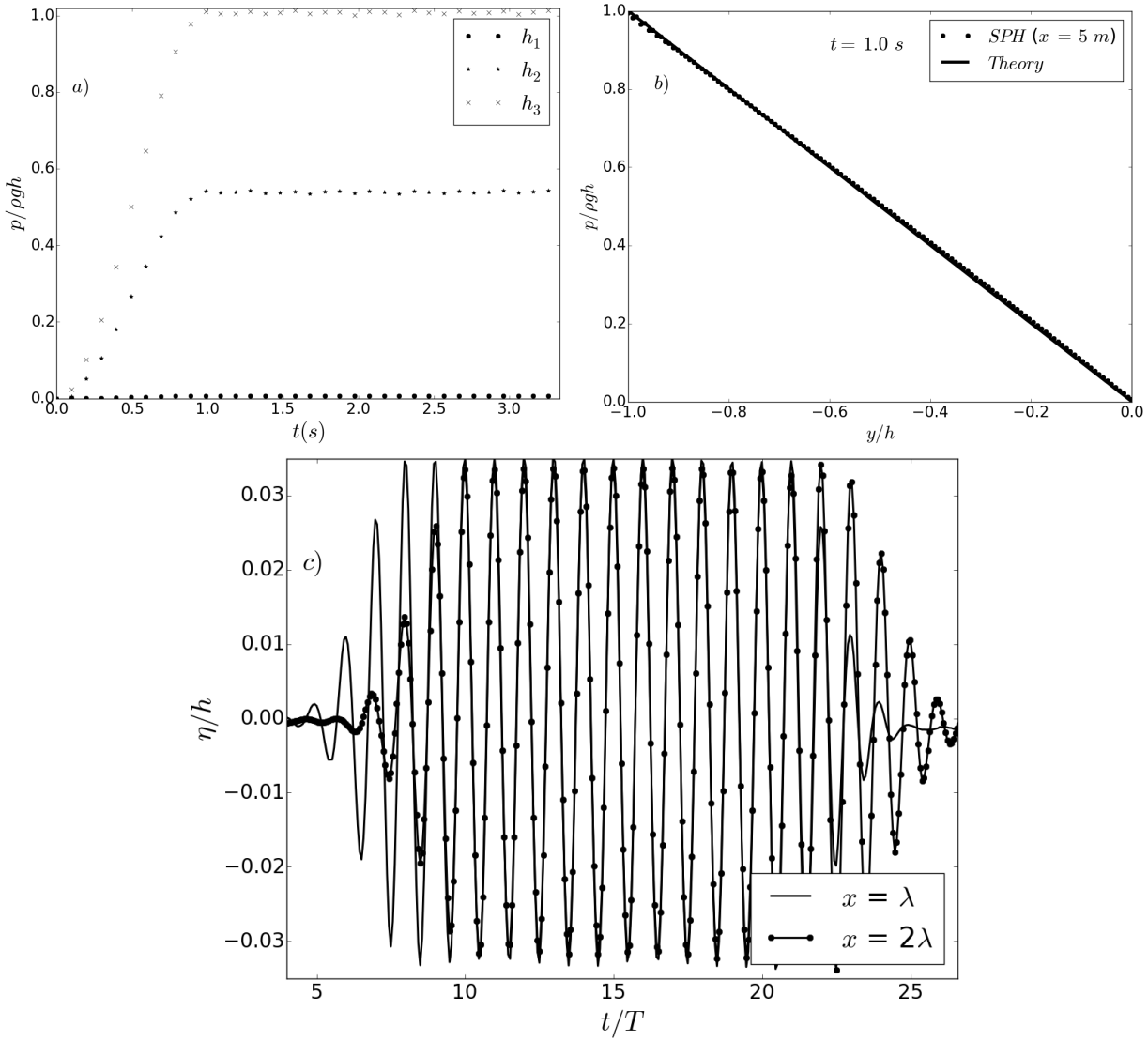

Figure 3.4: a) Pressure of the fluid particles located at $h_1 = 0$, $h_2 = -0.82$, and $h_3 = -1.53$ m, for $x = L/2$ m. b) Comparison of the theoretical hydrostatic pressure (ρgy) and the pressure of the fluid particles at $x = L/2$ m. c) Linear free surface profiles, $T = 1.5$ s.

The starting point of the beach was located at $x = L$. The total area of the beach with the length of 20 m was ~ 6.2 m^2. The area and number of particles needed to obtain the computational beach were equivalent to adding a 4 m damping layer (a technique to damp the velocity of the particles and to reduce the reflected waves).

3.3 Dam Break

In order to further test the scheme we analyzed the collapse of a water column under the gravity. This example have many aspects such as jet-flow impact and water re-entry that are useful in analyzing the plunging breaker impact force on TBW. The geometry of the problem is shown Fig. 3.5. We examined two cases of a square $b_d/h_d = 1$ and a rectangular $b_d/h_d = 2$ water columns. Then, we compared the results obtained from the computations to the ones reported in the literature [52, 63–65].

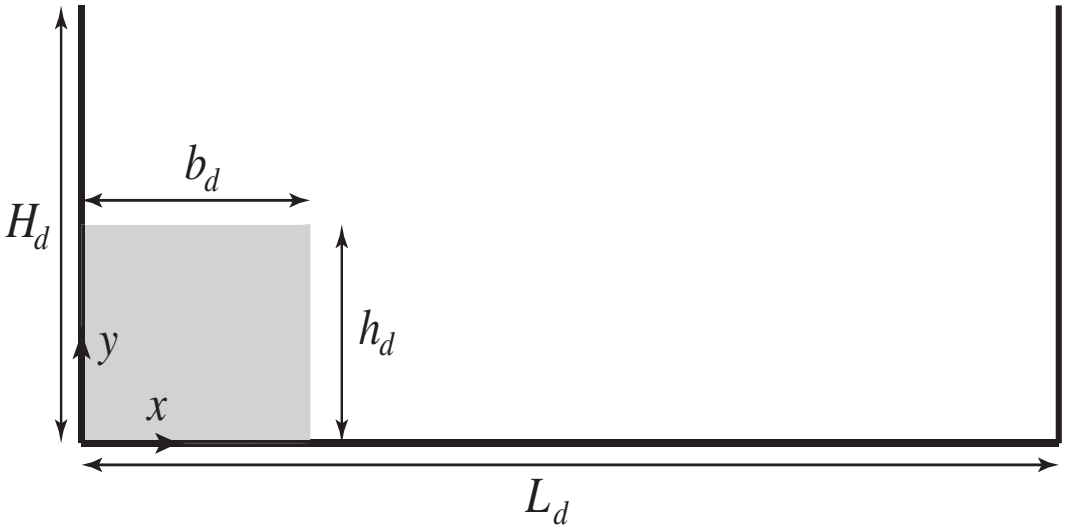

Figure 3.5: Schematics of the dam break.

3.3.1 Case of Square Water Column

The first example we consider was the collapse of a square water column $b_d/h_d = 1$ under the gravity. The length of $L_d/h_d = 5.366$ and hight of $H_d/h_d = 3$ were chosen for the tank geometry. In the scheme the viscous interaction between the fluid and wall particles were omitted to mimic the inviscid flow behavior. Different particle distancing Δx and factor α (Eqn. (3.6)) were adopted in the scheme to analyze how they affected the flow behavior. In this example Eqns. (3.21) and (3.22) were adopted in the numerical scheme. The following values were implemented in the computations; $h_{dx} = 1.2$, $c_0 = 10|\mathbf{v}_{max}|$, $|\mathbf{v}_{max}| = (gh_d)^{0.5}$, $g = 9.81\text{m/s}^2$, $\epsilon_x = 0.5$, $\alpha = 0.02,\ 0.1,\ 0.2,\ 0.4$, and $\Delta x/h_d = 0.02,\ 0.04$. Initially the density of the particles were chosen as the reference density $\rho/\rho_0 = 1$ thus, the initial pressure of the particles was zero. The Fig. 3.6a shows the water column front location at $y = 0$ vs time. The current computations ($\Delta x = 0.02$, $\alpha = 0.4$) is compared to the results reported in the

literature. The front location obtained from the current computations are in good agreement with SPH, BEM, and level set methods reported in the [52, 65]. The comparisons revealed the computations over predicted the water column's front location. This over prediction compared to experiment as discussed in [52,65], might be caused by surface roughness or the viscous effects between fluid and the bottom surface. Different values of particle distancing (Δx) and factor α were studied to analyze their affects on the movement of the water column front location and stability of the scheme. The Fig. 3.6b shows these comparisons. The location of the front of the water column is not altered with different values of Δx and α.

The top position of the water column at ($x = 0$) vs time is shown in Fig. 3.6c. The current SPH computations, the ones reported in [52], and experiments agree well.

3.3.2 Case of Rectangular Water Column

For the second example we changed the geometry of the water column by choosing the $b_d/h_d = 2$. Other dimensions of the problem stayed the same as section 3.3.1. In this example we looked at the release of the water particles under the effect of gravity. The comparison between the flow behavior and pressure field obtained from the current computations ($\Delta x/h_d = 0.005$ and $\alpha = 0.5$) and plots extracted from [52, 65] are shown in Fig. 3.7. The left column shows the current computations, the middle column result extracted from [52], and the right column from [65]. The current results of the free surface profile and cavity location are in good agreement with both cited examples. Also, the pressure field is in good agreement with [52]. The pressure field observed is different from the linear hydrostatic pressure profile reported in [65]. The weakly compressible nature of the scheme creates a dynamic pressure fluctuations. This is caused by weakly damped sound waves as a results of small viscous effects. For analyzing the effects of different α values on the pressure fluctuations, we incorporated $\alpha = 0.5,\ 0.4,\ 0.2$ in the computations. The results presented in Fig. 3.8. As the flow impacts the right tank wall, it creates a pressure shock. For the larger α value we observe less fluctuations in the pressure filed. Additionally, we hold the water particles by a barrier so a stable hydrostatic pressure of the fluid was achieved. Then, we removed the barrier. Less fluctuation of the pressure after the impact of the water jet to the right tank wall was observed.

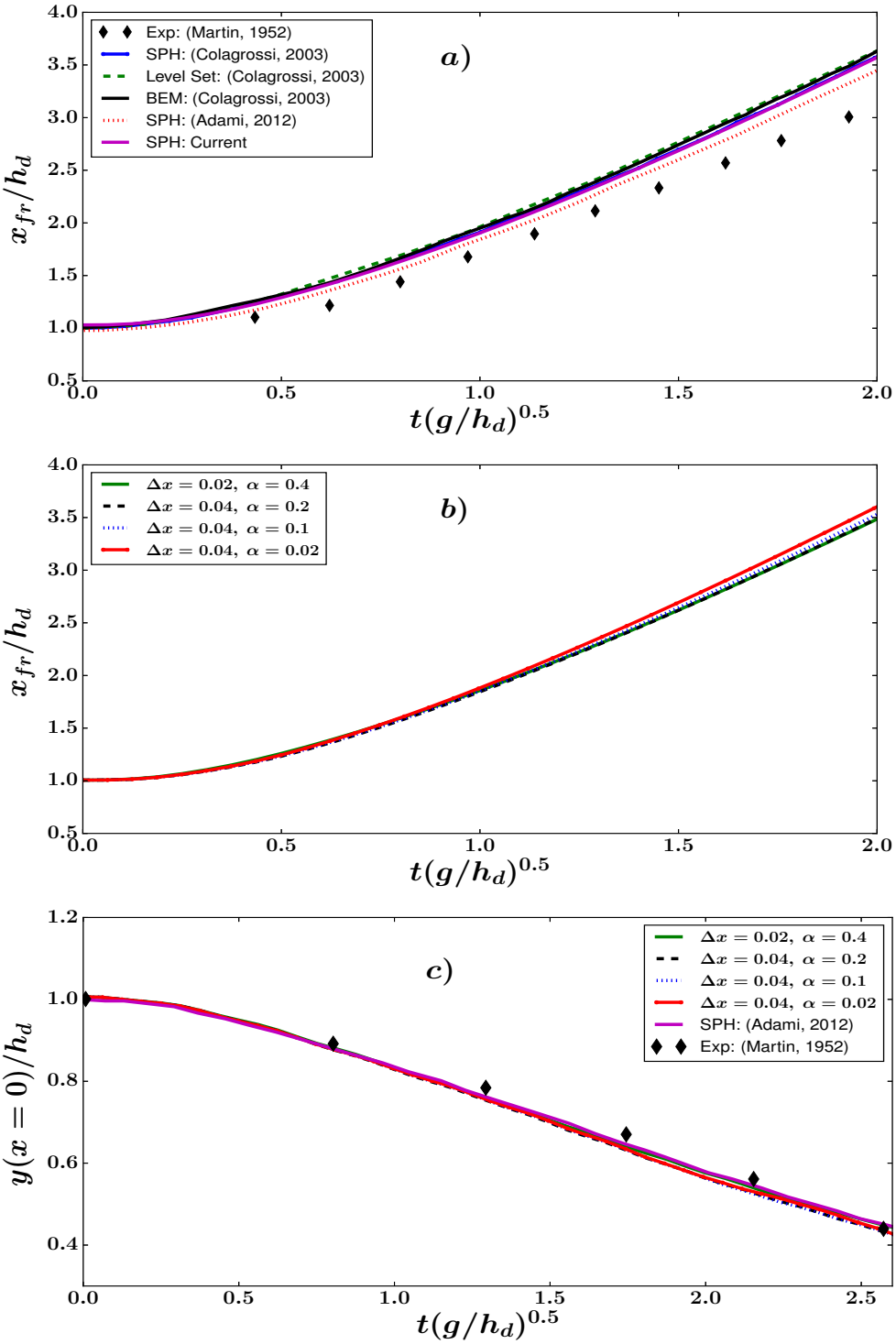

Figure 3.6: Comparison of front $x|_{y=0}$ and top $y|_{x=0}$ of the water column vs time.

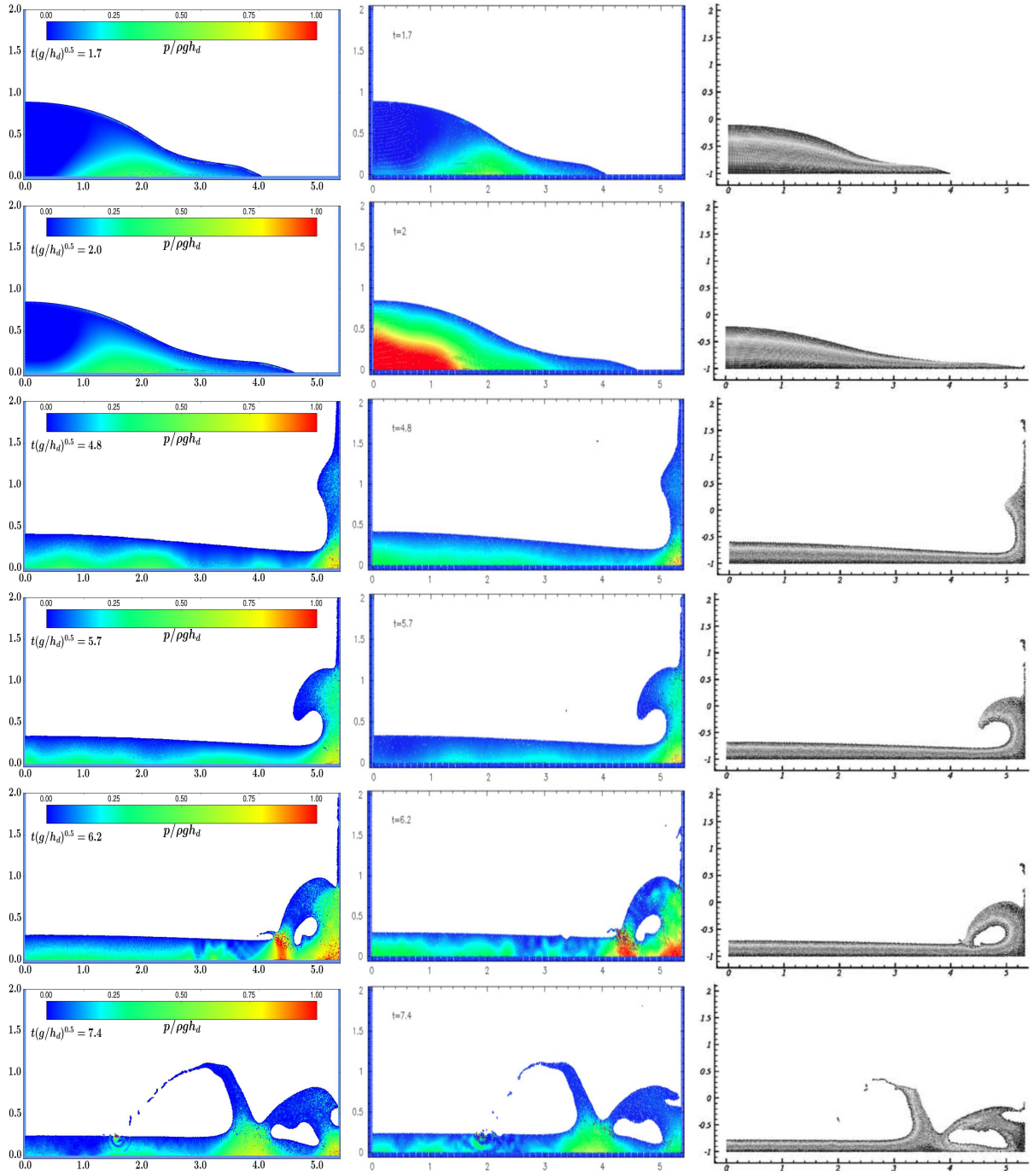

Figure 3.7: Dam break at different time windows, right column is the current computations, the middle column is extracted from [52] and the right column from [65].

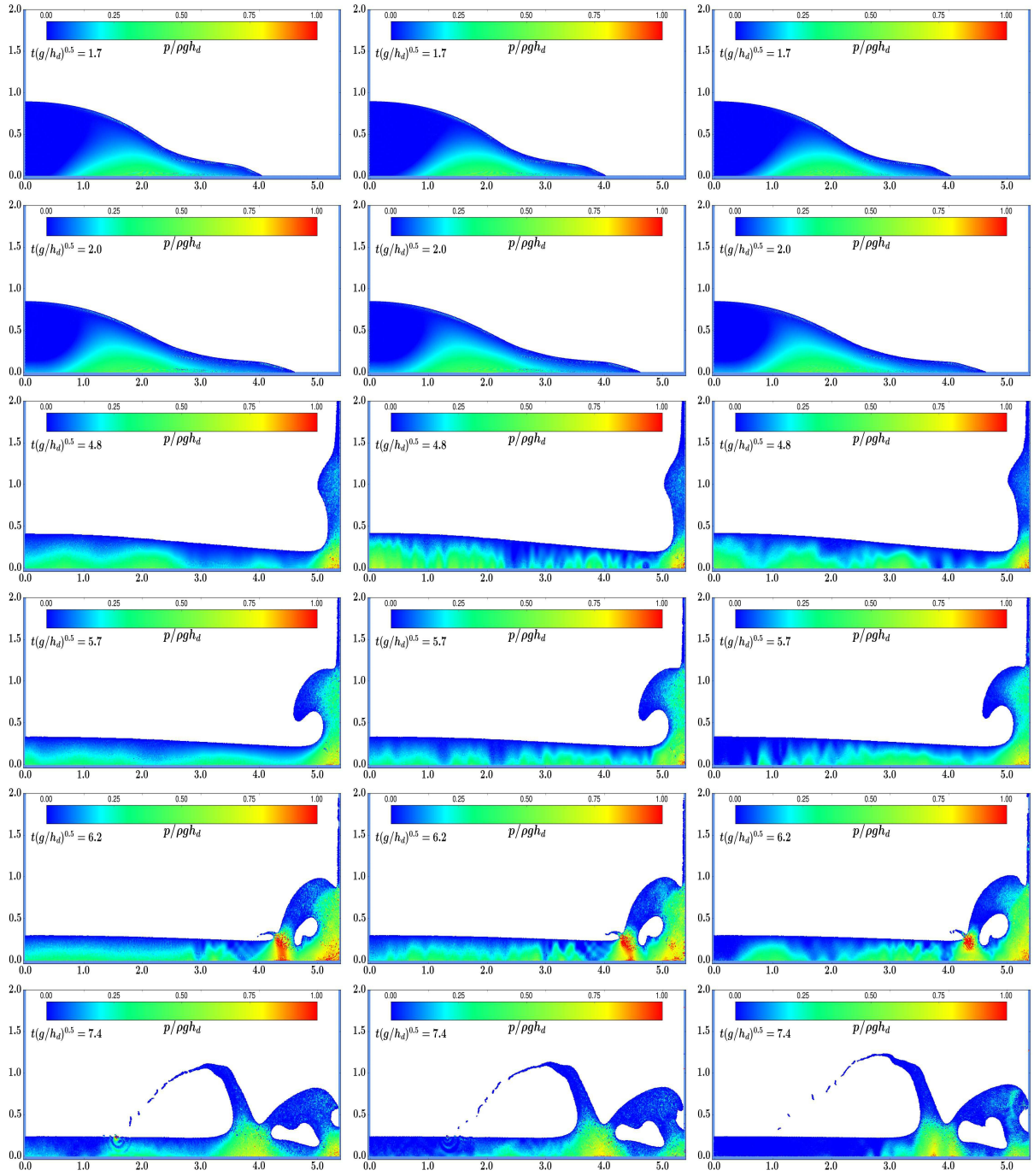

Figure 3.8: Dam break different α values. From left to right $\alpha = 0.5,\ 0.4,\ 0.2$.

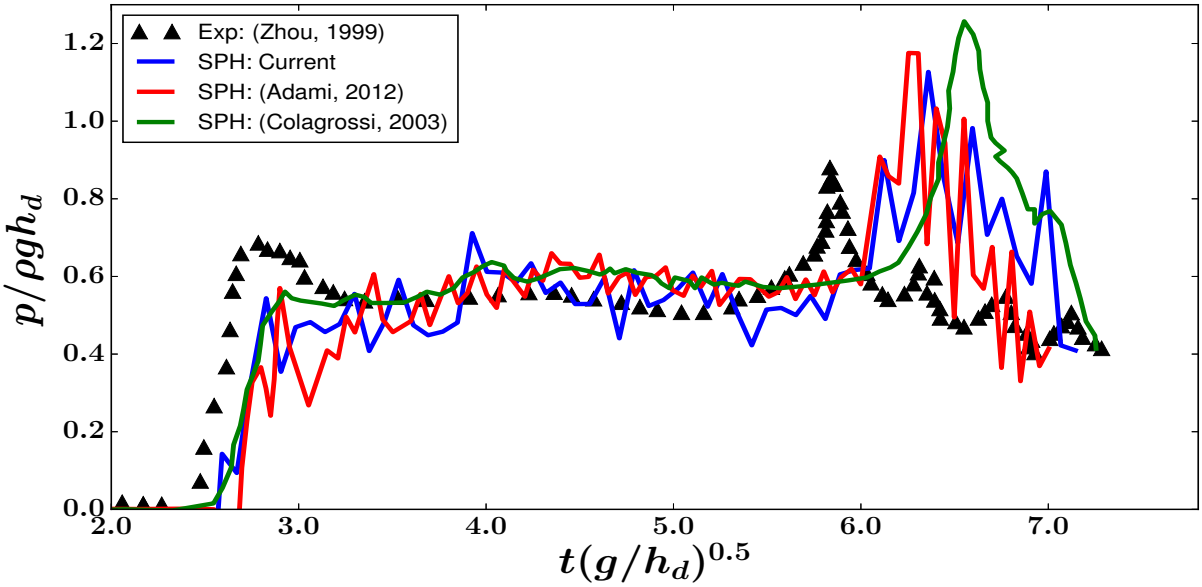

Figure 3.9: Pressure on the right side wall at $y/h_d = 0.2$.

Finally, we compared the pressure on the right wall at $y/h_d = 0.2$ that was obtained by Eqn. 3.11. The comparison between the pressure obtained from the current computations ($\Delta x = 0.005$ and $\alpha = 0.5$) and the ones reported in [52, 64, 65] is shown in Fig. 3.9. As expected and also reported by [52], we observed high frequency oscillation of the pressure but the main pressure profile was captured. In the latter sections, we allowed fluid to reach a hydrostatic stability before initiating the wavemaker. This reduced the pressure fluctuations in the flow and boundaries.

3.4 Breaking Waves

In order to achieve deep-water breaking waves in a tank, an input spectrum for the wavemaker is needed to generate waves that group together at a desired time and location. When several waves with correct phases, amplitudes, and frequencies group in a location, a high amplitude crest is produced that results in a plunging breaker. In a study [66], the relation between target wave profile before breaking to the input spectrum of the wavemaker is examined. This analysis is based on steady-state waves. Therefore, if at a specific location and time, the phase angles of the waves are known, all other phase angles can be found at other locations. Let us look at the collocation of M waves around a fundamental wave number, k_c, and

frequency, ω_c.

$$\begin{aligned}\eta(x,t) &= \sum_{i=1}^{M} A_i \cos(k_i x - \omega_i t + \theta_i) \\ &= \sum_{i=1}^{M} A_i \cos(k_c x - \omega_c t + \Delta\theta_i)\end{aligned} \tag{3.30}$$

The $\Delta\theta_i$ is the relative phase between the fundamental and i^{th} wave as

$$\Delta\theta_i = (k_i - k_c)x - (\omega_i - \omega_c)t + (\theta_i - \theta_c) \tag{3.31}$$

where θ_c represents the fundamental phase angle at $(x,t) = (0,0)$. A displacement of the piston-type wavemaker for generating deep-water plunging breakers can be developed by a summation of M waves [67].

$$s_p(t) = \sum_{i=1}^{M} x_i \sin(\omega_i t - \theta_i) \tag{3.32}$$

The input displacement for the piston-type wavemaker to generate plunging breakers at the location and time of (x^*, t^*), where $\Delta\theta_i$ is given, can be obtained from Eqns. (3.32), (3.27), and (3.31). If we arrange 52 waves with the fundamental wave frequency of $\omega_c(h/g)^{0.5} = 1.54$ to obtain a high crest wave at the location and time of $(x^*/h, t^*(g/h)^{0.5}) = (7.44, 45.38)$, we obtain the time history of the piston-type wavemaker displacement shown in Fig. 3.10a. In Table D.1 the 52 coefficients of x_i, ω_i, and θ_i are given to obtain the piston-type wavemaker displacement.

Next, the displacements (Fig. 3.10a) was implemented in the CWT's piston-type wavemaker. We constructed the CWT with the dimensions of $L = 13$ m and $h = 1.53$ m. In the WCSPH scheme the following values were adopted; $h/\Delta x = 226$, $c_0 = 39$ m/s, $\gamma = 7$, $dt = 3.56e-5$ s, $\epsilon_x = 0.5$, and $\alpha = 0.05$. The wavemaker's displacement started at $t = 2$ s to allow the inter-particle forces to equalize. Figs. 3.11b-3.11e show the comparison between the free surface profiles obtained from the linear potential-flow theory and computations. As we move forward in time the non-linearity of the surface profile and differences between the linear theory and computations become apparent. The actual location, where the wave resulted from the grouping of 52 waves reached its steepest peak before breaking, was observed (in CWT) at $(x/h, t(g/h)^{0.5}) = (7.24, 40.41)$. Water re-entry took place at $(x/h, t(g/h)^{0.5}) = (7.62, 40.99)$. The linear potential-flow theory was shown to be a fast way to predict the approximate location and time of the steepest crest wave.

Afterward, the displacement which was obtained by the linear potential-flow and confirmed by the computations, was adjusted to be used in the physical wave tank's (PWT) flap-type wavemaker. We obtained the new profile by changing the x_i coefficients (in Table D.1) according to Eqn. (3.26) and physical characteristics of the wavemaker. The breaking wave that was obtained in the PWT is shown in the left column of Fig. 3.13. The experimental and computational free-surface profiles for different locations along the wave tanks are shown

in the left column of Fig. 3.12. As shown in this figure, there is a satisfactory agreement between the experiment and computation.

The location of the PWT's visual window starts at approximately 20 m from the wave-

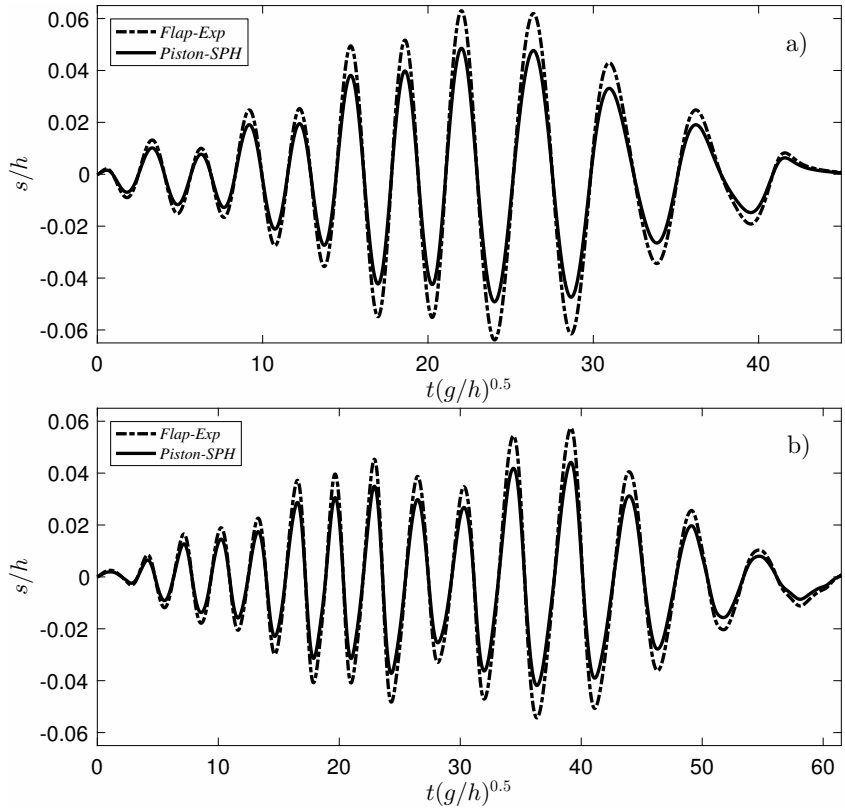

Figure 3.10: Displacement profiles of the piston-type and flap-type wavemakers to achieve deep-water plunging breakers.

maker. The ease of visualization required that the breaking waves be transferred to that section. For achieving this purpose we could adopt different techniques such as frequency-scaling. In this method the Froude scaling is used to change the fundamental wave components by a factor r. We can apply the geometric similarities to obtain the new components. For instance; $\hat{x}^* = x^* r^{-2}$, $\hat{\omega}_c = \omega_c r$, $\hat{k}_c = k_c r^2$, $\hat{t}^* = t^* r^{-1}$, etc., where the *hat* variables represent the new scaled components. The frequency-scaling method (for $r < 1$) results in a displacement profile that induces stress on the wavemaker as it requires a very large stroke of the flapper.

The "Packet Translation" is an another method to transfer the plunging breakers while maintaining the same ω_i. By defining a new θ_i in Eqn. (3.30) we can arrange the components of the wave to converge in a new location and time $(\overline{x}^*, \overline{t}^*)$.

$$\overline{x}^* = x^* + X \qquad \text{and} \qquad \overline{t}^* = t^* + \tau \tag{3.33}$$

X and τ are the linear transformations in space and time. They are related by the group velocity of the fundamental wave as $\tau = X/c_g$ where $c_g = 0.5\omega_c/k_c$. By substituting the newly defined variables ($\overline{x}^*$, $\overline{t}^*$) into Eqn. (3.30) we obtain the new equation for the new wave profile.

$$\begin{aligned}\eta(\overline{x}^*, \overline{t}^*) &= \sum_{i=1}^{M} A_i \cos(k_i \overline{x}^* - \omega \overline{t}^* + \overline{\theta}_i) \\ &= \sum_{i=1}^{M} A_i \cos\{k_i x^* - \omega_i t^* + \theta_i \\ &\quad + [\overline{\theta}_i - \theta_i + k_i \Delta x - \omega_i \Delta t]\}\end{aligned} \tag{3.34}$$

For obtaining the identical wave profile as specified in Eqn. (3.30), the bracketed term in Eqn. (3.34) vanishes and θ_i can be found.

$$\overline{\theta}_i = \theta_i - k_i \Delta x + \omega_i \Delta t \tag{3.35}$$

The new packet-translated piston-type wavemaker displacement profile with $\omega_c(h/g)^{0.5} = 1.54$ is shown in Fig. 3.10b. The location, and time of the targeted free-surface profile is shown in Fig. 3.11f. The predicted free-surface profile by the linear potential-flow theory was observed at $(x^*/h, t^*(g/h)^{0.5}) = (13.80, 71.66)$. The 72 components to obtain the new wavemaker profile are given in Table D.2.

The new displacement profile was implemented in the CWT's piston-type wavemaker. In the WCSPH scheme we espoused the same parameters as for the previous profile except, the length of the wave tank was increased to $L = 23$ m. A delay of $t = 1.8$ s was chosen before the initiation of the wavemaker's motion. Comparisons between the linear potential-flow theory and WCSPH predictions of the surface profiles for different time instances are shown in Figs. 3.11g-3.11j. The free-surface profile with the highest peak was observed at $(x/h, t(g/h)^{0.5}) = (13.72, 66.57)$ in CWT. Also, the wave re-enters the water surface at $(x/h, t(g/h)^{0.5}) = (14.10, 67.21)$.

Next, the displacement profile was adjusted (shown in Fig. 3.10b) and used for the PWT's flap-type wavemaker. The new breaking wave at the location of PWT's visual window is shown in Fig. 3.13 right column. The free-surface profiles at different locations of the CWT and PWT are shown in the right column of Fig. 3.12. WCSPH computations predicted the free surface profile well. All the results were shifted in time to account for the delayed start of the wavemakers displacement.

The two wave profiles obtained from the wavemaker displacement profiles shown in Figs. 3.10a and 3.10b are compared in Figs. 3.14a-b and 3.14c-d. The similarities in the free surface profiles, the velocity, and pressure fields are clearly presented. Also, the linearity of the pressure field in both wave profiles can be seen.

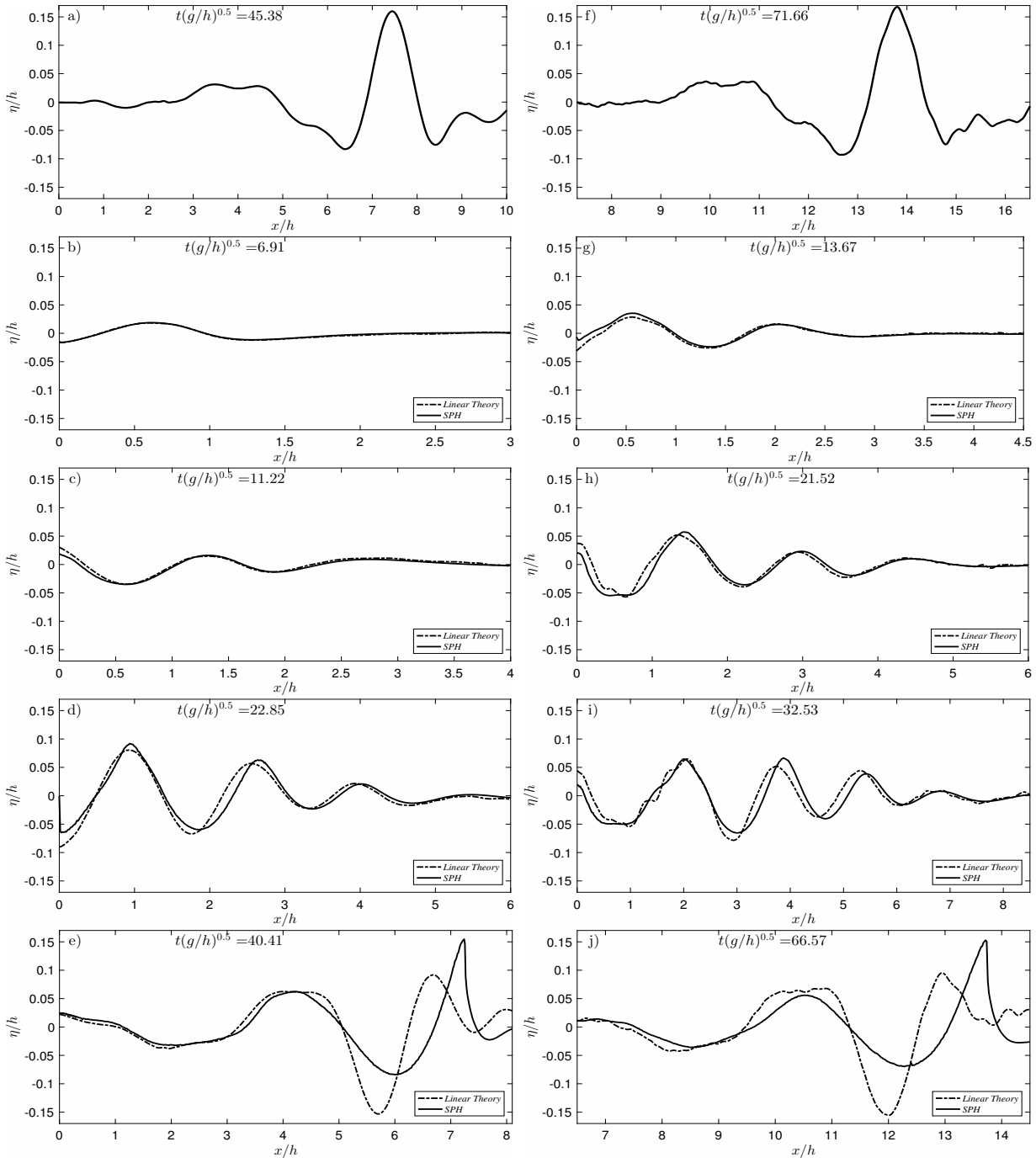

Figure 3.11: The linear potential-flow vs WCSPH computations, left column plots are free surface profiles results obtained from wavemaker displacement profile shown in Fig. 3.10a and the right column plots from Fig. 3.10b. Plots a) and f) are the targeted free-surface profiles obtained by potential-flow theory.

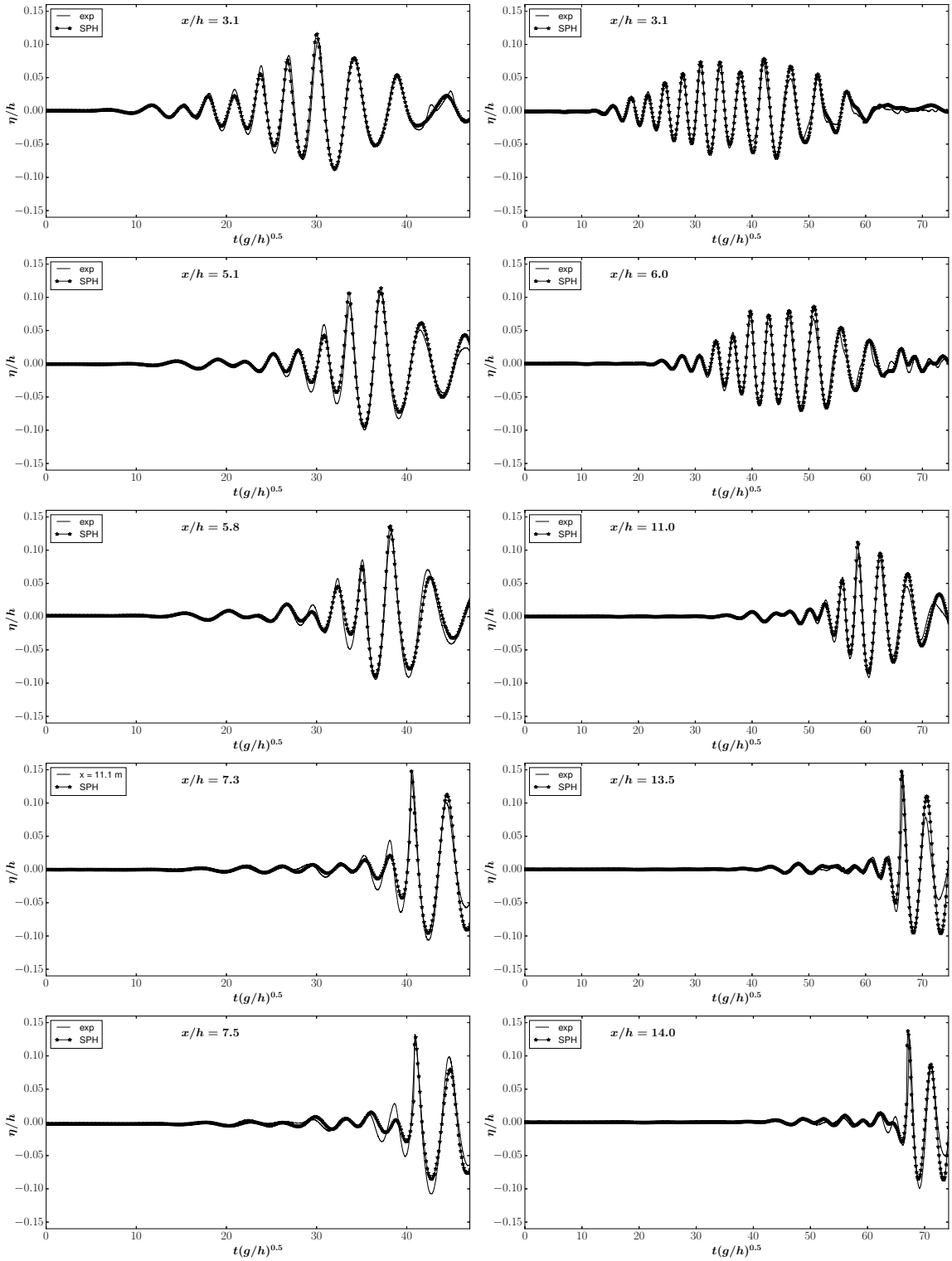

Figure 3.12: Comparison between experimental and computational wave elevations for different locations along the wave tanks. Left column obtained from Fig. 3.10a and the right column from Fig. 3.10b.

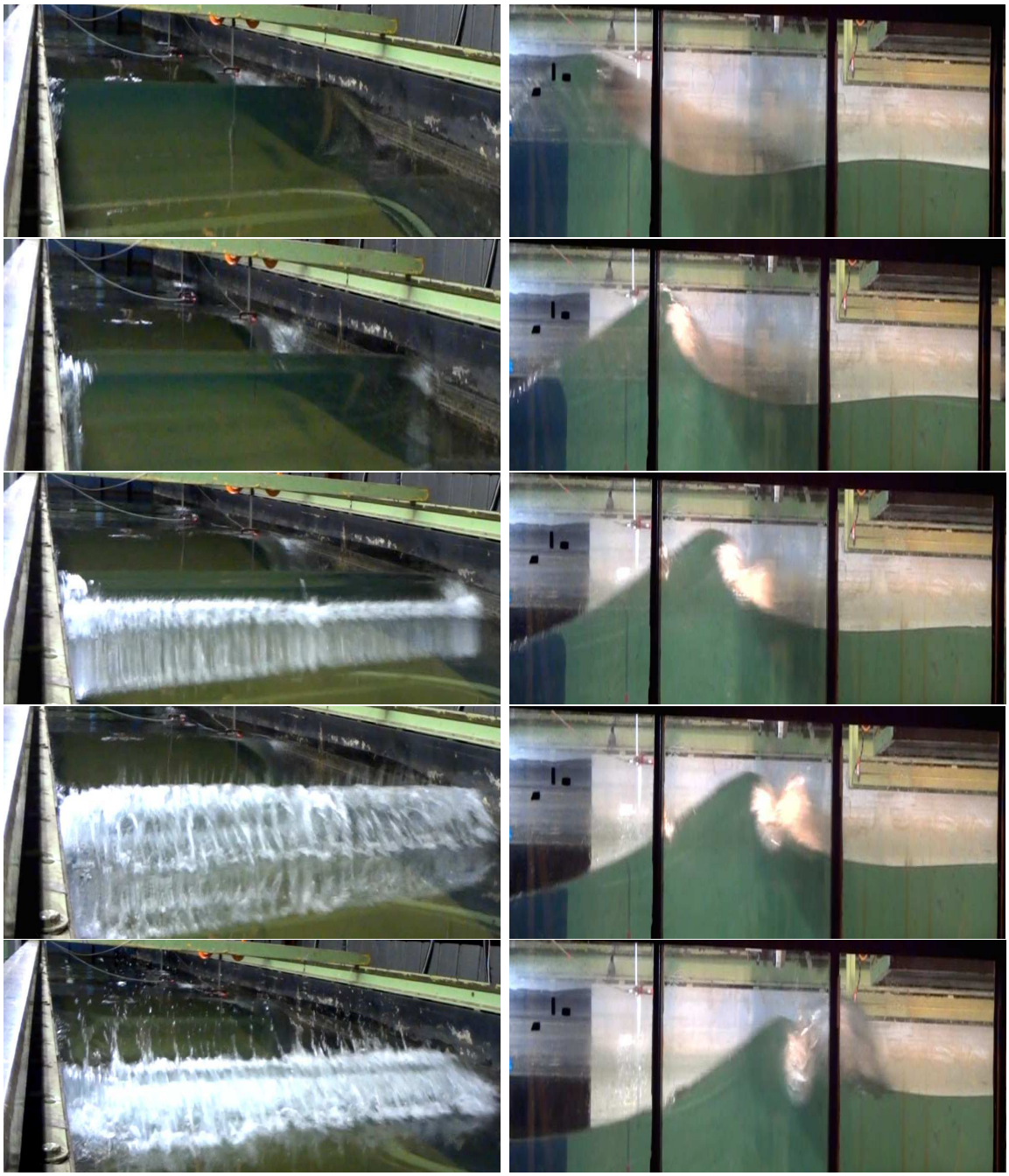

Figure 3.13: Breaking waves in PWT. Left column obtained from Fig. 3.10a and the right column from Fig. 3.10b.

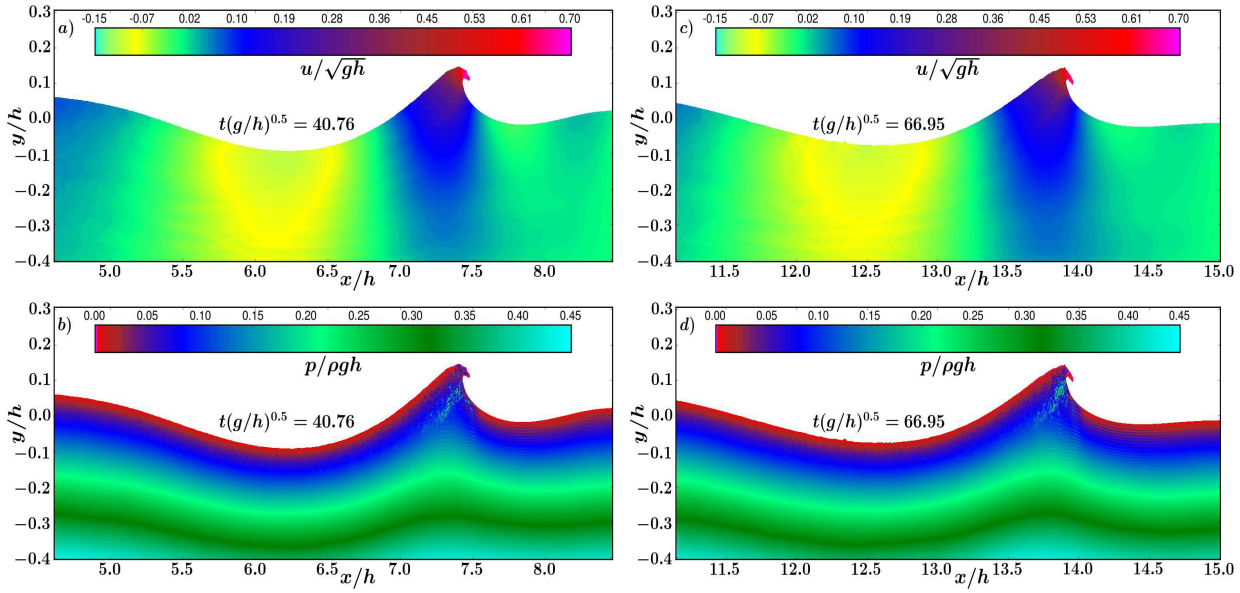

Figure 3.14: Pressure and velocity fields of the plunging breakers. Left column obtained by implementation of wavemaker displacement profile shown in Fig. 3.10a and the right column from Fig. 3.10b into WCSPH scheme.

3.5 Breaking Waves and TBW

3.5.1 Experiments

Achieving similar plunging breakers at the two set locations in the CWT and PWT enabled us to chose the PWT's window location for conducting the experimental measurement of the force and visually inspect the flow. The physical model of the AF was positioned in the PWT further downstream from the water-entry location of the breaking waves to analyze a jet-like-flow impact. The AF model has an approximate beam of $b = 0.22$ m, width of $w = 2.33$ m, and height of $H = 1.03$ m. The width of the AF span across the wave tank and leaves a very small gap between each side of the AF and wave tank walls. Water ballast was used to acquire different drafts of the AF. For the operational condition in linear harmonic waves the draft of the AF model was chosen to be 0.8 m. This draft ensured that the resonance period of the AF was in the linear wave-making range of the wavemaker. Thus, the vertical force on the AF was measured with this draft in the presence of the plunging breakers (see Fig. 3.17). The vertical displacement of the AF is fixed by the means of force blocks for the force measurements. The experiments repeated several times in order to check the repeatability of the results.

Next, the AF was fully submerged ($D = 1.03$ m) as shown in Figs. 3.15 and 3.18. This draft is the maximum allowable draft of the AF model as the electrical components of the PTO are attached to the top of the AF above water line. This PTO location was chosen

for the ease of operation, maintenance, electrical power transfer to girds, and to prevent water damage to the electrical parts. The vertical force was measured in the presence of the breaking waves.

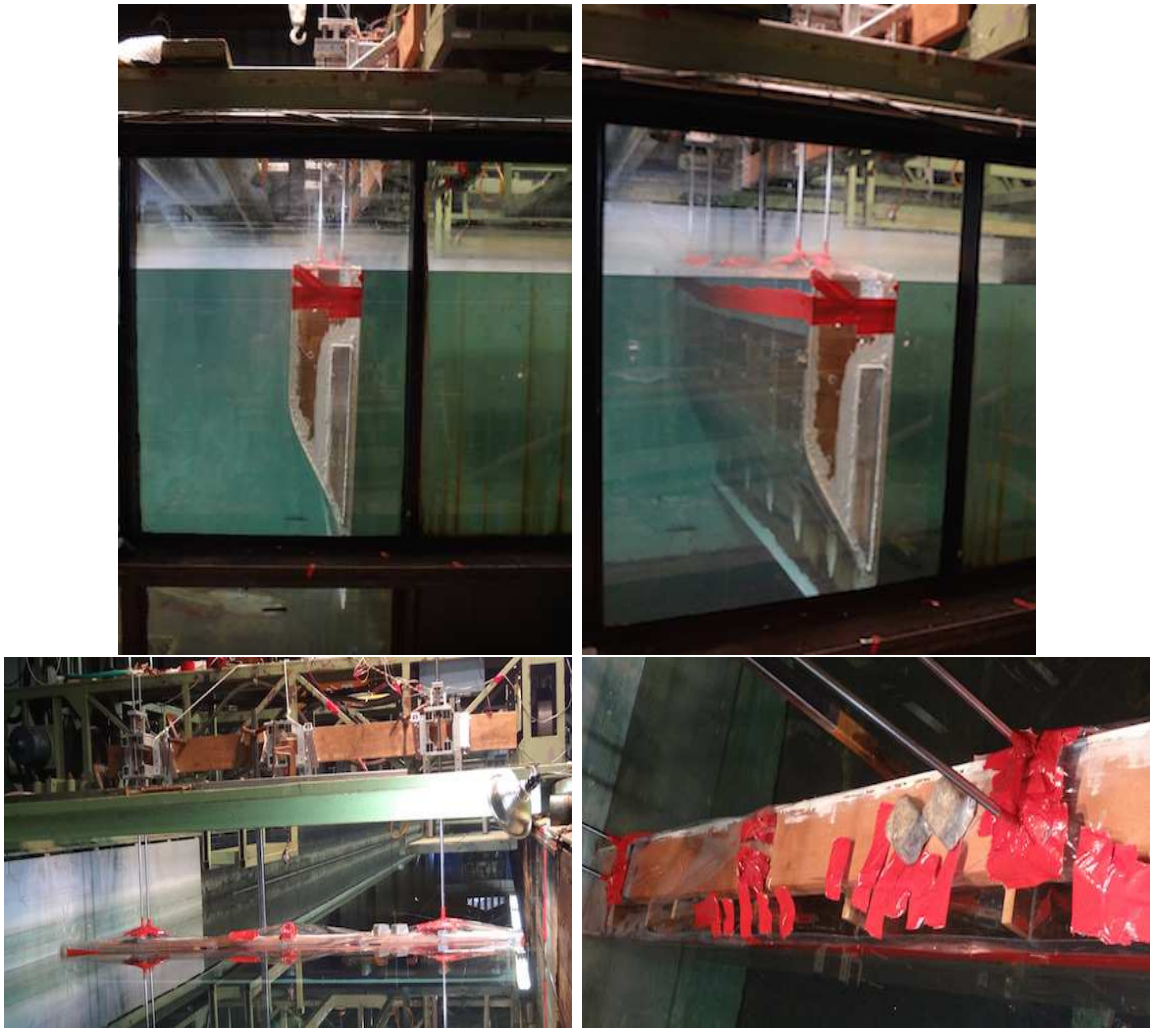

Figure 3.15: Experimental setup of fully submerged AF ($D = 1.03$ m).

3.5.2 Computations

Lowering the computational cost demanded shifting the plunging breakers closer to the wavemaker. As we decrease the length of the wave tank we lower the number of particles required in the computations. In Sec. 3.4 it was confirmed that the plunging breakers, resulted from the two displacement profiles shown in Fig. 3.10, were satisfactorily similar.

Also, the experimental and computational wave profiles matched quite well as shown in Fig. 3.12. The computational model of the AF was positioned at $L = 12$ m in the CWT. This location is further downstream from the breaking waves water entry point (as it was done in the experiments). We adopted a piston-type wavemaker in the CWT to lower the computational cost. The displacement of the wavemaker is shown in Fig. 3.10a. Forces on the AF, with the 0.8 m and fully submerged ($D = 1.03$ m) drafts, in the presence of the plunging breakers were measured. In the computations the pressure on the AF was obtained from Eqn. (3.11). The desired hydrostatic pressure was achieved on the AF about 1 s after the simulations started as shown in Fig. 3.16. The wavemaker was set to motion at $t = 2$ s. In the WCSPH scheme the same parameters were used as mentioned in Section. 3.4. The particle spacing of $h/\Delta x = 230$ was used in the computations.

The side by side comparisons of experiments and computations for the case of the AF (0.8 m draft) encountering the plunging breakers, at different time windows, are shown in Fig. 3.17. These comparisons indicated the largest pressure that the AF experienced upon the breaking waves impact was at the area above the water line facing the waves. The initial wave impact resulted in an impulsive repellent vertical ($F_y > 0$) and horizontal ($F_x > 0$) forces. Later in time, when the trough of the plunging breakers reached the AF, the front water level declined. This caused pressure build up on the leeward side close to the tip of the AF. Therefore, there was a high flow velocity under the AF tip, from the leeward side to the front side. This caused the AF to endure a secondary wide-band horizontal suction force ($F_x < 0$) and vertical downward force ($F_y < 0$).

As shown in Fig. 3.18 submerging the AF caused the waves to pass over it. This resulted in reducing the initial F_x peak that was present in the 0.8 m draft by 50%. On the other hand, a less significant change in the second F_x peak was observed. Similar behaviors were observed in the F_y. The comparison between the F_y obtained by experiment and computations is shown in Fig. 3.20c.

3.5.3 Pressure-Relief Channels (PRCs)

As discussed in the previous section, submerging the AF led to a reduction of the forces at the moment of the initial jet-flow impact. On the other hand, a negligible change in the secondary peak values of the F_x or F_y were observed. It is more practical and efficient to seek a solution to increase the survivability of TBW while maintaining its operational draft. Thus, in the computations, the areas of the AF geometry that experienced maximum pressure from the fluid were identified. These areas were; the portion of the AF geometry above the water line facing the waves and also the area leeward of the AF close to the tip. After, with considering the structural integrity of the AF, two places were singled out and removed from the geometry of the AF (in computations). These removed areas we named pressure-relief channels (PRCs).

The x-component of the fluid velocity as well as the pressure and the forces on the AF, with one and two PRCs, that were obtained by the computations are displayed in Fig. 3.19. The color-bars are shown in Fig. 3.17. As shown, the bottom PRC is effective in reducing

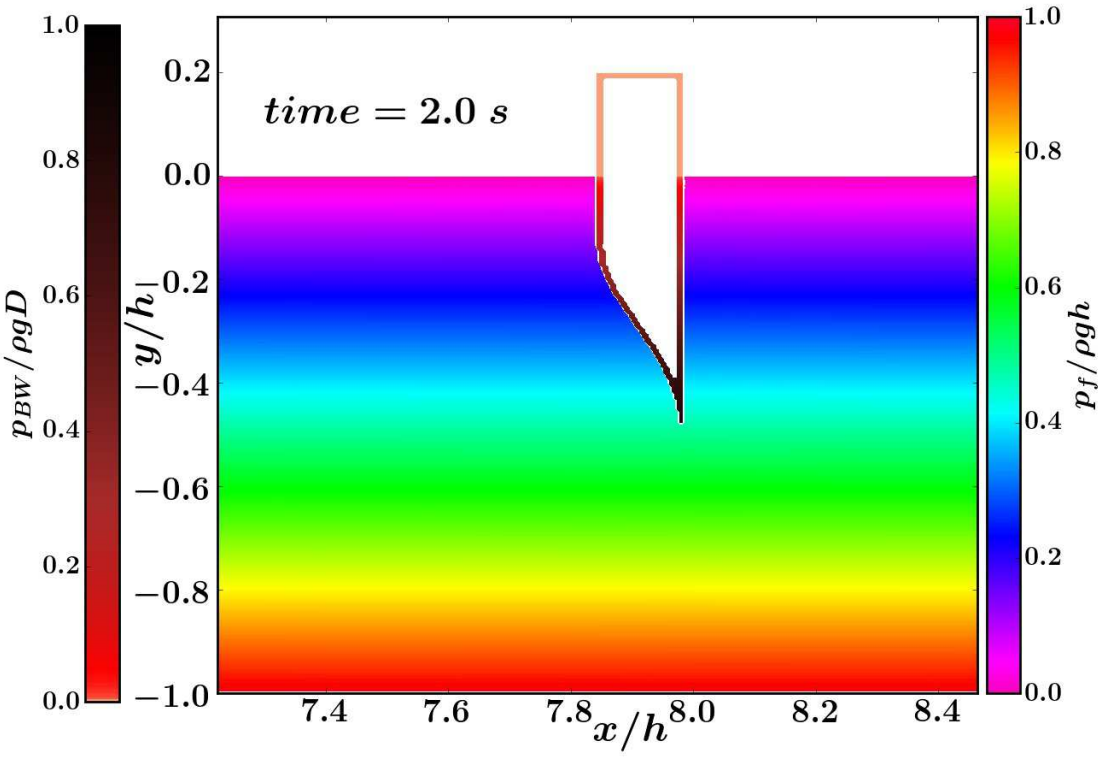

Figure 3.16: The fluid pressure and extrapolated pressure on the AF boundary after $t = 2$ s from the start of simulations.

the flow velocity near the tip of the AF, hence reducing the pressure build up in that region. The implementation of both bottom and top PRCs dramatically decreased the pressure on the surface of the AF by allowing the fluid flow through it.

The comparison between the four cases of experimental measurement of the vertical force on the AF model, computational measurement of the vertical force on the AF with zero, one, and two PRCs are presented in Fig. 3.20a ($D = 0.8$ m). The experimental and computational values of the F_y agree well. Placing the bottom PRC on the 0.8 m draft AF reduced the F_x by approximately 24% in the initial peak and by 50% in the secondary peak when compared to the case of the AF with zero PRC. On the contrary, this had an insignificant effect on reducing the peak values of the F_y. In addition to the bottom PRC a second one was implemented on the AF above the water surface where it experienced high pressure upon the initial impact. Placements of the top and bottom PRCs caused much reduction of both the F_x and F_y peak values as shown in Figs. 3.20a and 3.20c. The values of the repellent and suction portions of the F_y were reduced by more than 50%. More importantly, the repellent part of the F_x was reduced by 80% and the suction part of the F_x was reduced by more than 50%. The vertical force (F_y) was an order of magnitude smaller than the horizontal force (F_x) for the 0.8 m draft AF. Thus, reducing the F_x is the deciding factor in the survivability

of TBW. Therefore, we demonstrated that implementing the PRCs, while fixing the motion of the AF, is an effective solution for the survivability of TBW and similar structures.

3.6 Proposed Implementation Strategy for PRCs

Figure. 3.21 depicts a set of three drawings to demonstrate the operational and survivability conditions of TBW. For the operational condition the AF has a smooth surface for maximum performance of the system as shown in Fig. 3.21a. The side view of the AF with the PTO location and its components are specified in Fig. 3.21b. As shown, the PTO is located above the water line and inside a cover to prevent water damage to the electronics. In addition, a proposed bottom mounting structure for TBW is illustrated. The mounting structure provides stability to the AF and PTO while restricting the motion of the AF to heave only.

For the survivability condition, having in mind the integrity of the AF structure, several locations are chosen for the PRCs as shown in Fig. 3.21c. After the installation of TBW units at sea, wave sensor buoys are positioned in front of them to measure the amplitude and frequency of the incident waves. The PRCs are closed during the operational condition. They open when the sensors detect large extreme waves. The PRCs located near the tip of the AF are filled with water in the operational mode. They are located below the calm water line and do not have free-surfaces; therefore, they act as solid blocks. Thus, they do not alter the performance of TBW. On the other hand, they reduce the need for additional ballast. The top PRCs are empty in operational mode and when opened in extreme seas, water rushes out and they stay empty as demonstrated in Fig. 3.19. Several of TBW units (Fig. 3.21) can be positioned near shore to protect the harbor at the same time they provide electricity to the local community.

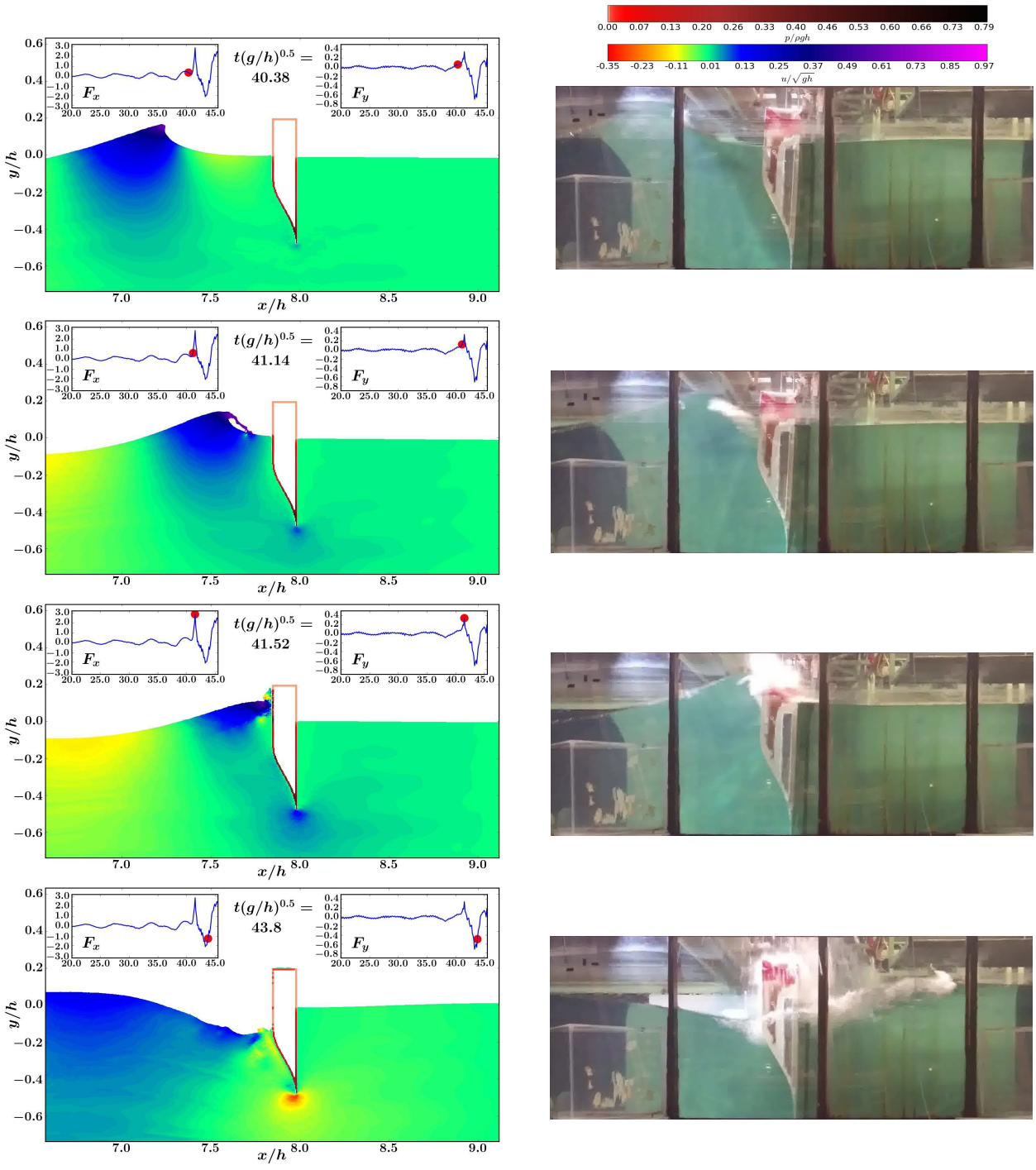

Figure 3.17: The AF ($D = 0.8$ m) encountering a plunging breaker, WCSPH computations on the left and experiments on the right. The color-bars indicate the pressure on the AF and x-component of fluid particle velocity.

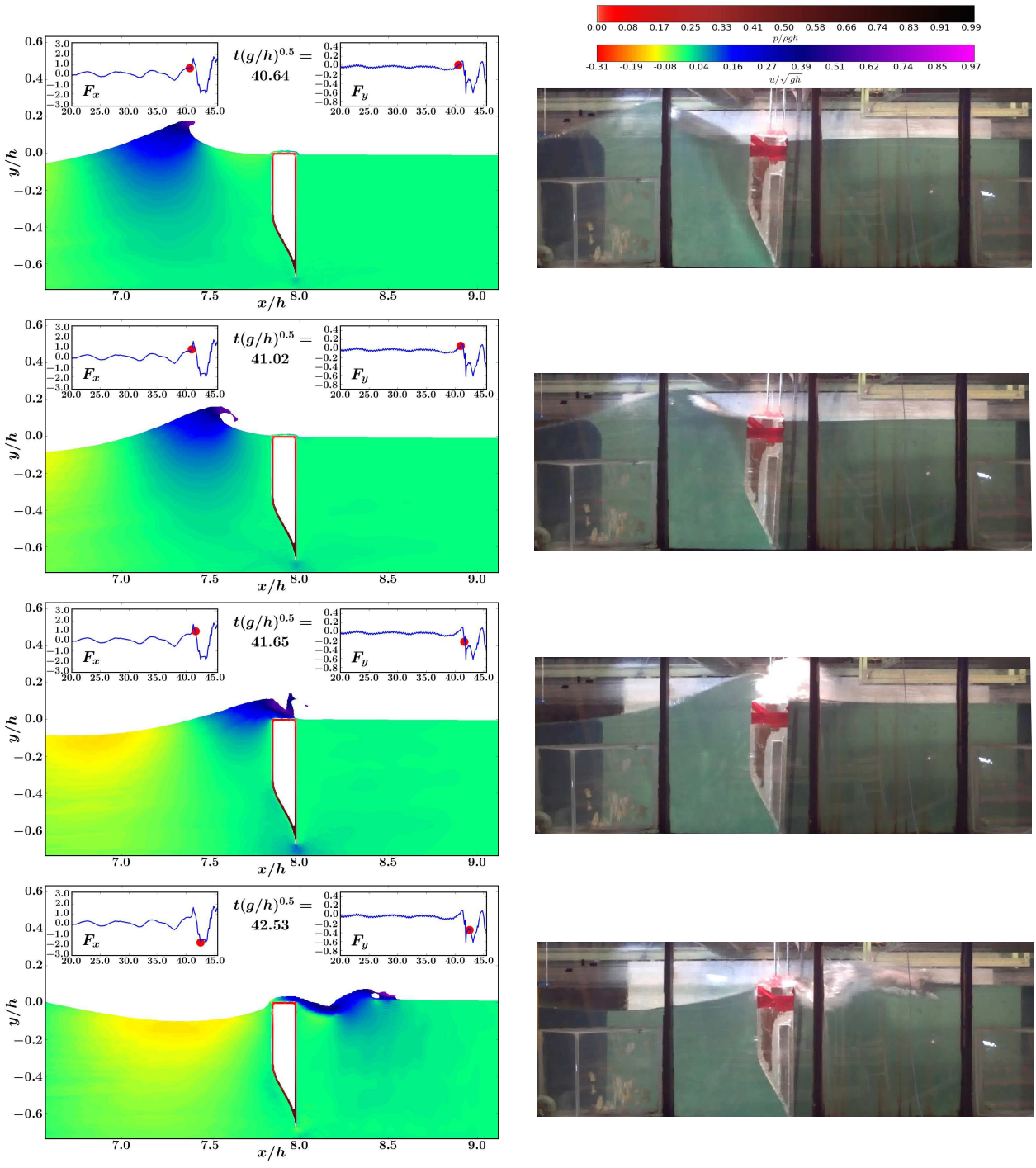

Figure 3.18: The fully submerged AF ($D = 1.03$ m) encountering a plunging breaker, WC-SPH computations on the left and experiments on the right. The color-bars indicate the pressure on the AF and x-component of fluid particle velocity.

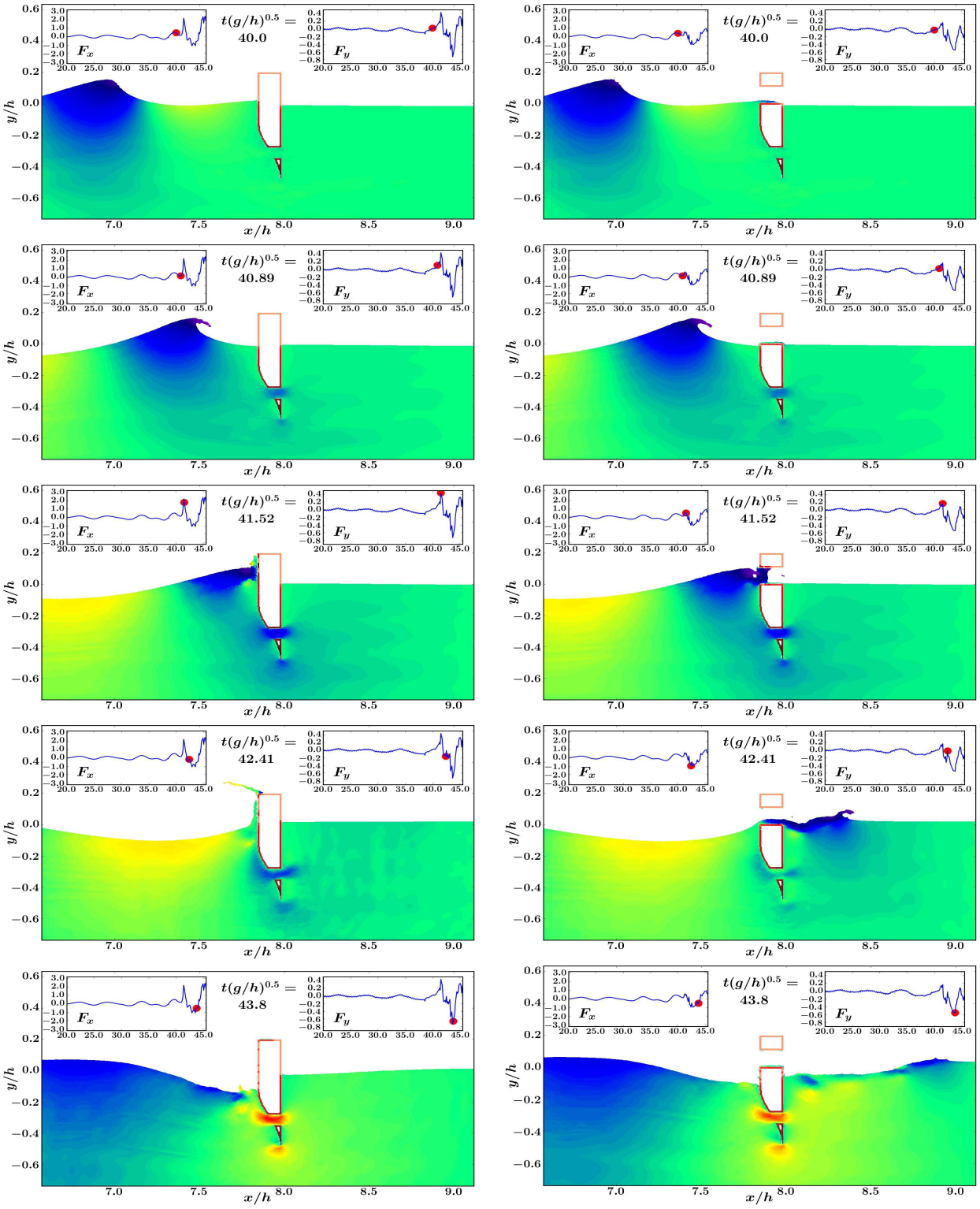

Figure 3.19: The Berkeley Wedge encountering a plunging breaker analyzed by WCSPH method ($D = 0.8$ m). Two cases of the AF with one PRC (left column) and two PRCs (right column) are presented side by side.

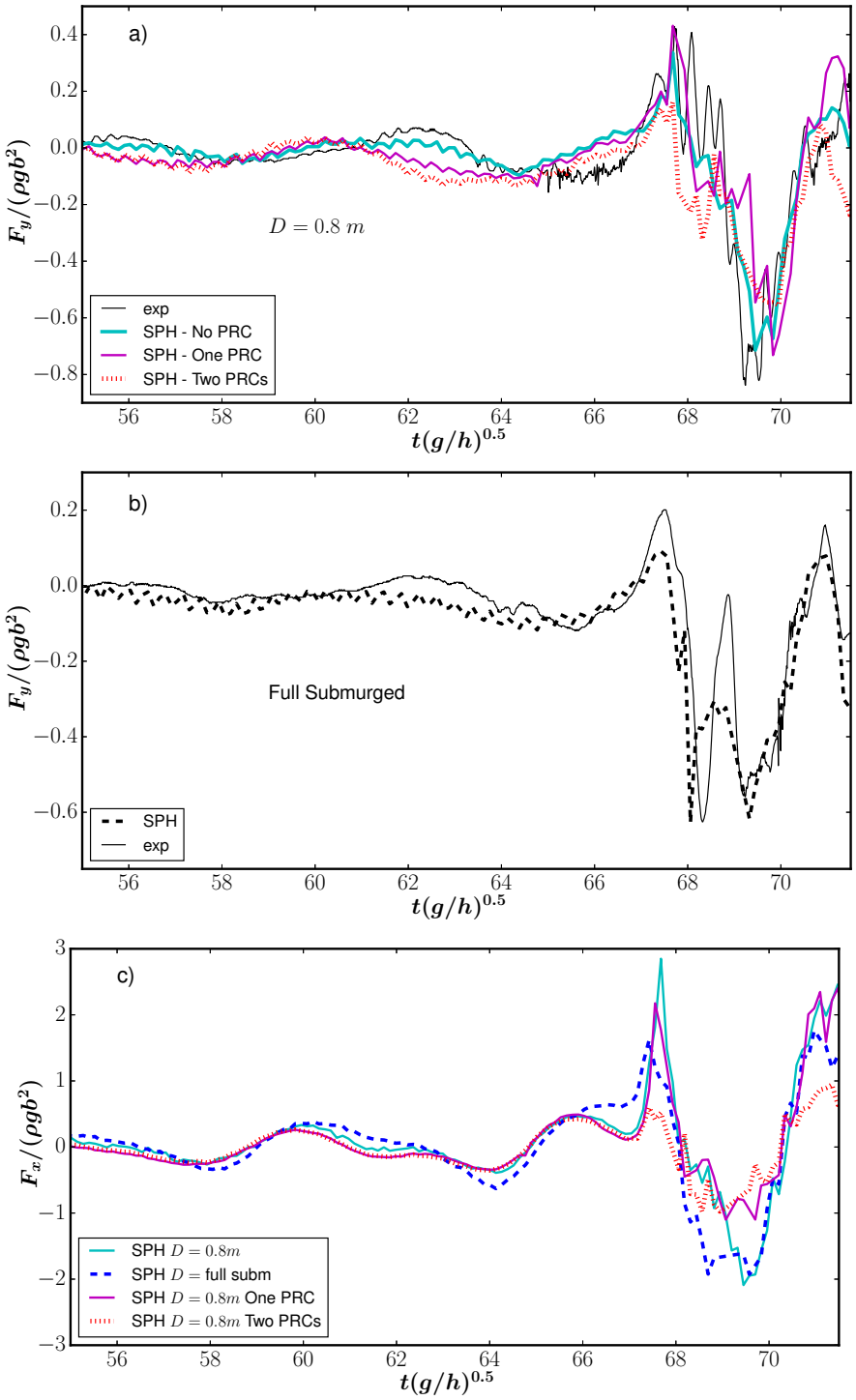

Figure 3.20: Comparison of the heave wave exciting forces on the AF obtained from experiments and computations for a) $D = 0.8$ m (operational condition draft) and b) $D = 1.03$ m (the fully submerged draft). c) The surge wave exciting forces obtained by computations for the 0.8 m draft AF with zero, one, and two PRCs as well as the fully submerged draft.

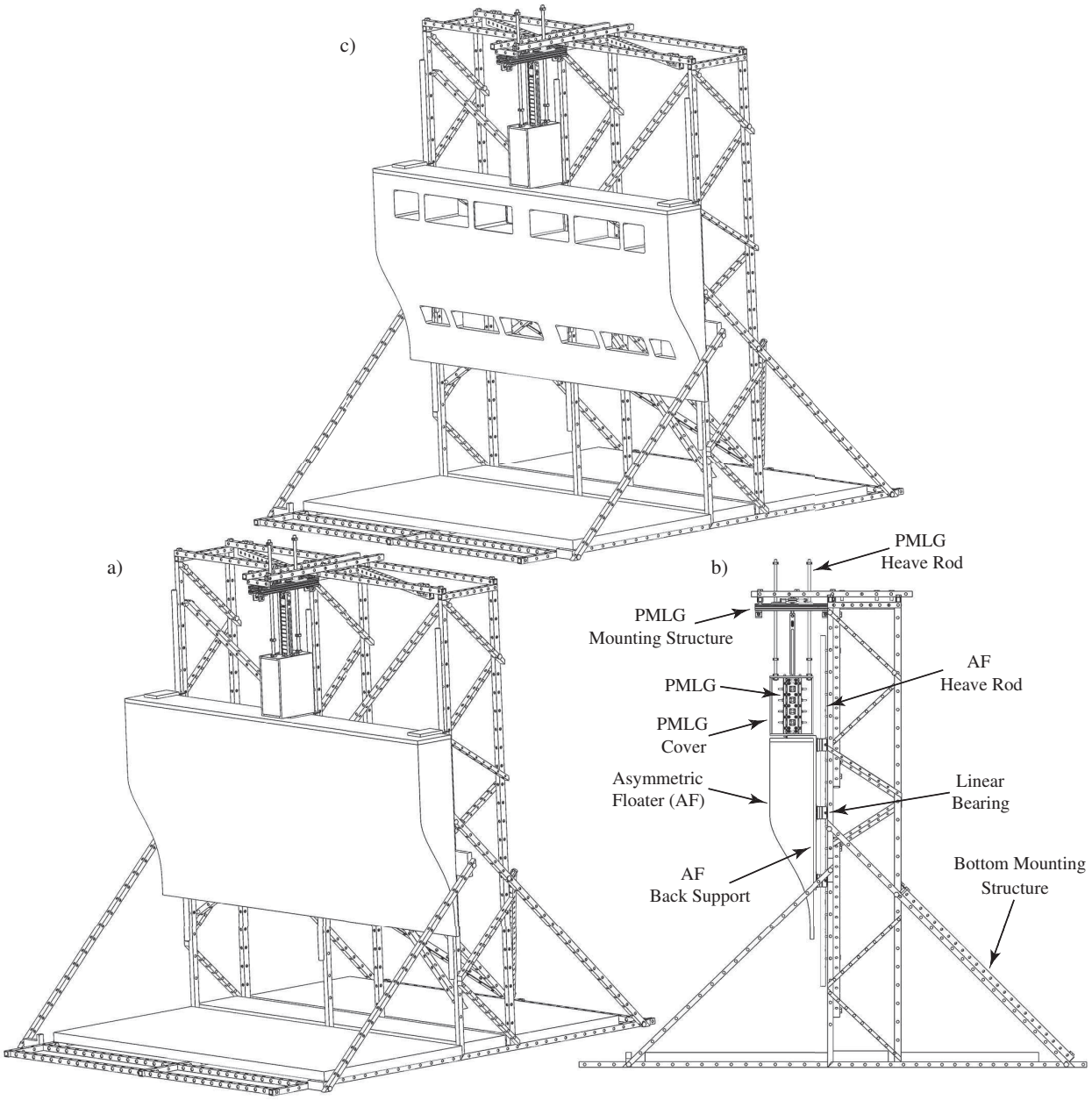

Figure 3.21: Schematic representations of a) operational (isometric view), b) operational (side view), and c) survivability (isometric view) modes of TBW. For the cases a and b (isometric and side views), the PRCs (imbedded on the AF) are closed and the AF has a smooth surface. The power-take-off system shown is a linear permanent magnet generator (LPMG) and was developed at the Berkeley Marine Mechanics Laboratory (BMML).

3.7 Effects of Draft (D) on Wave Force

3.7.1 Experimental Setup

In addition to the operational (0.8 m) and fully submerged (1.03 m) drafts of the AF, other drafts of the AF such as 0.6 m, 0.7 m, and 0.9 m were adopted. The extreme forces were measured on the AF with these drafts to analyze the effects of these different drafts of the AF on decreasing the extreme wave forces. Water ballast was used to obtain different drafts of the AF as shown in Fig. 3.22.

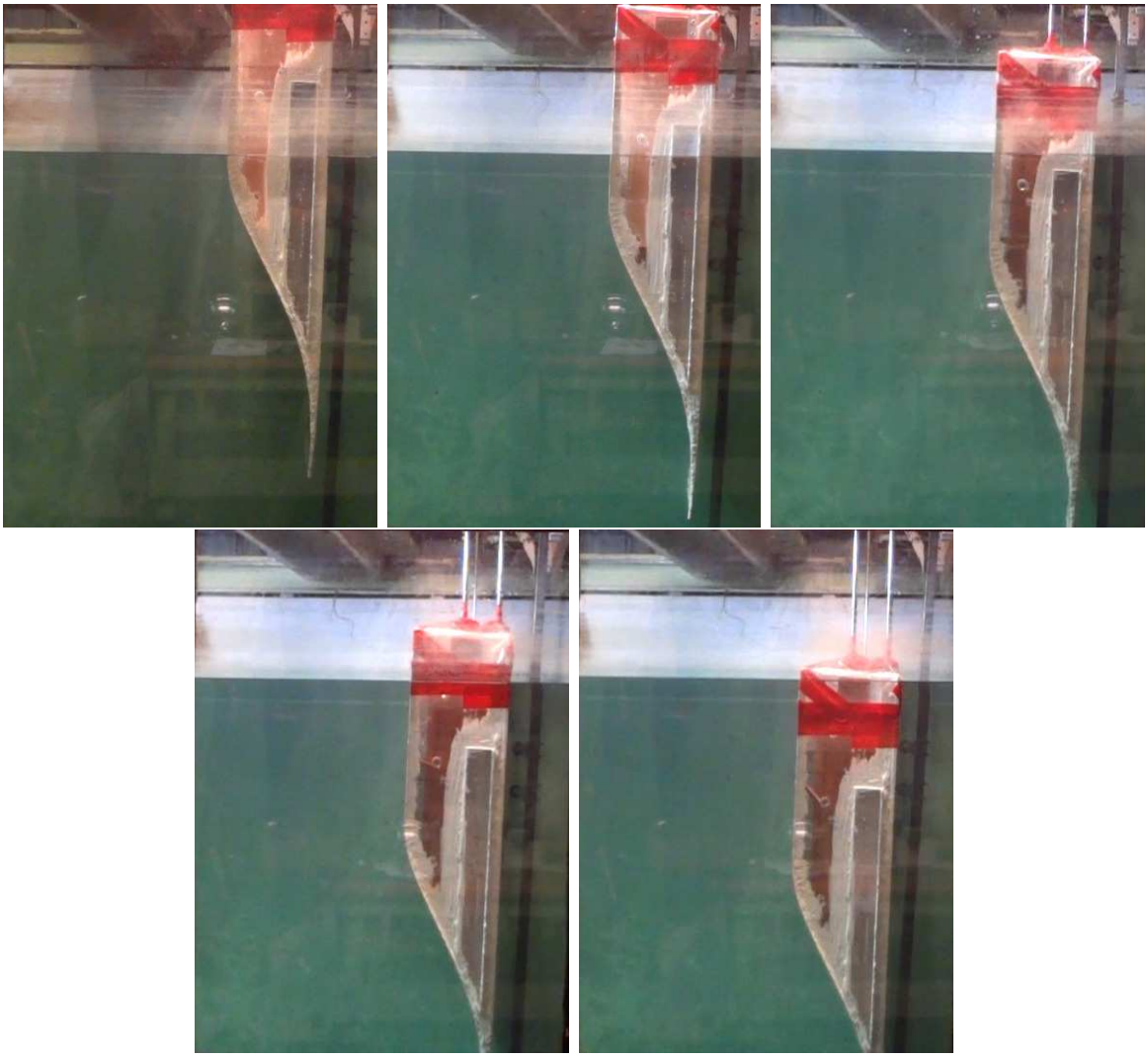

Figure 3.22: Experimental setup for analyzing the heave wave exciting force under breaking waves. Drafts shown are 0.6 m, 0.7 m, 0.8 m, 0.9 m, and 1.03 m.

3.7.2 Experimental Measurement of F_y

The experimental setup and force measurement procedure are mentioned in details in Section. 3.5.1. The same procedure was carried out to to measure the force on the AF with different drafts. For the AF with the drafts of 0.8 m, 0.7 m, 0.6 m as shown in Figs. 3.17, 3.24, and 3.23, less over-toping flow behavior was observed when comparing to the AF with the deeper drafts of 0.9 m and 1.03 m as demonstrated in Figs. 3.25 and 3.18. The experimental measurements of the F_y on the AF with these five different drafts are presented in Fig. 3.26. The vertical forces that were measured on the AF with 1.03 m and 0.9 m drafts, had three peaks. The first peak ($F_y > 0$) was the result of the initial impact of the plunging breaker with the AF. The second peak $F_y < 0$ was the result of slamming of the breaking waves on the top of the AF. The third peak $F_y < 0$ was caused by the trough of the breaking waves. As the trough reached the floater the water level near the floater declined which caused the third peak in the F_y. The second peak in the F_y was not present in the cases of the AF with 0.8 m, 0.7 m, 0.6 m drafts. The frontal area of the AF facing the waves, when sufficiently above the water level, this area absorbs most of the impact force and prevents water from slamming on the top part of the AF. As we decreased the drafts of the AF, from 1.03 m to 0.6 m, we increased the frontal area of the AF that is above the water line. Thus, the initial peak of the F_y increased. The small portion of the 0.9 m draft AF that was above the water line absorbed some of the initial impact, thus reducing the slamming force on the top part of the floater when comparing to the case of 1.03 m draft. The third peak value of the F_y, that was the result of a drop in the water level, was the lowest for the case of 1.03 m draft AF.

In the case of extreme waves, reducing the draft of the AF or completely lifting it out of the water increases the frontal area of the floater and causes larger forces on it. Also, in the presence of extreme waves, the areas of the AF with lower structural support (tip of the AF) is exposed to high stress. Additionally, lifting the floater requires change in ballast and detachment of the PTO. Thus, raising the floater is an impractical solution for the survivability of TBW and similar floaters.

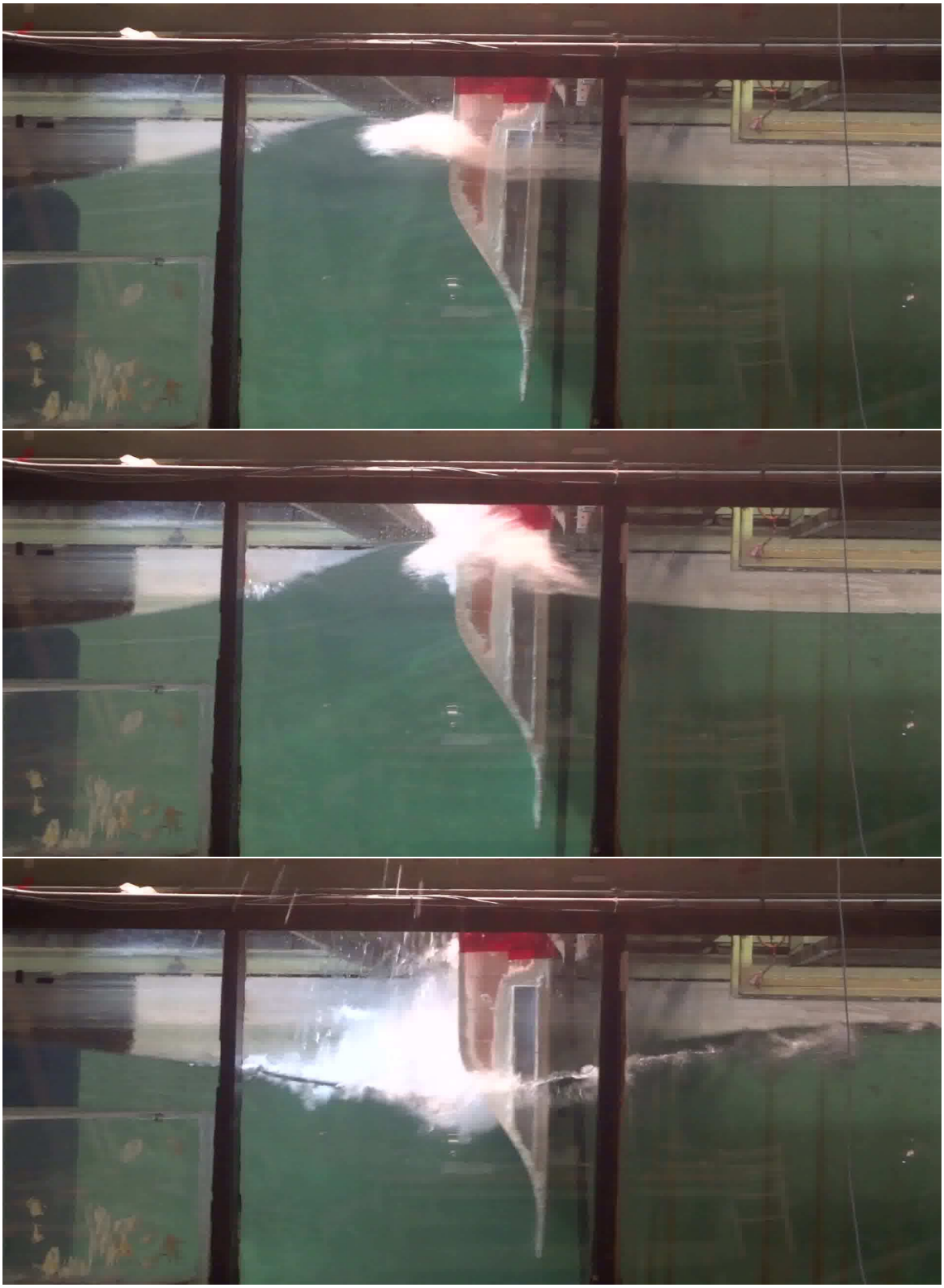

Figure 3.23: The AF with 0.6 m draft encountering breaking waves.

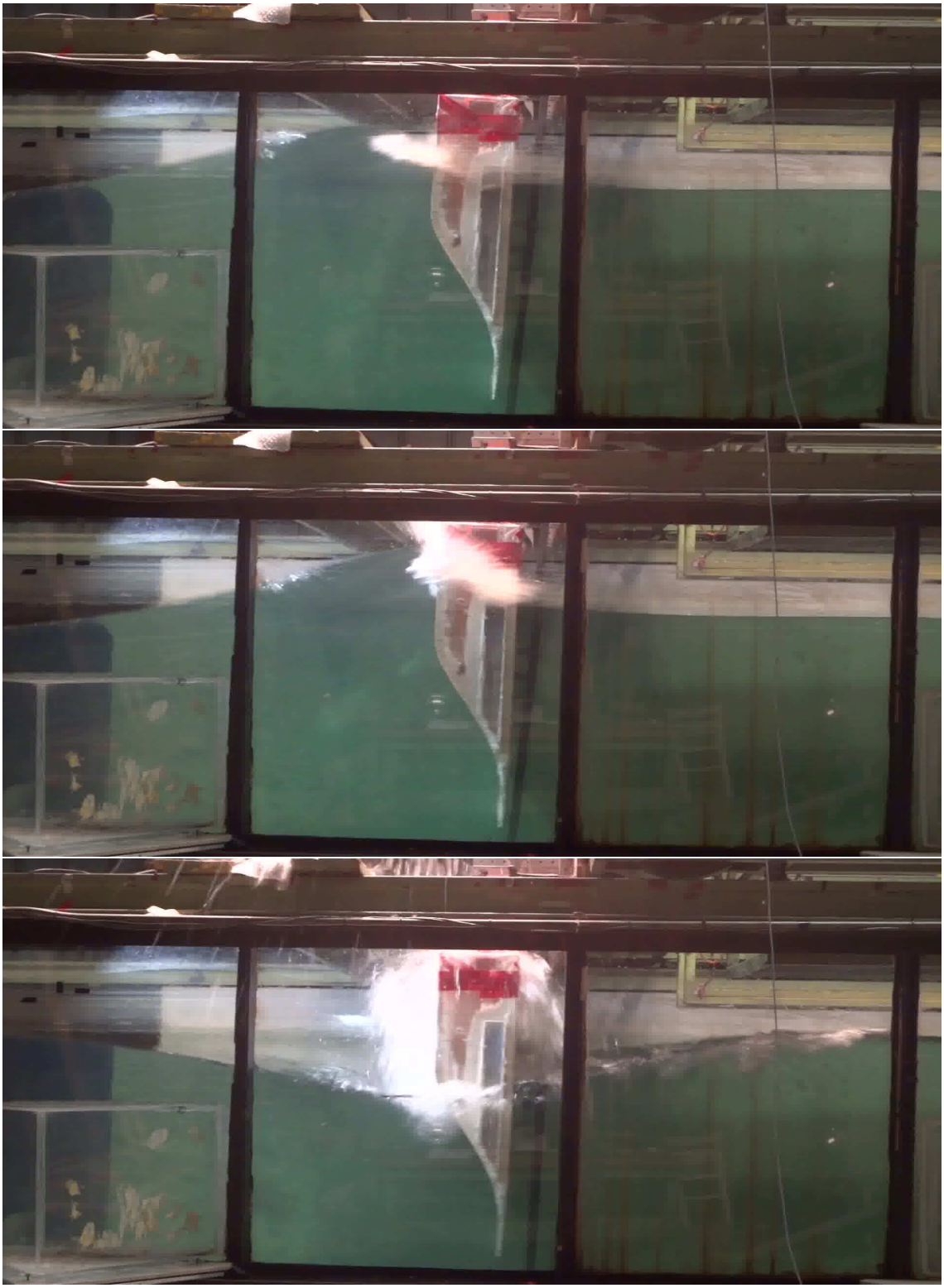

Figure 3.24: The AF with 0.7 m draft encountering breaking waves.

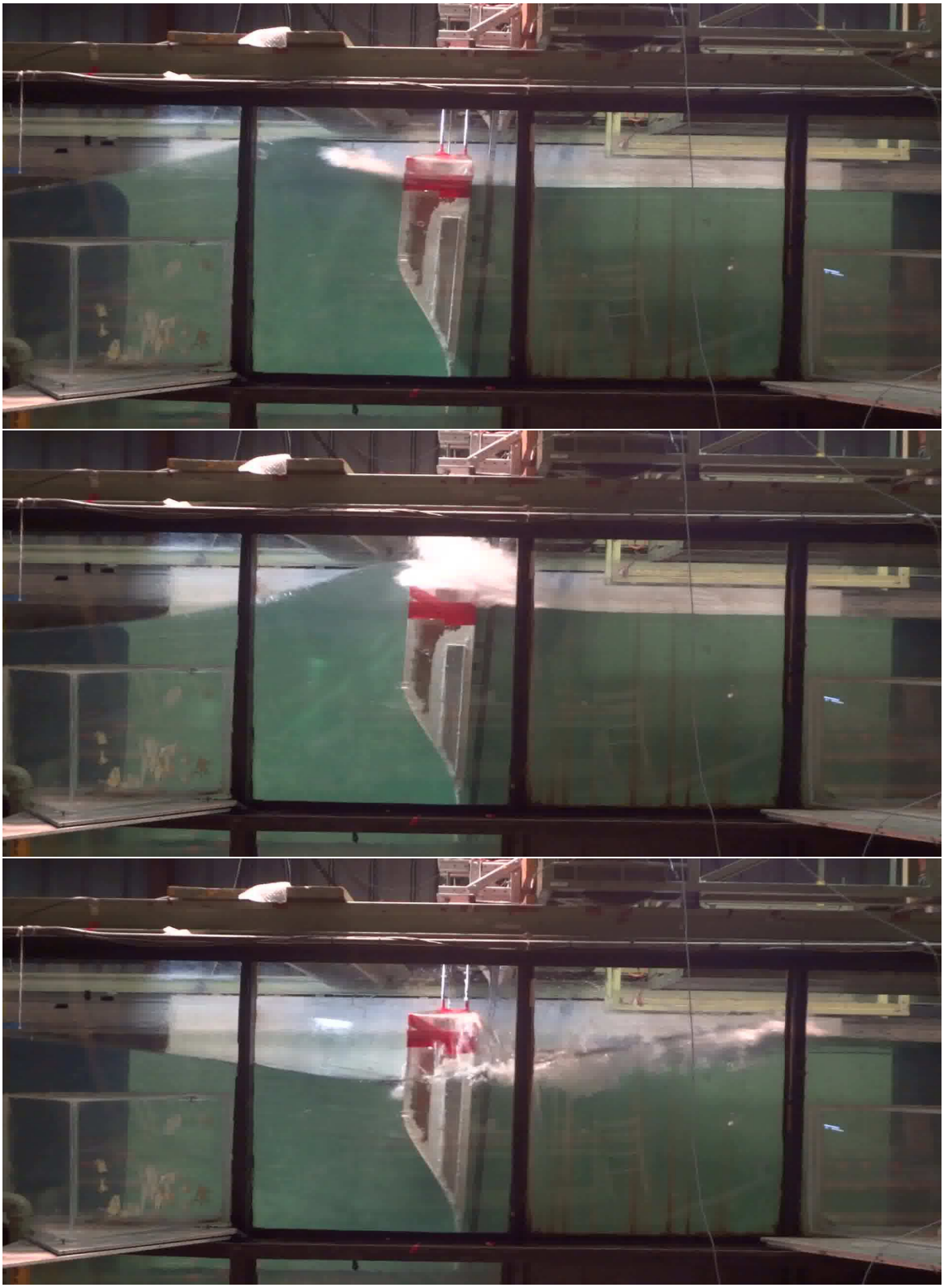

Figure 3.25: The AF with 0.9 m draft encountering breaking waves.

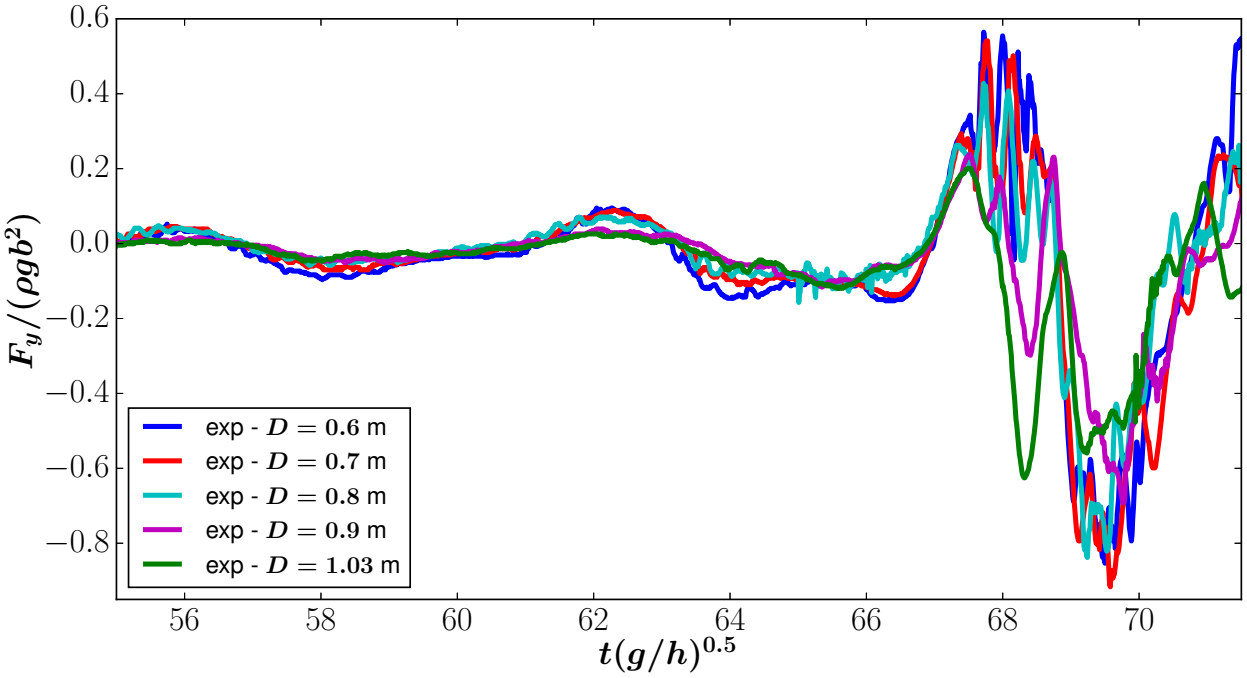

Figure 3.26: Comparison of the heave wave exciting forces on the AF with five different drafts obtained from experiments.

Chapter 4

Summary, Discussions, and Conclusions

In this thesis, we analyzed the operational and survivability conditions of the AWECs by employing a novel AWEC/breakwater, TBW as an example. In the operational condition we described how pseudo-spectral optimal control was used to optimize the performance of TBW. The analysis revealed that the power capture efficiency increases by 50% for lower frequencies ($\bar{\sigma} < 0.74$) compared to results obtained from a passive PTO with a constant linear damper. For frequencies greater than $\bar{\sigma} > 0.74$, a capture efficiency of unity can be achieved which is remarkable; however, as the wave frequency moves away from resonance a greater reactive power component is required. Though the maximum capture efficiency is lower when frequency is below resonance, the surge-restraining force and pitch-restraining torque are also lower, in the range of $0.5 \leq \bar{\sigma} \leq 0.7$, for the maximum constrained heave motion than with passive control. Thus, when operating slightly below the resonance frequency with a PTO that allows for bidirectional energy flow, lower restraint forces and torques will be observed, thereby leading to favorable power-to-load ratios. The magnitude and phase of heave motion required to cancel the surge-restraining force and pitch-restraining torque were calculated to show that greater PTO control forces and reactive power is required for achieving such performance.

The pseudo-spectral optimal control problem was improved by including the squared ℓ^2-norm of the surge-restraining force, pitch-restraining torque, and PTO actuator force in the objective function. The optimizer performance was found to be adjustable based on the values chosen for the separate penalty weights (γ_1 and β_m are penalty weights applied to the surge foundation force and the control force magnitude, respectively) placed on the three load contributions; however, it was found that because of WEC dynamics, reducing either the surge-restraint force or pitch-restraint torque would lead to a reduction in the other. Thus, penalizing one of the contributions in the objective function was sufficient to explore the power-to-load ratios. Two incident wave periods above and below the resonance frequency, with a wave amplitude of 0.02 m and maximum allowable heave displacement of 0.1 m, were used to analyze the pseudo-spectral controller. When the penalty weights $\gamma_1 \to 0$ and $\beta_m \to 0$, maximum power capture was recovered with minimal reduction in system loads. The case of $\gamma_1 \to \infty$ and $\beta_m \to \infty$ would significantly reduce restraint loads; however, at the expense of greater PTO forces and reactive power requirements. If the penalty weights are kept with the range of $\beta_m \geq 0.8$ and $\gamma_1 \leq 0.4$, an increase in capture efficiency of 20% to 80% is obtainable with the reactive power comprising no more than 1/10th of the TAP. In the same region, where the surge-restraining force and pitch-restraining torque were reduced between 20%–30% with little to no increase in PTO force. This work has highlighted some of the issues that arise when WEC control focuses solely on maximizing power absorption as

it is accompanied by proportionately greater structural and PTO loads that lead to a higher level cost of energy. In the future, pursuit of moderate gains in TAP from control strategies may be more favorable as the increase in power absorption may outpace the growth in structural loads.

Furthermore, we have investigated the wave exciting forces on the AWECs when encountering the deep-water breaking waves and proposed solutions to improve their survivability. For generating deep-water breaking waves at the two intended locations of 11 m and 21 from the wavemaker, we obtained two time-histories of the wavemakers displacements by means of the linear potential-flow theory. It was demonstrated that the generated deep-water breaking waves at the two locations in the CWT matched with the ones obtained in the PWT. These confirming results allowed the measurements of the force to be done at 22 m in PWT (location of PWT's visual window) and at 12 m in CWT (to reduce computational costs). The physical and numerical models of the AF were positioned further downstream from the waves water-entry to analyze a jet-like-flow impact.

Two drafts were chosen for the force measurements; 0.8 m (operational mode) and 1.03 m (fully submerged for survival mode). The initial jet-flow impact, effected an impulsive repellent vertical ($F_y > 0$) and horizontal ($F_x > 0$) forces on the 0.8 m draft AF. Later in time, the trough of the plunging breaker declined the water level in front of the AF thus, inducing a wide-band suction ($F_x < 0$) and downward ($F_y < 0$) forces. The F_y peak values were an order of magnitude smaller than the F_x. Submerging the AF resulted in a reduction in the F_y peak at the initial impact. On the other hand, there was no dramatic change in the secondary peak of the F_y. Similar behaviors were seen in the F_x values that were obtained by computations.

Additionally, the effects of the drafts of the AF on the F_y were analyzed experimentally. It was shown that decreasing the draft of the AF, from 1.03 m to 0.6 m, increases the F_y experienced by the floater. Lowering the draft of the AF exposes its tip (that has low structural stiffness) to extreme waves. Also, lifting the floater requires reducing the ballast and PTO detachment. Thus, raising the AF out of water is not a practical or efficient method for the survivability of TBW.

To mitigate the effects of the extreme waves on the AF while *maintaining its operational draft*, a novel design concept of using Pressure-Relief Channel (PRC), allowing water to flow through the AF, was presented and computationally tested. Placing the bottom PRC at the 0.8 m draft AF reduced the F_x by approximately 24% in the initial peak and by 50% in the secondary peak. On the contrary, this had an insignificant effect on reducing the peak values of the F_y. Placement of the top PRC in addition to the bottom one, reduced the repellent and suction parts of the F_y by more than 50%. More importantly, the repellent peak of the F_x was almost eliminated and the suction peak of the F_x was decreased by more than 50%. Therefore, we proved that implementing the PRCs, while fixing the motion of the AF, is an effective solution for the survivability of TBW.

Finally, we proposed a design for the implementation of the PRCs and demonstrated the operational and survivability layouts of TBW as displayed in Fig. 3.21. For the operational mode, the PRCs are closed; the top PRCs are empty and the bottom PRCs are filled with

water. When large waves beyond the tolerance of TBW are sensed, the motion of the AF is fixed and the PRCs open up while maintaining the operational mode draft. After extreme waves have passed, the PRCs are closed, the AF is released, and its operational condition resumes. Similarly, this research finding provides a very practical and effective method to improve the survivability of the offshore and nearshore structures in extreme waves.

To further expand the present study, it is of importance to extend the pseudo-spectral control in the irregular waves to analyze the effectiveness of the control methodology in reducing the fatigue load on the system. In addition, more analysis is needed to study the non-ideal PTO effect on the global power-to-load ratio of the system. More work can be done to analyze the 3D effects of the PRCs on the overall forces that TBW experiences in breaking waves. Also, it is of great interest to study the effect of oblique extreme waves on TBW, with and without the PRCs.

Bibliography

[1] M. Z. Jacobson, "Short-term effects of controlling fossilfuel soot, biofuel sootand gases, and methane on climate, arctic ice, and airpollution health," *Journal of Jeophysical Research*, vol. 115, no. 10.1029/2009JD013795, 2010, 2010.

[2] J. Twidell and T. Weir, *Renewable Energy Resources, 3rd Edition*. New York: Routledge, 2015.

[3] G. Mørk, S. Barstow, A. Kabuth, and M. T. Pontes, "Assessing the global wave energy potential," in *Proceedings of the 29th International Conference on Ocean, Offshore and Arctic Engineering*, no. OMAE2010–20473, Shanghai, China, June 6-11 2010.

[4] Z. Chongwei, S. Longtan, S. Wenli, S. Qin, L. Gang, L. Xunqiang, and C. Xiaobin, "An assessment of global ocean wave energy resources over the last 45 a," *Acta Oceanologica Sinica*, vol. 33, no. 1, pp. 92–101, 2014.

[5] F. Madhi, M. E. Sinclair, and R. W. Yeung, "The "Berkeley Wedge": an asymmetrical energy-capturing floating breakwater of high performance," *Marine System and Technology, Journal of SOBENA*, vol. 9, no. 1, pp. 5–16, 2014.

[6] I. López, J. Andreu, S. Ceballos, I. M. de Alegría, and I. Kortabarria, "Review of wave energy technologies and the necessary power–equipment," *Renewable and Sustainable Energy Reviews*, vol. 27, pp. 413–434, 2013.

[7] R. G. Coe and V. S. Neary, "Review of methods for modeling wave energy converter survival in extreme sea states," in *Proceedings of the 2nd Marine Energy Technology Symposium*, Seattle, WA, April 15-18 2014.

[8] W. Musial, M. Lawson, and S. Rooney, "Marine hydrokinetic technology (MHK) instrumentation, measurement, and computer modeling workshop," National Renewable Energy Laboratory, Boulder, CO., Tech. Rep. NREL/TP-5000-57605, 2013.

[9] H. Eidsmoen, "Optimum control of a floating wave-energy converter with restricted amplitude," *Journal of Offshore Mechanics and Arctic Engineering*, vol. 118, no. 2, pp. 96–102, 1996.

[10] J. Hals, J. Falnes, and T. Moan, "Constrained optimal control of a heaving buoy wave-energy converter," *Journal of Offshore Mechanics and Arctic Engineering*, vol. 133, no. 1, p. 011401, 2011.

[11] N. Tom and R. W. Yeung, "Non-linear model predictive control applied to a generic ocean-wave energy extractor," in *Proceedings of the 32nd International Conference on*

Ocean, Offshore and Arctic Engineering, no. OMAE2013-11247, Nantes, France, June 9-14 2013.

[12] J. A. M. Cretel, G. Lightbody, G. P. Thomas, and A. W. Lewis, "Maximisation of energy capture by a wave-energy point absorber using model predictive control," in *Proceedings of the 18th World Congress of the International Federation of Automatic Control*, Milano, Italy, 2011, pp. 3714–3721.

[13] E. Abraham and E. C. Kerrigan, "Optimal active control and optimization of a wave energy converter," *IEEE Transactions on Sustainable Energy*, vol. 4, no. 2, pp. 324–332, 2013.

[14] G. Li and M. R. Belmont, "Model predictive control of sea wave energy converters – part I: A convex approach for the case of a single device," *Journal of Renewable Energy*, vol. 69, pp. 453–463, 2014.

[15] G. Bacelli, J. V. Ringwood, and J. Gilloteaux, "A control system for a self-reacting point absorber wave energy converter subject to constraints," in *Proceedings of the 18th World Congress of the International Federation of Automatic Control*, Milano, Italy, 2011, pp. 11 387–11 392.

[16] D. R. Herber and J. T. Allison, "Wave energy extraction maximization in irregular ocean waves using pseudospectral methods," in *Proceedings of the ASME International Design Engineering Technical Conferences and Computers and Information in Engineering Conference*, Portland, OR, USA, 2013.

[17] N. M. Tom, Y. H. Yu, M. J. Lawson, and A. D. Wright, "Pseudo-spectral control of a novel oscillating surge wave energy converter in regular waves, part I: power optimization including load reduction," *under review*, 2016.

[18] J. Falnes, "Optimum control of oscillation of wave-energy converters," *International Journal of Offshore and Polar Engineering*, vol. 12, no. 2, pp. 47–154, 2002.

[19] A. Babarit and A. Clément, "Optimal latching control of a wave energy device in regular and irregular waves," *Journal of Applied Ocean Research*, vol. 28, pp. 77–91, 2006.

[20] A. Babarit, M. Guglielmi, and A. H. Cle ment, "Declutching control of a wave energy converter," *Journal of Ocean Engineering*, vol. 36, no. 12, pp. 1015–1024, 2009.

[21] Y.-H. Yu, J. V. Rij, R. Coe, and M. Lawson, "Preliminary wave energy converters extreme load analysis," in *Proceedings of the 34th International Conference on Ocean, Offshore and Arctic Engineering*, no. OMAE2015-41532, St. John's, Newfoundland, Canada, May 31- June 5 2015.

[22] P. Brevig, M. Greenhow, and T. Vinje, "Extreme wave forces on submerged wave energy devices," *Journal of Apldied Ocean Research*, vol. 4, no. 4, pp. 219–225, 1982.

[23] M. Greenhow, *Survival of Surface-Piercing Wave Energy Devices in Extreme Waves*. Berlin, Heidelberg: Springer, 1986, pp. 357–373.

[24] M. Greenhow, T. Vinje, P. Brevig, and J. Taylor, "A theoretical and experimental study of the capsize of salter's duck in extreme waves," *Journal of Fluid Mechanics*, vol. 118, pp. 221–239, 1982.

[25] M. Göteman, J. Engström, M. Eriksson, and M. Leijon, "Wave loads on a point-absorbing wave energy device in extreme waves," *Journal Ocean and Wind Energy*, vol. 2, no. 3, 2015.

[26] M. Landrini, A. Colagrossi, M. Greco, and M. P. Tulin, "Gridless simulations of splashing processes and near-shore bore propagation," *Journal of Fluid Mechanics*, vol. 591, pp. 183–213, 2007.

[27] D. D. Padova, R. A. Dalrymple, M. Mossa, and A. F. Petrillo, "SPH simulations of regular and irregular waves and their comparison with experimental data," arXiv:0911.1872, 2009.

[28] M. H. Dao, H. Xu, E. S. Chan, and P. Tkalich, "Numerical modelling of extreme waves by smoothed particle hydrodynamics," *Natural Hazards and Earth System Sciences*, vol. 11, pp. 419–429, 2011.

[29] M. Antuono, A. Colagrossi, S. Marrone, and C. Lugni, "Propagation of gravity waves through an SPH scheme with numerical diffusive terms," *Journal of Computer Physics Communications*, vol. 182, pp. 866–877, 2011.

[30] A. Rafiee, S. Cummins, M. Rudman, and K. Thiagarajan, "Comparative study on the accuracy and stability of SPH schemes in simulating energetic free-surface flows," *European Journal of Mechanics B/Fluids*, vol. 36, no. 1-16, 2012.

[31] S. D. Chowdhury and S. A. Sannasiraj, "Numerical simulation of 2D wave impact pressure using SPH schemes," in *Proceedings of the Twenty-third International Offshore and Polar Engineering*, Anchorage, Alaska, USA, June 30–July 5 2013.

[32] H. Gotoh, S. Shao, and T. Memita, "SPH-LES model for numerical investigation of wave interaction with partially immersed breakwater," *Coastal Engineering Journal*, vol. 46, no. 1, pp. 39–63, 2004.

[33] A. Khayyer, H. Gotoh, and S. Shao, "Enhanced predictions of wave impact pressure by improved incompressible SPH methods," *Journal of Applied Ocean Research*, vol. 31, pp. 111–131, 2009.

[34] K. Pan, R. H. A. IJzermans, B. D. Jones, A. Thyagarajan, B. W. H. van Beest, and J. R. Williams, "Application of the SPH method to solitary wave impact on an offshore platform," *Journal of Computational Particle Mechanics*, vol. 3, pp. 155–166, 2016.

[35] A. Rafiee, D. Dutykh, and F. Dias, "Numerical simulation of wave impact on a rigid wall using a two–phase compressible SPH method," *Procedia IUTAM*, vol. 18, pp. 123 – 137, 2015.

[36] M. H. Dao, H. Xu, E. S. Chan, and P. Tkalich, "Modelling of tsunami-like wave run-up, breaking and impact on a vertical wall by SPH method," *Natural Hazards and Earth System Sciences*, vol. 13, pp. 3457–3467, 2013.

[37] R. W. Yeung, A. Peiffer, N. Tom, and T. Matlak, "Design, analysis, and evaluation of the UC-Berkeley wave-energy extractor," *Journal of Offshore Mechanics and Arctic Engineering*, vol. 134, no. 021902, 2012.

[38] N. Tom and R. W. Yeung, "Performance enhancements and validations of the UC-Berkeley ocean-wave energy extractor," *Journal of Offshore Mechanics Arctic Engineering*, vol. 135, no. 2, p. 041101, 2013.

[39] N. Tom, "Confirmation of a nonlinear model predictive control strategy applied to a permanent magnet linear generator for wave-energy conversion," in *Proceedings of the 33rd International Conference on Ocean, Offshore and Arctic Engineering*, no. OMAE2014-24711, San Francisco, California, USA, June 8-13 2014.

[40] N. Tom, D. Son, V. Belissen, and R. W. Yeung, "Modeling of a permanent magnet linear generator for wave-energy conversion," in *Proceedings of the 34th International Conference on Ocean, Offshore and Arctic Engineering*, no. OMAE2015-42370, St. John's, Newfoundland, Canada, May 31- June 5 2015.

[41] D. Son, V. Belissen, and R. W. Yeung, "Optimizing the performance of a dual coaxial–cylinder wave–energy extractor," in *Proceedings of the 34th International Conference on Ocean, Offshore and Arctic Engineering*, no. OMAE2015-42379, St. John's, Newfoundland, Canada, May 31–June 5 2015.

[42] R. W. Yeung, J. V. Wehausen, and W. C. Webster, "Hydrodynamics of ships and ocean systems - II," University of California at Berkeley, Lectures Notes for The Course NAOE-241b, 1983.

[43] R. W. Yeung, "A hybrid integral-equation method for time-harmonic free surface flows," in *Proceedings of the 1st International Conference on Numerical Ship Hydrodynamics*. Gaithersburg, MD, 1975, pp. 58–607.

[44] W. E. Cummins, "The impulse response function and ships motions," *Schiffstechnik*, vol. 9, pp. 101–109, 1962.

[45] T. F. Ogilvie, "Recent progress towards the understanding and prediction of ship motions," in *Proceedings of the Fifth Symposium on Naval Hydrodynamics*, Bergen, Norway, Sept. 1964, pp. 3–79.

[46] D. V. Evans, "A theory for wave-power absorption by oscillating bodies," *Journal of Fluid Mechanics*, vol. 7, no. 1, pp. 1–25, 1976.

[47] J. Hals, T. Bjarte-Larsson, and J. Falnes, "Optimum reactive control and control by latching of a wave-absorbing semisubmerged heaving sphere," in *Proceedings of the 21st International Conference on Offshore Mechanics and Arctic Engineering*, Oslo, Norway, June 22-28 2002, pp. 415–423.

[48] D. V. Evans, "Maximum wave-power absorption under motion constraints," *Journal of Applied Ocean Research*, vol. 3, no. 4, pp. 200–203, 1981.

[49] G. Bacelli and J. V. Ringwood, "Numerical optimal control of wave energy converters," *IEEE Transactions on Sustainable Energy*, vol. 6, no. 2, pp. 133–145, 2015.

[50] R. Genest, F. Bonnefoy, A. H. Clément, and A. Babarit, "Effect of non-ideal power take-off on the energy absorption of a reactively controlled one degree of freedom wave energy converter," *Journal of Applied Ocean Research*, vol. 48, pp. 236–243, 2014.

[51] J. Monaghan, "Simulating free surface flows with SPH," *Journal of Computational Physics*, vol. 110, pp. 399–406, 1994.

[52] S. Adami, X. Hu, and N. Adams, "A generalized wall boundary condition for smoothed particle hydrodynamics," *Journal of Computational Physics*, vol. 231, pp. 7057–7075, 2012.

[53] J. P. Morris, P. J. Fox, and Y. Zhu, "Modeling low Reynolds number incompressible flows using SPH," *Journal of Computational Physics*, vol. 136, pp. 214–226, 1997.

[54] J. J. Monaghan and J. C. Lattanzio, "A refined particle method for astrophysical problems," *Journal of Astronomy and Astrophysics*, vol. 149, pp. 135–143, 1985.

[55] M. Liu, G. Liu, and K. Lam, "Constructing smoothing functions in smoothed particle hydrodynamics with applications," *Journal of Computational and Applied Mathematics*, vol. 155, pp. 263–284, 2003.

[56] J. J. Monaghan, "Smoothed particle hydrodynamics," *Reports on Progress in Physics*, vol. 68, pp. 1703–1759, 2005.

[57] L. Verlet, "Computer "experiments" on classical fluids. I. thermodynamical properties of lennard-jones molecules," *Phys. Rev.*, vol. 159, pp. 98–103, Jul 1967.

[58] P. Ramachandran and C. Kaushik, "PySPH: A python framework for smoothed particle hydrodynamics," in *Proc. of the 9th Python In Science Conf.*, 2010.

[59] J. P. Hughes and D. I. Graham, "Comparison of incompressible and weakly-compressible SPH models for free-surface water flows," *Journal of Hydraulic Research*, vol. 48, pp. 105–117, 2010.

[60] J. J. Monaghan, "Smoothed particle hydrodynamics," *Annual Review of Astronomy and Astrophysics*, vol. 30, 1992.

[61] A. Ferrari, M. Dumbser, E. F. Toro, and A. Armanini, "A new 3D parallel SPH scheme for free surface flows," *Computers & Fluids*, vol. 38, pp. 1203–1217, 2009.

[62] J. V. Wehausen and E. V. Laitone, *Surface Waves in Fluid Dynamics III.* URL: http://www.coe.berkeley.edu/SurfaceWaves: In Handbuch der Physik, Springer Verlag, 1960, vol. IX, ch. 3, pp. 446–778.

[63] J. C. Martin and W. J. Moyce, "Part IV. an experimental study of the collapse of liquid columns on a rigid horizontal plane," *Philosophical Transactions of the Royal Society of London A: Mathematical, Physical and Engineering Sciences*, vol. 244, pp. 312–324, 1952.

[64] Z. Zhou, J. D. Kat, and B. Buchner, "A nonlinear 3-D approach to simulate green water dynamics on deck," in *Proceedings of the 7th International Conference on Numerical Ship Hydrodynamics*, 1999.

[65] A. Colagrossi and M. Landrini, "Numerical simulation of interfacial flows by smoothed particle hydrodynamics," *Journal of Computational Physics*, vol. 191, pp. 448–475, 2003.

[66] S.-W. Liao and D. Roddier, "Generation of plunging breakers - laboratory and numerical simulation," University of California at Berkeley, Tech. Rep., 1998.

[67] D. G. Dommermuth, D. K. P. Yue, W. M. Lin, and R. J. Rapp, "Deep-water plunging breakers: a comparison between potential theory and experiments," *Journal of Fluid Mechanics*, vol. 189, pp. 423–442, 1988.

[68] J. N. Newman, "The exciting forces on fixed bodies in waves," Dept. of the Navy, David Taylor Model Basin in Washington, D.C., Tech. Rep., 1963.

Appendix A

Wave Exciting Force and Far-field Radiated Waves

In order to obtain a relation between the wave exciting force and far-field radiated wave amplitudes (shown in Fig. 2.1 as $A_j^{\pm}$) we examine the fluid domain shown in Fig. A.1 [42]. In

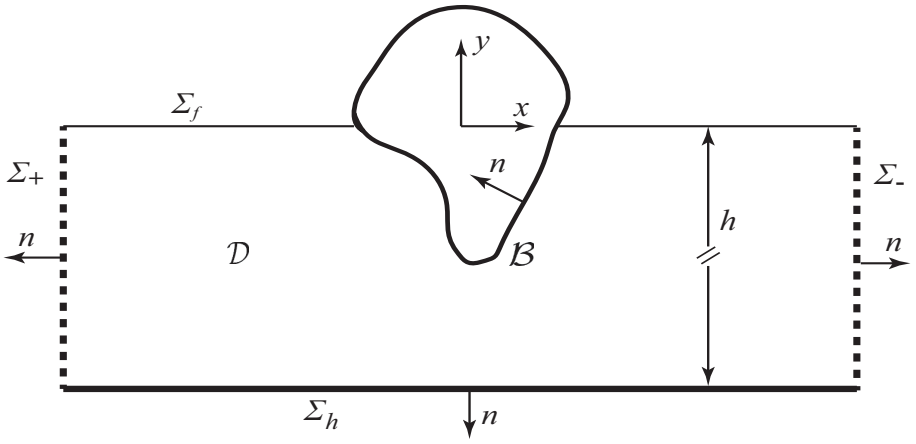

Figure A.1: Fluid domain boundaries and coordinate system.

this figure $\mathcal{B}$, $\mathcal{D}$, n, Σ_f, Σ_h, Σ_-, Σ_+, denote the body boundary, fluid domain, normal vector, free-surface boundary, bottom boundary, far-field left and right boundaries respectively. We begin with considering an incident wave form given in Eqn. (2.14).

$$\eta\left(x,t\right)=\Re\left\{-\frac{1}{g}\frac{\partial\phi_0}{\partial t}\bigg|_{z=h}\right\}=\Re\left\{Ae^{i(\sigma t-kx)}\right\}=A\cos\left(\sigma t-kx\right) \tag{A.1}$$

The total velocity potential that describes the fluid can be decomposed to time harmonic and spatial components as follows.

$$\Phi(x,y,t)=\Re[\phi(x,y)e^{i\sigma t}] \tag{A.2}$$

By the assumptions of small body motion and linearized water-wave theory, the velocity potential can be decomposed to incident, diffraction, and j-th mode radiation potentials; Φ_0, Φ_7, and Φ_j respectively. With $\alpha_j(t)=a_je^{i\sigma t}$ denoting the displacement of the body, the total potential can be written as the following.

$$\Phi(x,y,t)=A[\phi_0(x,y)+\phi_7(x,y)]e^{i\sigma t}+\sum_{j=1}^{3}\phi_j(x,y)[i\sigma a_je^{i\sigma t}] \tag{A.3}$$

The incident wave potential can be obtained by using the linearized dynamics free-surface boundary condition.

$$\left.\frac{\partial \Phi_0}{\partial t}\right|_{y=0} = -g\eta \tag{A.4}$$

Thus, by substituting the incident wave (Eqn. (2.14)) in Eqn. (A.4), incident wave potential can be found

$$\Phi_0 = \Re\{\frac{igA}{\sigma} f(y) e^{i(\sigma t - kx)}\} \tag{A.5}$$

where $f(y)$ describes the variation of the potential along the depth and is given by the following.

$$f(y) = \frac{\cosh k(y+h)}{\cosh kh} \tag{A.6}$$

Now the incident wave velocity potential can be written as

$$\Phi_0 = \Re\{\frac{igA}{\sigma} \frac{\cosh k(y+h)}{\cosh kh} e^{i(\sigma t - kx)}\} \tag{A.7}$$

Then, with the no flux through the body condition

$$\left.\frac{\partial \phi_7}{\partial n}\right|_{\mathcal{B}} = -\left.\frac{\partial \phi_0}{\partial n}\right|_{\mathcal{B}} \tag{A.8}$$

the diffraction potential beyond Σ_- & Σ_+ can be obtained [43],

$$\phi_7 = D^{\pm} f(y) e^{\mp ikx}, \ \substack{x\to+\infty \\ x\to-\infty} \tag{A.9}$$

Equation (A.9) clearly shows that ϕ_7 behaves like two propagating waves, where $D^{\pm}$ are unknown coefficients. In the radiation problem the ϕ_j represents the disturbances caused by the forced oscillation of the body in surge, heave and pitch; ϕ_1, ϕ_2, ϕ_3. Φ_j has to satisfy the linearized dynamics free-surface boundary condition

$$\left.\frac{\partial \Phi_j}{\partial t}\right|_{y=0} = -g\eta \tag{A.10}$$

where $\partial\Phi_j/\partial t = -\sigma^2 a_j \phi_j e^{i\sigma t}$. We obtain boundary conditions on the body surface $\mathcal{B}$ by equating the normal derivative of Eqn. (A.3) to the normal component of the vector on the body surface. These boundary conditions are

$$\frac{\partial \phi_j}{\partial n} = n_j \ , \quad j = 1, 2 \tag{A.11}$$

and

$$\frac{\partial \phi_3}{\partial n} = (\mathbf{r} \times \mathbf{n})_3 \tag{A.12}$$

where **n** and **r** are the unit normal and position vectors. To ensure the uniqueness of the boundary value problem we include the radiation condition that states waves generated from the forced oscillation of the body should radiate away from the body. These result in a well defined solution of the ϕ_j and can be found from the following.

$$\phi_j = -\frac{ig}{\sigma^2} f(y) A_j^{\pm} e^{\mp kx}, \ \substack{x\to+\infty \\ x\to-\infty} \tag{A.13}$$

For a fixed body the wave exciting force can be obtained from the diffraction problem [68].

$$X_j = i\rho\sigma \int_{\mathcal{B}} (\phi_0 + \phi_7) n_j dS \tag{A.14}$$

By applying the boundary condition Eqn. (A.11) to Eqn. (A.14) we have

$$X_j = i\rho\sigma \int_{\mathcal{B}} (\phi_0 + \phi_7) \frac{\partial \phi_j}{\partial n} dS \tag{A.15}$$

For any scalar function pair, ϕ and ψ, Green's Second Identity states

$$\iint_{\partial\nu} (\phi \frac{\partial \psi}{\partial n} - \psi \frac{\partial \phi}{\partial n}) dS = \iiint_{\nu} (\phi \nabla^2 \psi - \psi \nabla^2 \phi) dv = 0 \tag{A.16}$$

Let $\phi \to \phi_j$ and $\psi \to \phi_7$, be the radiation and diffraction potentials. The radiation and diffraction potentials as discussed must satisfy the radiated outgoing waves condition and vanish for the case of infinite depth fluid. Also, the linearized free surface boundary condition must be satisfied by all the potentials then, Eqn. (A.17) follows from the Green's theorem.

$$\iint_{\mathcal{B}} (\phi_j \frac{\partial \phi_7}{\partial n} - \phi_7 \frac{\partial \phi_j}{\partial n}) dS = 0 \tag{A.17}$$

At this point by applying Eqns. (A.17) and (A.8) to Eqn. (A.15) we obtain the following expression for the wave exciting force.

$$X_j = i\rho\sigma \iint_{\mathcal{B}} (\phi_0 \frac{\partial \phi_j}{\partial n} - \phi_j \frac{\partial \phi_0}{\partial n}) dS \tag{A.18}$$

It was shown that wave exciting force only depends on the radiation potential and is independent of diffraction potential. Since, ϕ_0 and ϕ_j both satisfy the free surface boundary condition it follows from Green's theorem that

$$\iint_{\mathcal{B}\cup\Sigma_f\cup\Sigma_h\cup\Sigma_-\cup\Sigma_+} (\phi_0 \frac{\partial \phi_j}{\partial n} - \phi_j \frac{\partial \phi_0}{\partial n}) dS = 0 \tag{A.19}$$

Then, wave exciting force can be evaluated from the infinite surface integral.

$$X_j = i\rho\sigma \iint_{\Sigma_f\cup\Sigma_h\cup\Sigma_-\cup\Sigma_+} (\phi_0 \frac{\partial \phi_j}{\partial n} - \phi_j \frac{\partial \phi_0}{\partial n}) dS \tag{A.20}$$

Finally, for the two dimensional case shown in Fig. A.1, the surface integral Eqn. (A.20) can be written as a line integral. Also, the $\frac{\partial}{\partial n} = -\frac{\partial}{\partial x}$ for $x >> 0$ (Σ_+) and $\frac{\partial}{\partial n} = \frac{\partial}{\partial x}$ for $x << 0$ (Σ_-).

$$X_j = i\rho\sigma \int_{-h}^{0} (\phi_0 \frac{\partial \phi_j}{\partial x} - \phi_j \frac{\partial \phi_0}{\partial x}) \Big|_{x=-\infty}^{x=+\infty} dy \tag{A.21}$$

At this point, with substituting Eqns. (A.7) and (A.13) in Eqn. (A.21) we obtain

$$\begin{aligned} \frac{X_j}{i\rho\sigma} = \frac{2ikg^2A}{\sigma^3} \Bigg\{ & \int_{-h}^{0} \frac{\cosh^2 k(y+h)}{\cosh^2 kh} A_j^+ e^{-2ikx} \Big|_{x=+\infty} dy \\ & + \int_{-h}^{0} \frac{\cosh^2 k(y+h)}{\cosh^2 kh} A_j^- e^{-ikx} e^{ikx} \Big|_{x=-\infty} dy \Bigg\} \end{aligned} \tag{A.22}$$

which simplifies to

$$\frac{X_j}{i\rho\sigma} = \frac{2ikg^2A}{\sigma^3} \int_{-h}^{0} \frac{\cosh^2 k(y+h)}{\cosh^2 kh} A_j^- dy \tag{A.23}$$

With denoting $q(\sigma, h) = 2k \int_{-h}^{0} \frac{\cosh^2 k(y+h)}{\cosh^2 kh} dy$ that equates to 1 as $h \to \infty$, the expression of the wave exciting force becomes more simplified.

$$\frac{X_j}{A} = -\frac{\rho g^2}{\sigma^2} A_j^- \tag{A.24}$$

This relation is known as the Haskind relation for this problem, which relates the wave exciting force to the left far-field wave amplitude. Thus, with the forced oscillation of the body in calm water we can obtain the wave exciting force on the body in the presence of incident waves. For a different incident wave such as $\eta(x,t) = A\sin(kx - \sigma t)$ one can follow the same analysis which lead to the following expression for the wave exciting force.

$$\frac{X_j}{A} = -\frac{i\rho g^2}{\sigma^2} A_j^- \tag{A.25}$$

Appendix B

Wave Exciting Force and Radiation Damping

As shown in Eqn. (A.24) the wave exciting force (X_j) is related to the left far-field radiated wave amplitude (A_j^-, shown in Fig. 2.1) which indicates wave exciting force can also be related to the radiation damping of the body. With looking at the second mode of motion (heave), the radiation force has the following form

$$F_2(t) = -\mu_{22}\ddot{\alpha}_2(t) - \lambda_{22}\dot{\alpha}_2(t) \tag{B.1}$$

where μ_{22} is the heave added mass, λ_{22} is the radiation damping, and $\alpha_2(t) = a_2 e^{i\sigma t}$ is the heave displacement of the body. Then, the time average work done on the fluid by the body can be found by

$$\overline{\dot{W}} = \frac{1}{T}\int_0^T -F_2(t)\dot{\alpha}_2(t)\ dt \tag{B.2}$$

where because of the orthogonality of the μ_{22} and $\dot{\alpha}_2(t)$, only λ_{22} contributes to the work.

$$\overline{\dot{W}} = \lambda_{22} \mid a_2 \mid^2 \sigma^2 \frac{1}{T}\int_0^T \sin^2 \sigma t\ dt = \frac{\lambda_{22} \mid a_2 \mid^2 \sigma^2}{2} \tag{B.3}$$

Energy flux of the linear harmonic wave per unit wave front is $\overline{\dot{E}} = 1/2\rho g A^2 V_g$ where $V_g = g/2\sigma$. Then, the energy flux associated with the propagating far-filed wave amplitudes ($A_j^{\pm}$) can be found next.

$$\overline{\dot{E}} = \frac{1}{2}\rho g A_j^+ \bar{A}_j^+ \mid a_2 \mid^2 \frac{g}{2\sigma} + \frac{1}{2}\rho g A_j^- \bar{A}_j^- \mid a_2 \mid^2 \frac{g}{2\sigma} = \frac{1}{2}\rho g \mid a_2 \mid^2 \left(\mid A_j^+ \mid^2 + \mid A_j^- \mid^2\right) \tag{B.4}$$

At this point by equating Eqns. (B.3) and (B.4) the relation between the radiation damping and far-filed wave amplitudes can be realized.

$$\lambda_{22} = \frac{\rho g^2}{2\sigma^3}\left(\mid A_j^+ \mid^2 + \mid A_j^- \mid^2\right) \tag{B.5}$$

By denoting $\gamma = \mid A_j^+/A_j^- \mid$ the geometry-hydrodynamic factor and substituting this factor in Eqn. (B.5) and using the Haskind relation Eqn. (A.24), the relation between the wave exciting force and radiation damping can be stablished.

$$\mid X_2 \mid^2 = \frac{2\rho g^2}{\sigma}\frac{\lambda_{22}}{(1+\gamma^2)} \tag{B.6}$$

Appendix C

Peak-to-Average Power and Matrix Expressions

When the motion of the floater is limited to a maximum allowable displacement ($\xi_2|_{max}$), the PTO force can be applied to ensure the displacement does not exceed this limit. The damping of the PTO can be obtained from Eqn. (2.19) by setting $\xi_2 = \xi_2|_{max}$ and solving for the damping (B_g) as

$$B_g|_{pc} = \left\{ \left(\frac{A|X_2|}{\sigma|\xi_2|_{max}} \right)^2 - \left[\frac{C_{22} + C_g}{\sigma} - \sigma \left(m + \mu_{22} + \mu_g \right) \right]^2 \right\}^{1/2} - \lambda_{22} \tag{C.1}$$

Next, the instantaneous power passing through an ideal power-take-off unit can be calculated from

$$P\left(t\right) = \frac{1}{2}\left[B_g|i\sigma\xi_2|^2 + |i\sigma\xi_2|^2|B_g - iC_g/\sigma| \cos\left(2\left(\omega t + \varphi\right) + \nu\right) \right] \tag{C.2}$$

where φ is the argument of $i\sigma\xi_2$, ν is the argument of $B_g - iC_g/\sigma$ [47]. Then, from TAP absorbed by the PTO (recall Eqn. (2.20)) and Eqn. (C.2) the $P_\pm$ is peak-to-average power ratio can be obtained as follows

$$P_\pm = 1 \pm \sqrt{1 + \left[\frac{C_{22} - \sigma^2\left(m + \mu_{22}\right)}{\sigma B_g} \right]^2} \tag{C.3}$$

The time-derivative matrix, $\Gamma \in \mathbb{R}^{N\times N}$, is block diagonal with the following block structure

$$\Gamma^j = \begin{bmatrix} 0 & j\sigma_0 \\ -j\sigma_0 & 0 \end{bmatrix} \quad \text{for} \quad j = 1, 2, \ldots, N/2 \tag{C.4}$$

Using a change of variables, the surge-pitch radiation convolution integral can be represented in matrix form as follows

$$f_{r12}\left(t\right) = \int_{-\infty}^{t} K_{r12}\left(t-\tau\right)\dot{\zeta}_2\left(\tau\right)d\tau = \Phi\left(t\right)\left(G_{12} - \mu_{12}\left(\infty\right)\Gamma\right)\hat{\psi} \tag{C.5}$$

where $G_{12} \in \mathbb{R}^{N\times N}$ is block diagonal with the following structure

$$G_{12}^j = \begin{bmatrix} \lambda_{12}\left(j\sigma_0\right) & \sigma\mu_{12}\left(j\sigma_0\right) \\ -j\sigma_0\mu_{12}\left(j\sigma_0\right) & \lambda_{12}\left(j\sigma_0\right) \end{bmatrix} \text{ for } j = 1, 2, \ldots, N/2 \tag{C.6}$$

Appendix D

Displacement of Wavemaker

The Fourier coefficients for obtaining the time histories of the wavemaker displacements to obtain deep-water plunging breakers are included in the following tables. The Tables D.1 and D.2 data can be used for the piston-type wavemaker.

Table D.1: Fourier Series input for wavemaker displacement profile resulting in a plunging breaker at 11 m.

n	ω_n	x_n	θ_n	n	ω_n	x_n	θ_n	n	ω_n	x_n	θ_n
1	0.000	-6.114e-04	-1.571	2	0.313	2.381e-04	-0.257	3	0.625	7.149e-04	-2.315
4	0.938	8.266e-04	-3.223	5	1.250	7.611e-04	-4.175	6	1.563	8.418e-04	0.987
7	1.876	1.193e-03	-0.171	8	2.188	1.846e-03	-1.003	9	2.501	3.319e-03	-1.595
10	2.813	1.401e-02	-4.139	11	3.126	1.545e-02	-0.414	12	3.439	1.674e-02	-2.978
13	3.751	1.422e-02	0.334	14	4.064	1.495e-02	-2.999	15	4.376	1.379e-02	-0.337
16	4.689	1.345e-02	-4.214	17	5.002	1.390e-02	-2.215	18	5.314	1.221e-02	-0.596
19	5.627	5.859e-03	1.341	20	5.939	1.230e-03	0.953	21	6.252	4.294e-04	0.941
22	6.565	1.990e-04	-4.555	23	6.877	2.523e-04	-4.263	24	7.190	3.263e-04	-4.587
25	7.502	2.692e-04	1.382	26	7.815	1.678e-04	0.910	27	8.128	6.221e-05	0.567
28	8.440	7.889e-05	-3.757	29	8.753	1.368e-04	-4.288	30	9.065	1.251e-04	1.464
31	9.378	3.906e-05	-4.666	32	9.690	1.099e-04	1.046	33	10.003	3.401e-05	-1.937
34	10.316	9.712e-05	-4.264	35	10.628	1.893e-05	1.033	36	10.941	1.432e-04	-4.598
37	11.253	4.304e-05	-1.345	38	11.566	6.128e-05	1.512	39	11.879	5.026e-05	-3.090
40	12.191	3.610e-05	1.014	41	12.504	6.492e-05	-3.795	42	12.816	5.279e-05	0.446
43	13.129	4.528e-05	-3.556	44	13.442	3.627e-05	-1.072	45	13.754	7.736e-05	-4.596
46	14.067	4.639e-05	-2.989	47	14.379	5.289e-05	0.115	48	14.692	6.801e-05	-4.156
49	15.005	4.894e-05	-2.199	50	15.317	3.754e-05	0.222	51	15.630	4.738e-05	-4.290

Table D.2: Fourier Series input for wavemaker displacement profile resulting in a plunging breaker at 21 m.

n	ω_n	x_n	θ_n	n	ω_n	x_n	θ_n	n	ω_n	x_n	θ_n
1	0.000	-1.426e-03	-1.571	2	0.260	4.875e-04	0.534	3	0.519	1.093e-03	0.295
4	0.779	5.426e-04	0.633	5	1.039	5.514e-04	0.469	6	1.299	9.290e-04	0.393
7	1.558	6.756e-04	0.807	8	1.818	1.046e-03	0.173	9	2.078	1.522e-03	0.278
10	2.338	1.765e-03	-0.461	11	2.597	4.908e-03	0.024	12	2.857	1.320e-02	-1.848
13	3.117	1.402e-02	-3.738	14	3.377	1.555e-02	0.636	15	3.636	1.390e-02	-1.829
16	3.896	1.153e-02	-4.579	17	4.156	1.107e-02	-1.531	18	4.415	1.038e-02	1.293
19	4.675	1.149e-02	-2.576	20	4.935	1.168e-02	-0.681	21	5.195	9.179e-03	0.880
22	5.454	6.535e-03	-3.910	23	5.714	2.371e-03	-1.657	24	5.974	1.234e-03	-3.597
25	6.234	1.340e-03	-3.954	26	6.493	1.883e-03	-0.849	27	6.753	1.500e-03	-2.778
28	7.013	1.178e-03	0.862	29	7.272	1.177e-03	-1.547	30	7.532	7.510e-04	-4.065
31	7.792	1.226e-03	-0.546	32	8.052	1.016e-03	-3.793	33	8.311	1.116e-03	-1.147
34	8.571	9.840e-04	-4.604	35	8.831	1.050e-03	-1.598	36	9.091	6.874e-04	1.038
37	9.350	7.645e-04	-3.487	38	9.610	1.027e-03	-1.132	39	9.870	1.320e-03	1.029
40	10.130	1.183e-03	-3.534	41	10.389	1.064e-03	-1.680	42	10.649	5.545e-04	0.494
43	10.909	2.152e-04	-3.936	44	11.168	2.094e-04	-2.166	45	11.428	2.518e-04	0.251
46	11.688	1.099e-04	-2.393	47	11.948	1.023e-04	1.154	48	12.207	2.186e-04	-2.579
49	12.467	2.717e-04	0.440	50	12.727	2.833e-04	-3.275	51	12.987	1.011e-04	-0.803
52	13.246	1.199e-04	-1.467	53	13.506	5.270e-05	-4.315	54	13.766	8.823e-05	-4.561
55	14.025	7.097e-05	-3.021	56	14.285	1.339e-04	0.313	57	14.545	4.467e-05	-4.341
58	14.805	2.181e-04	-2.729	59	15.064	2.174e-04	-0.484	60	15.324	9.449e-05	-4.403
61	15.584	7.303e-05	-4.054	62	15.844	7.245e-05	-0.443	63	16.103	1.367e-05	1.047
64	16.363	6.298e-05	-2.515	65	16.623	9.789e-05	1.189	66	16.883	3.880e-05	-2.696
67	17.142	2.837e-05	-4.590	68	17.402	6.316e-05	-1.029	69	17.662	1.058e-04	-4.628
70	17.921	9.009e-05	-2.233	71	18.181	3.635e-05	-0.757	72	18.441	2.791e-05	-4.607